



### 저작자표시-비영리 2.0 대한민국

이용자는 아래의 조건을 따르는 경우에 한하여 자유롭게

- 이 저작물을 복제, 배포, 전송, 전시, 공연 및 방송할 수 있습니다.
- 이차적 저작물을 작성할 수 있습니다.

다음과 같은 조건을 따라야 합니다:



저작자표시. 귀하는 원저작자를 표시하여야 합니다.



비영리. 귀하는 이 저작물을 영리 목적으로 이용할 수 없습니다.

- 귀하는, 이 저작물의 재이용이나 배포의 경우, 이 저작물에 적용된 이용허락조건을 명확하게 나타내어야 합니다.
- 저작권자로부터 별도의 허가를 받으면 이러한 조건들은 적용되지 않습니다.

저작권법에 따른 이용자의 권리는 위의 내용에 의하여 영향을 받지 않습니다.

이것은 [이용허락규약\(Legal Code\)](#)을 이해하기 쉽게 요약한 것입니다.

[Disclaimer](#)

공학박사 학위논문

**Improving Catalytic Activities by Controlling Metal-Support Interaction between Platinum Group Metals and Transition Metal Oxide Supports**

전이 금속 산화물 지지체와 귀금속 간의 금속-지지체 상호작용을 활용한 촉매 활성 증진

2020년 2월

서울대학교 대학원

화학생물공학부

이 재 하

# **Abstract**

## **Improving Catalytic Activities by Controlling Metal-Support Interaction between Platinum Group Metals and Transition Metal Oxide Supports**

Jaeha Lee

School of Chemical and Biological Engineering

The Graduate School

Seoul National University

By manipulating metal-support interaction between PGMs and metal-oxide supports, the catalysts' chemical properties could be modulated and their catalytic performances could be significantly improved. In addition, it is most desirable both in academic and industrial perspectives to control the metal-support interaction in a simple but effective manner. In this context, in this thesis, the metal-support interaction was studied under both oxidizing and reducing environments. Based on the understanding of the interaction under

various environments, three different simple but effective strategies were devised to improve catalytic performances.

The interaction between Pt and CeO<sub>2</sub> under reducing and oxidizing conditions were extensively investigated. According to Raman spectroscopy, Pt species are strongly bonded on CeO<sub>2</sub> surface by forming Pt-O-Ce bond under the oxidizing condition. Interestingly, Pt-O-Ce bonds became more resistive to the reducing treatment when the oxidation temperature increased from 500 °C to 800 °C. Under the reducing condition, the amount of CO chemisorbed on CeO<sub>2</sub> is almost equal to that on Pt/CeO<sub>2</sub>, implying that Pt atoms are located on the oxygen vacancy generated on reduced CeO<sub>2</sub> surface. The textural properties of Pt/CeO<sub>2</sub> were maintained from the oxidative treatment at high temperature as high as 1000 °C. However, the thermal stability of Pt/CeO<sub>2</sub> greatly decreased when Pt-O-Ce bonds are selectively removed. Therefore, it can be concluded that Pt-O-Ce bonds play the critical role in improving the thermal stability of Pt/CeO<sub>2</sub>.

The CO oxidation ability of Pt/CeO<sub>2</sub> catalysts can be greatly improved by weakening the metal-support interaction between Pt and CeO<sub>2</sub> by decreasing the defect concentration of CeO<sub>2</sub> surface before loading Pt. The defect concentration of CeO<sub>2</sub> surface could be readily decreased by the thermal treatment of CeO<sub>2</sub> at high-temperature. In short, Pt/(800C)CeO<sub>2</sub> was prepared by the thermal treatment of CeO<sub>2</sub> at 800 °C before loading Pt. Pt/(800C)CeO<sub>2</sub> maintained the much higher Pt dispersion than Pt/ $\gamma$ -Al<sub>2</sub>O<sub>3</sub> after the thermal aging at 800 °C, indicating its excellent thermal resistance against Pt sintering.

In addition, the CO oxidation rate of Pt/(800C)CeO<sub>2</sub> was order-of-magnitude higher than that of Pt/CeO<sub>2</sub>. The temperature for 50 % conversion of CO oxidation of Pt/(800C)CeO<sub>2</sub> was 76 °C lower than that of Pt/CeO<sub>2</sub>. Particularly, Pt/(800C)CeO<sub>2</sub> accomplished ~100% CO conversion below 150 °C. Such enhanced activity is explained by the formation of PtO<sub>2</sub> species that interact weakly with CeO<sub>2</sub>.

Similarly to Pt/CeO<sub>2</sub> catalysts, the CO oxidation ability of Pt/TiO<sub>2</sub> catalysts could be improved by weakening the metal-support interaction between Pt and TiO<sub>2</sub> by using S-doped TiO<sub>2</sub> (S-TiO<sub>2</sub>) as the support. The temperature for 50 % conversion of CO oxidation of Pt/S-TiO<sub>2</sub> was 50 °C lower than that of Pt/TiO<sub>2</sub>. Especially, Pt(4)/S-TiO<sub>2</sub> accomplished ~100% CO conversion below 150 °C. Such improvement in activity is explained by the formation of large Pt clusters on S-TiO<sub>2</sub> with more metallic character.

The catalytic performance could be also improved by modifying the geometry of catalysts to facilitate the metal-support interaction. The type of catalysts with Pt nanoparticles (NP) encapsulated in CeO<sub>2</sub> over-layers ('Pt in CeO<sub>2</sub>') were successfully prepared by applying the controlled reductive treatments. Pt NP are covered by CeO<sub>2</sub> over-layers as revealed by HAADF-STEM images and CO chemisorption. While 'Pt on CeO<sub>2</sub>' exhibits good high temperature Water-Gas-Shift reaction (HT-WGSR) activity, Pt sites also catalyze the formation of CH<sub>4</sub> as by-product, which places the limitation on the use of Pt/CeO<sub>2</sub> as HT-WGSR catalyst. On the contrary, the CH<sub>4</sub> production was successfully inhibited on 'Pt in CeO<sub>2</sub>' while high WGS activity was maintained.

Interestingly, thin CeO<sub>2</sub> over-layers could catalyze WGSR while thick CeO<sub>2</sub> over-layers could not. This is attributed to the high concentration of oxygen vacancies on thin CeO<sub>2</sub> over-layers that aided the formation of catalytically active monodentate formate intermediates. Detailed CO chemisorption, XPS and in-situ DRIFT studies unraveled the catalytic properties of CeO<sub>2</sub> over-layers formed by controlled reductive treatments.

**Keywords:** platinum group metals, transition metal oxide supports, metal-support interaction, CO oxidation, Water-Gas-Shift reaction

**Student Number:** 2014-21513

# Contents

|                              |           |
|------------------------------|-----------|
| <b>Abstract .....</b>        | <b>i</b>  |
| <b>List of Tables .....</b>  | <b>ix</b> |
| <b>List of Figures .....</b> | <b>xi</b> |

## **Chapter 1. Introduction..... 1**

|   |   |
|---|---|
| 1.1. Necessities to study the control of metal-supporting interactions in heterogeneous catalysts ..... | 1 |
| 1.2. CO oxidation.....  | 3 |
| 1.3. Water-Gas-Shift reaction.....  | 4 |
| 1.4. Objectives .....   | 5 |

## **Chapter 2. How Pt interacts with CeO<sub>2</sub> under the reducing and oxidizing environments at elevated temperature? The origin of improved thermal stability of Pt/CeO<sub>2</sub> compared to CeO<sub>2</sub>..... 7**

|                        |    |
|------------------------|----|
| 2.1. Introduction..... | 7  |
| 2.2. Experimental..... | 10 |
| 2.3. Results.....      | 14 |

|   |    |
|---|----|
| 2.3.1. Position of Pt on CeO <sub>2</sub> under oxidizing and reducing condition..... | 14 |
| 2.3.2. The role of Pt-O-Ce bond in the thermal stability of CeO <sub>2</sub> .....    | 24 |
| 2.3.3. Pt-CeO <sub>2</sub> interaction under the oxidizing environment ..             | 32 |
| 2.4. Discussion.....  | 36 |

## **Chapter 3. Weakening the metal-support interaction to improve catalytic activities of PGM supported catalysts (Pt/CeO<sub>2</sub>&Pt/TiO<sub>2</sub>) ..... 40**

|  |    |
|--|----|
| 3.1. Introduction.....   | 40 |
| 3.2. Experimental.....   | 44 |
| 3.3. Results.....  | 52 |
| 3.3.1. The CO oxidation ability of Pt(2)/CeO <sub>2</sub> and CeO <sub>2</sub> .....   | 52 |
| 3.3.2. The influence of the change in Pt-CeO <sub>2</sub> interaction induced by the thermal treatment of CeO <sub>2</sub> prior to the Pt loading ..... | 54 |
| 3.2.2.1. The influence on the Pt sintering behavior .....  | 54 |
| 3.3.2.2. The influence on the CO oxidation ability .....   | 56 |
| 3.2.2.3. The relationships between the Pt dispersion and the CO oxidation ability .....  | 59 |
| 3.3.3 Chemical states of the Pt species on CeO <sub>2</sub> , (800C)CeO <sub>2</sub>   |    |

|  |    |
|--|----|
| and $\gamma$ -Al <sub>2</sub> O <sub>3</sub> supports .....  | 67 |
| 3.3.3.1 Investigation of the chemical states of Pt species by<br>CO chemisorption.....   | 67 |
| 3.3.3.2. Investigation of the chemical states of Pt species by<br>XP spectroscopy .....  | 71 |
| 3.3.3.3. Investigation of the chemical states of Pt species by<br>H <sub>2</sub> -TPR .....  | 75 |
| 3.3.4. S dopants on TiO <sub>2</sub> surface weakens the Pt-TiO <sub>2</sub> interaction<br>and improves the CO oxidation ability of Pt/TiO <sub>2</sub> catalysts ... | 78 |

## **Chapter 4. Synthesis of Pt nanoparticles encapsulated in CeO<sub>2</sub> over-layers by controlled reduction treatment to suppress CH<sub>4</sub> formation in high-temperature Water-Gas-Shift reaction ..... 84**

|   |     |
|---|-----|
| 4.1. Introduction.....  | 84  |
| 4.2. Experimental.....  | 87  |
| 4.3. Results.....   | 92  |
| 4.3.1. Synthesis of ‘Pt in CeO <sub>2</sub> ’ with the controlled reductive<br>treatment.....   | 92  |
| 4.3.2. Comparison of WGS activity and CH <sub>4</sub> yield of ‘Pt on<br>CeO <sub>2</sub> ’ and ‘Pt in CeO <sub>2</sub> ’ catalysts ..... | 100 |
| 4.3.2.1. WGS activity.....  | 100 |

|   |     |
|---|-----|
| 4.3.2.2. CH <sub>4</sub> yield .....  | 102 |
| 4.3.2.3. R and NC treatments at other temperatures.....   | 104 |
| 4.3.3. Why only Pt(2)/CeO <sub>2</sub> 800NC has the WGS activity, not<br>Pt(2)/CeO <sub>2</sub> 800R?..... | 112 |

**Chapter 5. Summary and Conclusions ..... 122**

**Bibliography ..... 125**

**국 문 초 록..... 133**

## List of Tables

|  |    |
|--|----|
| <b>Table 2-1.</b> The amount of chemisorbed CO on CeO <sub>2</sub> and Pt(2)/CeO <sub>2</sub> , after in-situ reduction treatment at different temperature .....   | 19 |
| <b>Table 2-2.</b> Physiochemical properties of CeO <sub>2</sub> , Pt(2)/CeO <sub>2</sub> and Pt(2)/Al <sub>2</sub> O <sub>3</sub> samples, oxidized at various temperatures. In-situ reduction for CO chemisorption was proceeded at 350 °C for Pt/CeO <sub>2</sub> (and Pt/Al <sub>2</sub> O <sub>3</sub> ) and 500 °C for CeO <sub>2</sub> samples ..... | 28 |
| <b>Table 2-3.</b> Physiochemical properties of Pt/CeO <sub>2</sub> samples, with various Pt loading and after different kinds of thermal treatments .....  | 29 |
| <b>Table 2-4.</b> Relative surface concentration (wt%) of Pt, Ce, and O of Pt(2)/CeO <sub>2</sub> samples from XPS.....  | 34 |
| <b>Table 3-1.</b> Activation energy, TOF (at 190 °C), T <sub>50</sub> and T <sub>90</sub> of CO oxidation over CeO <sub>2</sub> , Pt(2)/CeO <sub>2</sub> , Pt(2)/(800C)CeO <sub>2</sub> and Pt(2)/γ-Al <sub>2</sub> O <sub>3</sub> catalysts after oxidative treatment at 500 and 800 °C.....  | 61 |
| <b>Table 3-2.</b> The amount of chemisorbed CO, the Pt dispersion, and the ratio between the amount of Pt loaded and the amount of chemisorbed CO of CeO <sub>2</sub> , Pt(2)/CeO <sub>2</sub> , Pt(2)/(800C)CeO <sub>2</sub> and Pt(2)/γ-Al <sub>2</sub> O <sub>3</sub> after the oxidative treatment at 500 and 800 °C .....                             | 62 |
| <b>Table 3-3.</b> The relative atomic concentration of Pt to Ce and Pt <sup>2+</sup> to Pt <sup>4+</sup> of Pt(2)/CeO <sub>2</sub> and Pt(2)/(800C)CeO <sub>2</sub> catalysts obtained from X-ray Photoelectron Spectroscopy.....  | 73 |

|  |     |
|--|-----|
| <b>Table 4-1.</b> Physiochemical properties of Pt(2)/CeO <sub>2</sub> catalysts, after various thermal treatments .....  | 95  |
| <b>Table 4-2.</b> Average Pt NP size and Pt dispersion, measured from pulsed CO chemisorption at -78 °C and particle size distribution curves obtained from HAADF-STEM images .....  | 96  |
| <b>Table 4-3.</b> WGS reaction activity and CH <sub>4</sub> selectivity of Pt(2)/CeO <sub>2</sub> 500C, Pt(2)/CeO <sub>2</sub> 800R and Pt(2)/CeO <sub>2</sub> 800 NC at 400 and 450 °C. Reactant was composed of 3 % CO, 24 % H <sub>2</sub> O, (3 % CO <sub>2</sub> ), (20 % H <sub>2</sub> ), and He balance gas with the total flow rate of 70 mL/min .. | 105 |

## List of Figures

- Figure 2-1.** Sample preparation procedure and the notation of samples thereof .....13
- Figure 2-2.** H<sub>2</sub> Temperature Programmed Reduction curves of CeO<sub>2</sub> 500C and Pt(2)/CeO<sub>2</sub> 500C samples .....20
- Figure 2-3.** (a) Ex-situ Raman spectra of CeO<sub>2</sub> 500C, Pt(0.05)/CeO<sub>2</sub> 500C and Pt(2)/CeO<sub>2</sub> 500C samples (from bottom to top). (b) Magnified region of 300 cm<sup>-1</sup>~1400 cm<sup>-1</sup> .....21
- Figure 2-4.** In-situ Raman spectra of Pt(2)/CeO<sub>2</sub> (a) 500C and (b) 800C obtained at temperature from 50 °C to 250 °C with a temperature step of 25 °C, under the reducing condition. 20 min was maintained at each temperature and spectra were obtained after cooling down to 50 °C .....22
- Figure 2-5.** (a) After the oxidative treatment, Pt-O-Ce bond is formed between Pt and CeO<sub>2</sub>. CeO<sub>2</sub> surface is also oxidized. (b) After the reductive treatment, CeO<sub>2</sub> surface is reduced and oxygen vacancies are generated on the surface. Pt is located in the oxygen vacancies....23
- Figure 2-6.** XRD patterns of (a) CeO<sub>2</sub> and (b) Pt(2)/CeO<sub>2</sub> samples, taken after oxidative treatment at 500, 600, 700 and 800 °C for 2 h.....30
- Figure 2-7.** BJH pore size distribution curves of CeO<sub>2</sub> and Pt/CeO<sub>2</sub> samples. Desorption branch of N<sub>2</sub> was analyzed. (a) CeO<sub>2</sub> and Pt(2)/CeO<sub>2</sub> treated at 500 °C and 800 °C. (b) The role of surface oxygen and bulk oxygen of Pt(2)/CeO<sub>2</sub> 500C in sustaining the CeO<sub>2</sub> structure

from high temperature treatment, (c) The effect of Pt loadings on the pore size distribution of Pt/CeO<sub>2</sub> under the oxidative condition .....31

**Figure 2-8.** H<sub>2</sub> Temperature Programmed Reduction curves of Pt(2)/CeO<sub>2</sub> samples, after oxidation at 500, 600, 700 and 800 °C for 2 h ....35

**Figure 2-9.** Schematic diagram comparing the behavior of (a) CeO<sub>2</sub> and (b) Pt(2)/CeO<sub>2</sub> after the oxidation treatment at high temperature. After 800 °C oxidation treatment, crystalline size of Pt(2)/CeO<sub>2</sub> was only slightly increased, while that of CeO<sub>2</sub> was greatly increased from 8.6 nm to 17.2 nm. After the 800 °C oxidation treatment, Pt diffused into CeO<sub>2</sub> structure, while maintaining the CeO<sub>2</sub> structure from the oxidative treatment .....39

**Figure 3-1.** , (a) Raman spectra of CeO<sub>2</sub> 500C and CeO<sub>2</sub> 800C. To observe the rise of Raman peak at 595 cm<sup>-1</sup>, Raman spectra of (a) is magnified 15 times on (b) .....51

**Figure 3-2.** Light-off curves of CO oxidation over (a) CeO<sub>2</sub> and (b) Pt(2)/CeO<sub>2</sub> catalysts, after oxidative treatments at 500 and 800 °C .....53

**Figure 3-3.** (a) XRD pattern of Pt(2)/(800C)CeO<sub>2</sub> and Pt(2)/γ-Al<sub>2</sub>O<sub>3</sub> catalysts after the oxidative treatments at 500 and 800 °C. (b) XRD pattern of Pt(2)/(800C)CeO<sub>2</sub> 500C, 800C and Pt(2)/CeO<sub>2</sub> 800C catalysts .....55

**Figure 3-4.** (a) Light-off curves of CO oxidation over Pt(2)/CeO<sub>2</sub> and Pt(2)/γ-Al<sub>2</sub>O<sub>3</sub> catalysts, after oxidative treatments at 500 and 800 °C. (b)

Light-off curves of CO oxidation over Pt(2)/(800C)CeO<sub>2</sub> and Pt(2)/ $\gamma$ -Al<sub>2</sub>O<sub>3</sub> catalysts, after oxidative treatment at 500 and 800 °C. Pt(2)/(800C)CeO<sub>2</sub> 500C was exposed to 1000 ppm of CO for 5 h at room temperature to reach the steady state CO concentration before reaction .....63

**Figure 3-5.** (a) The temperature dependence of TOF of Pt(2)/CeO<sub>2</sub> 500C and 800C catalysts. (b) The temperature dependence of TOF of Pt(2)/(800C)CeO<sub>2</sub> 500C and 800C catalysts. For a comparison, TOFs of Pt(2)/ $\gamma$ -Al<sub>2</sub>O<sub>3</sub> 500C are provided in the figure .....64

**Figure 3-6.** (a) CO break-through curves with time-on-stream during the CO oxidation (1000 ppm CO and 10 % O<sub>2</sub>) at the room temperature over Pt(2)/CeO<sub>2</sub> 500C and Pt(2)/(800C)CeO<sub>2</sub> 500C catalysts. (b) CO break-through curves with time-on-stream during the CO oxidation at the room temperature over Pt(2)/(800C)CeO<sub>2</sub> 500C and 800C catalysts .....65

**Figure 3-7.** (a) Light-off curves of the CO oxidation over Pt(2)/(800C)CeO<sub>2</sub> 800C and Pt(2)/ $\gamma$ -Al<sub>2</sub>O<sub>3</sub> 800C catalysts with 1 % of CO in the feed. (b) The activation energy (E<sub>a</sub>) was calculated from the slope of the Arrhenius-type plot of the TOFs .....66

**Figure 3-8.** CO chemisorption curves of CeO<sub>2</sub> and Pt(2)/CeO<sub>2</sub> catalysts, after the oxidative treatments at 500 and 800 °C. In-situ reduction temperature is marked in the parenthesis. Filled symbol represents the sum of the amount of chemisorbed and physisorbed CO while

the empty symbol represents the amount of physisorbed CO. On the table listed is the amount of chemisorbed CO and the amount of Pt impregnated on CeO<sub>2</sub>. .....69

**Figure 3-9.** CO chemisorption curves of Pt(2)/(800C)CeO<sub>2</sub> 500C, 800C and CeO<sub>2</sub> 800C catalysts. The in-situ reduction temperature is marked in the parenthesis. Filled symbol represents the sum of the amount of chemisorbed and physisorbed CO while the empty symbol represents the amount of physisorbed CO. On the table listed is the amount of chemisorbed CO and the amount of Pt impregnated on (800C)CeO<sub>2</sub>. .....70

**Figure 3-10.** XP spectra of (a) Pt(2)/CeO<sub>2</sub> 500C, (b) Pt(2)/CeO<sub>2</sub> 800C, (c) Pt(2)/(800C)CeO<sub>2</sub> 500C and (d) Pt(2)/(800C)CeO<sub>2</sub> 800C. The contributions from Pt<sup>2+</sup>, Pt<sup>4+</sup>, and Pt<sup>0</sup> species are de-convoluted and marked on the figures .....74

**Figure 3-11.** Cryo H<sub>2</sub>-TPR curves of (a) Pt(2)/CeO<sub>2</sub> and (b) Pt(2)/(800C)CeO<sub>2</sub> catalysts after oxidative treatments at 500 and 800 °C. ....77

**Figure 3-12.** HAADF-STEM images of (a) Pt(4)/TiO<sub>2</sub> 500C and (b) Pt(4)/S-TiO<sub>2</sub> 500C catalysts. (c) Particle size distributions of Pt particles. (d) Fourier Transform of k<sup>3</sup>-weighted EXAFS spectra at the Pt L3-edge of Pt/TiO<sub>2</sub> 500C and Pt/S-TiO<sub>2</sub> 500C catalysts compared to those of reference Pt foil and PtO<sub>2</sub> .....81

**Figure 3-13.** XANES spectra at the Pt L3-edge of Pt/TiO<sub>2</sub> 500C and Pt/S-TiO<sub>2</sub> 500C in comparison with those of reference PtO<sub>2</sub> and Pt foil .....82

**Figure 3-14.** (a) Comparison of the CO conversion curves for Pt/TiO<sub>2</sub> 500C and Pt/S-TiO<sub>2</sub> 500C catalysts. (b) The temperature of 50 % conversion (T<sub>50</sub>) in CO oxidation over various Pt/TiO<sub>2</sub> 500C catalysts as a function of the relative amount of metallic Pt in catalysts. Relative amount of metallic Pt was obtained from the linear combination analysis of XANES spectra of Pt/TiO<sub>2</sub> catalysts, assuming only Pt and PtO<sub>2</sub> species are present on the catalysts. XANES spectra of Pt foil and PtO<sub>2</sub> were taken as references.....83

**Figure 4-1.** BJH pore distribution curve of Pt(2)/CeO<sub>2</sub> XR and XNC catalysts are displayed in (a) and (b), respectively. (c) Apparent Pt dispersion was measured from pulsed CO chemisorption at -78 °C .....97

**Figure 4-2.** HAADF-STEM images of Pt(2)/CeO<sub>2</sub> 800R (a) and 800NC (b); corresponding particle size distribution curves are displayed in (c). (d) The comparison of Pt dispersion measured by HAADF-STEM images and CO chemisorption, which indicate that Pt nanoparticles are covered by CeO<sub>2</sub> over-layers. (e) XRD patterns of Pt/CeO<sub>2</sub> catalysts in the 2θ region between 25 and 35 ° to observe peaks from fluorite structured CeO<sub>2</sub> particles. (f) XRD patterns of Pt/CeO<sub>2</sub> catalysts in the 2θ region between 35 and 45 ° to observe the peak from agglomerated Pt clusters at 39.5 ° .....98

**Figure 4-3.** Schematics displaying the effect of XR and XNC treatments in the structure of Pt/CeO<sub>2</sub> catalysts.....99

**Figure 4-4.** WGS reaction activity of Pt(2)/CeO<sub>2</sub> 500C (a) and Pt(2)/CeO<sub>2</sub>

800NC (b) catalysts under various feed conditions. The CH<sub>4</sub> yield of Pt/CeO<sub>2</sub> 500C and 800NC catalysts are compared in (c) .....106

**Figure 4-5.** (a) Comparison of WGS activity of Pt(2)/CeO<sub>2</sub> 500C ('Pt on CeO<sub>2</sub>') and Pt(2)/CeO<sub>2</sub> 800NC ('Pt in CeO<sub>2</sub>') under 3 % CO, 24 % H<sub>2</sub>O, 3 % CO<sub>2</sub>, 20 % H<sub>2</sub> with He balance gas. (b) The activation energies of WGS reaction of Pt(2)/CeO<sub>2</sub> 500C and 800NC catalysts under the full gas feed are compared .....107

**Figure 4-6.** The effect of the presence of 5 % H<sub>2</sub>O in the CH<sub>4</sub> yield of Pt/CeO<sub>2</sub> 500C and 800NC catalysts. Reactants are composed of 3 % CO, 20 % H<sub>2</sub>, (5% H<sub>2</sub>O) and He balance gas with the total flow rate of 70 mL/min .....108

**Figure 4-7.** (a) WGS reactivity and (b) CH<sub>4</sub> yield of Pt(2)/CeO<sub>2</sub> 500C, 500R, 600R, 700R and 800R under the feed of 3 % CO, 24 % H<sub>2</sub>O and He balance gas .....109

**Figure 4-8.** (a) WGS reactivity and (b) CH<sub>4</sub> yield of Pt(2)/CeO<sub>2</sub> 500C, 600R and 700R under the feed of 3 % CO, 24 % H<sub>2</sub>O, 3 % CO<sub>2</sub>, 20 % H<sub>2</sub> and He balance gas .....110

**Figure 4-9.** (a) WGS reactivity and (b) CH<sub>4</sub> yield of Pt(2)/CeO<sub>2</sub> 500C, 600NC, 700NC and 800NC under the feed of 3 % CO, 24 % H<sub>2</sub>O, 3 % CO<sub>2</sub>, 20 % H<sub>2</sub> and He balance gas.....111

**Figure 4-10.** Pulsed CO chemisorption was performed at -78 and 50 °C. The amount of CO chemisorbed in Pt/CeO<sub>2</sub> catalysts (either 'R' or 'NC' treated) are compared in (a). (b) O 1s XPS spectra of Pt(2)/CeO<sub>2</sub>

|  |     |
|--|-----|
| 500C, 800R and 800NC catalysts .....   | 117 |
| <b>Figure 4-11.</b> Bright-field TEM images of Pt(2)/CeO <sub>2</sub> 800R ((a) and (b)) and Pt(2)/CeO <sub>2</sub> 800NC ((c) and (d)) catalysts.....   | 118 |
| <b>Figure 4-12.</b> Pt to Ce molar ratio of Pd(2)/CeO <sub>2</sub> 500C, 800R and 800NC catalysts, calculated from XP spectra, are compared in (a). Error bars are included in the figure. Depth-profiling XP spectra of Pt/CeO <sub>2</sub> catalysts are compared in (b).....  | 119 |
| <b>Figure 4-13.</b> Comparison of in-situ CO-DRIFT spectra of CeO <sub>2</sub> 500C, Pt(2)/CeO <sub>2</sub> 500C, 800NC and 800R after CO adsorption followed by N <sub>2</sub> purging for 60 min at 100 °C .....   | 120 |
| <b>Figure 4-14.</b> The variation in the peak intensity of DRIFT spectra from monodentate formate ( $\nu_s(\text{OCO}) = 1300 \text{ cm}^{-1}$ ) upon H <sub>2</sub> O addition was monitored. Prior to H <sub>2</sub> O addition, catalysts were exposed to CO flow for 60 min and purged under N <sub>2</sub> flow for 60 min. These in-situ DRIFT experiments were carried out at 100 °C..... | 121 |

# **Chapter 1. Introduction**

## **1.1. Necessities to study the control of metal-supporting interactions in heterogeneous catalysts**

Platinum group metals (PGMs) are widely used as catalytically active phase in catalysis. PGMs should be well dispersed on supports (mostly metal oxides) to increase the cost effectiveness (catalytic activity/amounts) because of their high price. In this regards, single-atom catalysts with atomically dispersed PGMs on metal oxides are getting the great research attention lately [1-5]. However, in many occasions, simply achieving the atomic dispersion of PGMs is not enough to accomplish the desired catalytic performances. Several recent articles discussed that the intrinsic catalytic activity of atomically dispersed PGMs is far less than that of PGM ensembles and emphasized that inducing the formation of PGM nanoclusters would be the good strategy to achieve optimum catalytic activity [2, 6-8]. For example, recently, Yang et al. compared the catalytic activities of Pt single-atom and Pt-O-Pt ensemble, both supported on CeO<sub>2</sub>, where the latter displayed the order-of-magnitude higher activity in CO oxidation [2]. In addition, Karim et al. compared the catalytic activities of Pt single-atom, Pt sub-nanometer clusters and Pt nanoparticles, all supported on TiO<sub>2</sub>, and found that Pt nanoparticle displayed the highest intrinsic activity in semi-hydrogenation of acetylene [6]. The question arises why just achieving the high dispersion of PGMs on metal oxides, maximizing the accessible active sites, frequently does not result in the highest catalytic performances.

The famous phrase by Aristotle, “The whole is greater than the sum of its parts” also applies to the field of catalysts. When PGMs and metal oxides are brought in contact, the unique metal-support interaction could grant the extraordinary catalytic activities to PGM supported catalysts. Even when each of PGMs and metal oxides has no catalytic activity, the use of the two together can achieve the high catalytic activity. For example, although Pt and CeO<sub>2</sub> each have little activity in Water-Gas-Shift reaction, Pt supported CeO<sub>2</sub> catalyst is known as one of the most active catalysts in Water-Gas-Shift reaction [9]. Therefore, to understand the extraordinary catalytic activity of PGM supported catalysts, one must understand what role the metal-support interaction plays in catalysis. Various strategies have been developed to tune the metal-support interaction to improve catalytic performances where many good review papers exist introducing different strategies and categorizing them by their respective standards. For example, Gorte et al. introduced the opportunities for tailoring metal-support interaction mainly by modifying the catalysts’ morphology; ex-solution catalysts (e.g. perovskite catalysts), inverse catalysts (incorporating oxides onto bulk metals, rather than loading PGMs on metal oxides) and core-shell catalysts (PGMs encapsulated in metal oxides) [10]. Recently, de Jong et al. have categorized strategies for controlling metal-support interaction into three categories; by modifying the support, by modifying the metal nanoparticle and by using post-treatment methods [11]. They emphasized that by adopting the proper strategy, the catalytic performance in C1 chemistry could be enhanced by an order of ~20 under industrially relevant conditions [11]. In this context, the tuning of

metal-support interaction is getting the great research attention recently, and there are still needs to develop appropriate strategies to manipulate metal-support interactions to improve catalytic performances.

In modifying the metal-support interaction, it would be best if the simple strategy could have the greatest effects. Recent advances in surface science chemistry have allowed the chemical composition, morphology, or even metal-supporting interactions of catalysts to be manipulated in a sophisticated manner. By assembling the ideal catalyst in several stages in a laboratory environment, the catalyst performance could be greatly improved. However, if the modification methodology is too complex, even if the catalytic performance is greatly improved, such a strategy will have industrially limited applicability. Thus, while modifying the metal-supporting interaction opens the opportunity to significantly improve the catalytic activity, it should be emphasized that the strategy for tailoring the metal-supporting interaction should be as simple as possible to attain industrial importance.

## **1.2. CO oxidation**

1 mole of CO reacts with 0.5 mole of O<sub>2</sub> to be oxidized to 1 mole of CO<sub>2</sub> ( $\text{CO} + 1/2 \text{O}_2 = \text{CO}_2$ ). CO oxidation has been frequently employed as the probe reaction in surface chemistry to investigate the surface properties of various materials. For this reason, there is an extensive literature examining the CO oxidation activity of a wide variety of materials. In this context, CO oxidation would be the good probe

reaction to investigate the validity of strategies manipulating the metal-support interaction to improve catalytic activities.

In addition, improving the CO oxidation performance has the significance in developing automotive exhaust catalysts [12]. To improve the fuel efficiency, lean-gasoline and diesel vehicles should implement high air to fuel ratio, which reduces the exhaust temperature. Since CO is one of the major toxic exhaust gas from vehicles, the need for developing catalysts with high CO oxidation ability at low temperature (as low as 150 °C) is emerging [13].

### **1.3. Water-Gas-Shift reaction**

1 mole of CO reacts with 1 mole of H<sub>2</sub>O to produce 1 mole of H<sub>2</sub> and 1 mole of CO<sub>2</sub> ( $\text{CO} + \text{H}_2\text{O} = \text{H}_2 + \text{CO}_2$ ). The purpose of the reaction is to remove CO from the H<sub>2</sub> feed, which could poison the Pt electrodes of the fuel cell. In order to take advantage of both the thermodynamics and kinetics of the reaction, the industrial scale Water-Gas-Shift (WGS) reaction is performed in multiple stages consisting of high-temperature (HT) WGS followed by low-temperature (LT) WGS. HT WGS takes advantage of the high reaction rate, but the reaction is limited by thermodynamics. The exit gas of HT WGS usually contains about 2-4 % of CO. LT WGS can avoid the thermodynamic constraints and decrease the CO concentration of exit gas below 1 %. The operating temperature window of HT WGS and LT WGS are 350-450 °C and 200-250 °C, respectively.

The important limitation for HT WGS is that the high temperature and the low H<sub>2</sub>O/CO ratio result in the promotion of side reactions such as methanation reaction. Excess amount of H<sub>2</sub> is always included in the reaction feed of practical operation, where 3 moles of H<sub>2</sub> could react with 1 mole of CO to produce 1 mole of CH<sub>4</sub> and 1 mole of H<sub>2</sub>O ( $\text{CO} + 3\text{H}_2 = \text{CH}_4 + \text{H}_2\text{O}$ ). Therefore, the ideal HT WGS catalysts should possess both the high activity and the high selectivity to H<sub>2</sub> and CO<sub>2</sub>.

## 1.4. Objectives

In this thesis, how the metal-support interaction influences the chemical properties of PGMs supported catalysts was investigated. In addition, three different strategies have been implemented to tailor the metal-support interaction in a simple but effective manner to improve catalytic performances.

In Chapter 2, how the interaction between PGMs (e.g. Pt) and metal oxide (e.g. CeO<sub>2</sub>) could improve the thermal stability of PGMs supported samples was investigated. Supported Pt improved the thermal stability of CeO<sub>2</sub> supports by forming strong Pt-O-Ce bonds [14].

In Chapter 3, CO oxidation abilities of PGMs supported catalysts (Pt/CeO<sub>2</sub> and Pt/TiO<sub>2</sub>) were improved by weakening the metal-support interactions. To weaken Pt-CeO<sub>2</sub> interaction, defect concentration of CeO<sub>2</sub> surface was decreased by the simple thermal treatment before loading Pt [15]. When Pt-CeO<sub>2</sub> interaction was

weakened by decreasing the defect concentration of CeO<sub>2</sub>, T<sub>50</sub> (temperature of 50 % conversion) of CO oxidation shifted 76 °C to the lower temperature [15]. In addition, to weaken Pt-TiO<sub>2</sub> interaction, S-doped TiO<sub>2</sub> was used as the support where S dopants hindered the intimate contact between Pt nanoparticles and TiO<sub>2</sub> [16]. When Pt-TiO<sub>2</sub> interaction was weakened by S dopants, T<sub>50</sub> of CO oxidation shifted 50 °C to the lower temperature [16].

In Chapter 4, by tailoring the metal-support interaction, HT WGS performance of Pt/CeO<sub>2</sub> catalyst was improved. By modulating the catalyst's geometry, the methanation reaction during HT WGS could be successfully suppressed while maintaining the high HT WGS activity of Pt/CeO<sub>2</sub>. Such improvement was accomplished by destroying the catalyst's structure and forming the thin CeO<sub>2</sub> over-layers on Pt nanoparticles. While methanation reaction, the reaction of 1 mol of CO with 3 mol of H<sub>2</sub> to produce 1 mol of H<sub>2</sub>O and 1 mol of CH<sub>4</sub> ( $\text{CO} + 3\text{H}_2 = \text{CH}_4 + \text{H}_2\text{O}$ ), occurs mainly on the Pt surface, the CeO<sub>2</sub> over-layers on Pt nanoparticles suppressed the CH<sub>4</sub> production by blocking the accessible Pt surface sites. In addition, the electronic interaction between Pt and CeO<sub>2</sub> over-layers granted the catalytic activity to CeO<sub>2</sub> surface which is originally inactive in WGS reaction.

# **Chapter 2. How Pt interacts with CeO<sub>2</sub> under the reducing and oxidizing environments at elevated temperature? The origin of improved thermal stability of Pt/CeO<sub>2</sub> compared to CeO<sub>2</sub>**

## **2.1. Introduction**

Platinum group metals (PGMs) are widely used as catalytically active phase in catalyst. Their unique electronic d-band structure allows them to be applied in many kinds of different reactions including CO oxidation [2, 4, 13, 17, 18], methane oxidation [19-21], hydrogenation [6, 22] and Water-Gas-Shift reaction [9, 23-27]. PGMs should be well dispersed on supports to increase the cost-effectiveness because of their high price. When PGMs are dispersed on supports, PGM and support interact electronically with each other, which brings about the characteristic physiochemical effects on their catalytic properties [9]. In this regard, PGM-support interaction has been the interesting issue for the past several decades [11].

Alumina and CeO<sub>2</sub> are widely used as the support materials, which can be regarded as the representative non-reducible and reducible oxides, respectively. When CeO<sub>2</sub> is exposed to oxidizing or reducing environment, it can readily change oxidation states between Ce<sup>3+</sup> and Ce<sup>4+</sup>, while alumina is relatively very stable [28-30]. Such typical physiochemical difference between CeO<sub>2</sub> and alumina causes a

significant effect on the interaction with PGM [30]. The interaction between PGM and alumina is known to be weaker than that of PGM and CeO<sub>2</sub>, which gives rise to PGM sintering at lower temperature in alumina support, resulting in lower PGM dispersion at higher temperature [31]. Thus, minimizing the metal sintering at higher temperature (> 700 °C) remains a great challenge to make more durable catalyst.

Meanwhile, it is known that PGM and CeO<sub>2</sub> strongly interact with each other. Consequently, relatively high dispersion of PGM can be maintained even after high temperature treatment. Based on the EXAFS spectroscopy, which demonstrated the formation of strong Pt-O-Ce bond, Nagai et al. reported that Pt-CeO<sub>2</sub> interaction plays a critical role in retaining the high platinum dispersion even after treatment at 800 °C [31]. Farmer and Campbell also reported that CeO<sub>2</sub> suppresses the metal sintering through the strong metal support interaction [32]. Their calorimetric measurement showed that small Ag particles are more stabilized on reduced CeO<sub>2</sub>(111) than on MgO(100), which provides a strong evidence about the excellent sintering resistance of PGM on CeO<sub>2</sub> support [32].

The strong interaction between Pt and CeO<sub>2</sub> has been shown to be beneficial for the catalytic reactions [33]. For example, Pt on CeO<sub>2</sub> can catalyze CO oxidation at low temperature because CeO<sub>2</sub> is able to spill-over atomic oxygen to neighboring Pt where CO is bonded (Mars-van Krevelen mechanism) [34, 35]. In addition, Pt-CeO<sub>2</sub> interaction promotes Water-Gas-Shift (WGS) reaction. Pt/CeO<sub>2</sub> catalyst showed the order of magnitude higher WGS reaction activity than that of individual Pt or CeO<sub>2</sub> [9]. Based on DFT calculation, Rodriguez et al. claimed that the changes

in electronic band structure of Pt and CeO<sub>2</sub> facilitates water dissociation on catalyst surface, which is considered to be the rate-determining step in WGS reaction [9].

In this regard, understanding of metal- CeO<sub>2</sub> interaction is of practical importance to provide the rational design of CeO<sub>2</sub> supported PGM catalysts. Especially, the comprehensive understanding of PGM-CeO<sub>2</sub> interaction under both reducing and oxidizing conditions is crucial, because PGM-CeO<sub>2</sub> catalysts can be utilized under both reaction conditions. For example, when PGM-CeO<sub>2</sub> catalysts are to be used as diesel oxidation catalysts (DOC), it encounters excess oxygen for CO and hydrocarbon oxidation [12]. In this case, understating metal-support interaction under oxidizing condition becomes important. On the other hand, in the case of WGS reaction, catalysts should eliminate CO under the reducing environment [36]. Therefore, understating metal-support interaction under reducing condition is important.

In this contribution, CeO<sub>2</sub> with high surface area [120 m<sup>2</sup>/g] was used to maximize Pt-CeO<sub>2</sub> interaction, and to understand the role of Pt-CeO<sub>2</sub> interaction in the thermal stability of CeO<sub>2</sub> [14]. The Pt-CeO<sub>2</sub> interaction under oxidizing/reducing environments was investigated in detail. The Pt-CeO<sub>2</sub> interaction has been extensively investigated by combining various characterization methods including X-ray diffraction (XRD), N<sub>2</sub> adsorption/desorption (BET/BJH), H<sub>2</sub> temperature programmed reduction (TPR), CO-chemisorption, X-ray photoelectron spectroscopy (XPS) and in-situ & ex-situ Raman spectroscopy [14].

## 2.2. Experimental

**Catalyst Synthesis.** CeO<sub>2</sub>, obtained from Rhodia, had a surface area of 120 m<sup>2</sup>/g. Pt was impregnated on CeO<sub>2</sub> by the incipient wetness impregnation method with aqueous Pt(NH<sub>3</sub>)<sub>4</sub>(NO<sub>3</sub>)<sub>2</sub> (Sigma Aldrich, 99.99 % grade, metal basis) solution as a metal precursor at room temperature. After the impregnation procedure, the catalysts were dried at 100 °C for 24 h. Dried samples were further treated in flowing 100 mL/min of 15 %O<sub>2</sub>/N<sub>2</sub> or 10 %H<sub>2</sub>/N<sub>2</sub> or N<sub>2</sub> for 2 h at the selected temperature. As shown in Figure 2-1, several notations were used to represent the treatment condition. Varied Pt loading was denoted as Pt(x)/CeO<sub>2</sub>, where the parenthesis value is the wt% of Pt in the sample. In the case of sequentially treated samples, oxidizing and reducing conditions were also denoted after the sample name. For example, Pt(2)/CeO<sub>2</sub> 500C 800R was prepared by oxidizing Pt(2)/CeO<sub>2</sub> sample at 500 °C for 2 h, followed by reducing Pt(2)/CeO<sub>2</sub> 500C sample at 800 °C for 2 h.

**The powder X-ray diffraction (XRD).** XRD patterns were taken by a Rigaku (model smartlab) diffractometer with Cu K $\alpha$  radiation ( $\lambda=0.1542$  nm). The voltage and current of X-ray were 40 kV and 50 mA, respectively. The patterns were collected in a 2 $\theta$  range from 5 ° to 90 ° with the scanning step size of 0.02 ° at a speed of 2.5 °/min.

**Surface area measurement.** N<sub>2</sub> adsorption/desorption isotherms were measured on a Micromeritics ASAP 2010 apparatus at liquid N<sub>2</sub> temperature of -196 °C. Before analysis, all catalysts were pretreated at 300 °C for 4 h under evacuation condition. The pore size distribution and specific surface area were calculated by using the

Barrett-Joyner-Halenda (BJH) and Brunauer-Emmett-Teller (BET) methods, respectively.

**H<sub>2</sub> temperature programmed reduction (TPR).** H<sub>2</sub>-TPR was performed to study the reducibility of various Pt/CeO<sub>2</sub> samples in a BET-CAT-BASIC (BEL Japan Inc.) with a thermal conductivity detector (TCD). All catalysts were pretreated in a flow of He (50 ml/min) at 350 °C for 2 h. After cooling down to room temperature, catalysts were exposed to 5 %H<sub>2</sub>/Ar (50 ml/min) and heated from room temperature to 900 °C with a heating rate of 10 °C/min.

**CO chemisorption.** CO chemisorption was measured on a Micromeritics ASAP 2010 following previously reported procedure with slight variations [37, 38]. 0.2 g of sample was placed in between the quartz wool in the U-shaped quartz tube. Samples were pretreated at 300 °C for 4 h under vacuum condition prior to the analysis. During analysis, after evacuation at room temperature, samples were reduced with H<sub>2</sub> gas at the desired temperature to reduce metal oxides. Reduction temperature of 200, 350, and 500 °C were used. After the subsequent evacuation at 400 °C for 2 h to desorb the surface bound H species, temperature was cooled down to 35 °C to perform CO chemisorption. CO pressure was varied from 10 to 70 kPa to obtain the CO adsorption isotherms. After the first CO adsorption isotherm was obtained, sample was evacuated at 35 °C for 4 h to desorb physisorbed CO. The second CO isotherm was obtained to measure the amount of physisorbed CO. The difference between the first and the second CO isotherms corresponds to the chemisorbed CO. CO pressure was extrapolated to zero pressure to estimate the amount of chemisorbed CO.

**X-ray photoelectron spectroscopy (XPS).** XPS analysis was conducted on a AXIS-HSi (Kratos) instrument with Mg K $\alpha$  radiation of 450 W. The charging effects were corrected with respect to the C 1s binding energy of 284.5 eV. The spectra were processed using the software casaXPS. The chemical composition of the catalysts was calculated using the integral intensities of the lines or their components, subject to the atomic sensitivity factors [39].

**Ex-situ and In Situ Raman Spectroscopy.** The Raman spectra of the series of Pt/CeO<sub>2</sub> samples were collected with a BaySpecNomadic<sup>TM</sup> Raman spectrometer equipped with a confocal microscope (Olympus BX-51 upright microscope), volume phase gratings, and a dichroic filter. The catalysts were excited with 532 nm excitation (DPSS, CW, diode-pumped solid state continuous wave, max power, 50 mW) in the 300–1500 cm<sup>-1</sup> Raman shift regions. The scattered photons were focused onto a CCD detector (2048x64 pixels), with a spectral resolution of 4 cm<sup>-1</sup>. For the in-situ Raman spectroscopy, 40 mg of powdered sample was loosely spread on the ceramic sample holder inside the environmental cell (LinkamCCR1000). Prior to reduction, Pt/CeO<sub>2</sub> sample was dehydrated by heating the cell at 350 °C under 3 % O<sub>2</sub>/Ar (Airgas, 30 mL/min) for 30 min. The reduction was carried out under 3 % H<sub>2</sub>/Ar (Airgas, 30 mL/min). The sample was heated to the desired temperatures (50 °C ~250 °C) and held for 20 min. In-situ Raman spectra was collected under 30 mL/min He (Praxair, UHP) after cooling down to 50 °C. A spectral acquisition was done with 5 scans of 100 sec/scan, for a total acquisition time of ~9 min per spectrum in both ex-situ and in-situ Raman spectra.

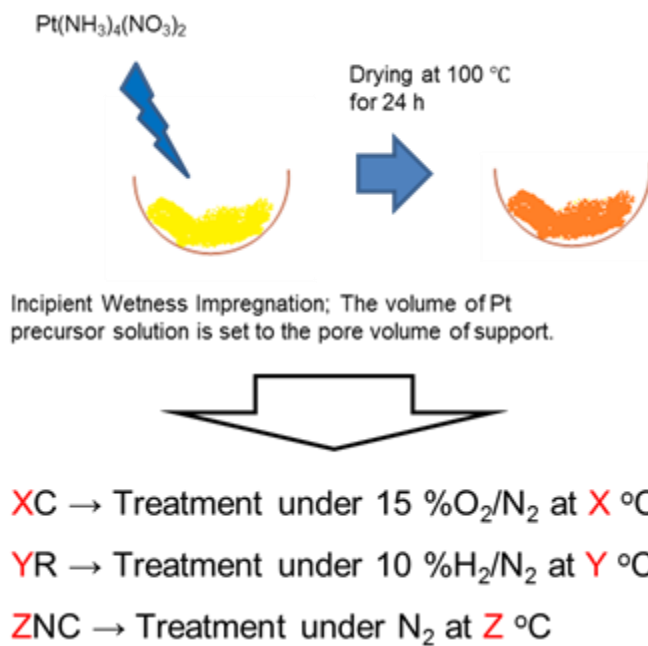


**Figure 2-1.** Sample preparation procedure and the notation of samples

## 2.3. Results

**2.3.1. Position of Pt on CeO<sub>2</sub> under oxidizing and reducing condition** H<sub>2</sub> TPR profiles of CeO<sub>2</sub> and Pt(2)/CeO<sub>2</sub> 500C are shown in Figure 2-2. Two reduction peaks at ~465 °C and ~780 °C are observed on CeO<sub>2</sub> sample, which originate from the reduction of surface and bulk of CeO<sub>2</sub>, respectively [40]. It is known that the bulk oxygen is caged in the fluorite structure of CeO<sub>2</sub> and requires high temperature to react with H<sub>2</sub>, while surface oxygen of CeO<sub>2</sub> is under-coordinated (2 to 3 instead of 4) and can react with H<sub>2</sub> at lower temperature [40]. When 2 wt% of Pt is impregnated on CeO<sub>2</sub>, two reduction peaks centered at 100 °C and 780 °C appeared. It is widely accepted that Pt spills over hydrogen to the neighboring CeO<sub>2</sub> surface, which subsequently facilitates the reduction of the CeO<sub>2</sub> surface at lower temperature [41, 42]. It is known that Pt-O-Ce species, formed by the strong interaction between Pt and CeO<sub>2</sub>, are reduced at temperature in the range of 40 ~ 250 °C, while bulk Pt oxides such as PtO and PtO<sub>2</sub> species are reduced below room temperature due to the weak interaction with CeO<sub>2</sub> [43, 44]. Note that the amount of H<sub>2</sub> consumed below 200 °C on Pt(2)/CeO<sub>2</sub> 500C (0.284 mmol/g) is larger than the amount of Pt loaded (0.103 mmol/g). This result supports that not only Pt-O-Ce but also the surface oxygen of CeO<sub>2</sub> react with H<sub>2</sub>, which leads to the formation of metallic Pt and surface oxygen vacancies, respectively. On the contrary to the behavior of surface oxygen, the bulk oxygen of CeO<sub>2</sub> was hardly affected by the presence of Pt as seen in Figure 2-2. This implies that the interaction between Pt and CeO<sub>2</sub> is confined to the surface region of CeO<sub>2</sub>. Sanchez et al. previously suggested that the cerium cations create a diffusion

barrier and restrict the metal-support interaction between PGM and reducible oxide to the surface region [40].

Static CO chemisorption has been widely used to measure the dispersion of precious metal on supported catalysts. Exposed PGM atom can make bond with CO at 1:1 stoichiometry so that the adsorbed amount of CO provides the number of exposed PGM sites. However, CO chemisorption is known to overestimate the PGM dispersion of CeO<sub>2</sub> supported catalysts, because CO can also be adsorbed on CeO<sub>2</sub> [45, 46]. Papavasiliou et al. tried to count separately the number of CO adsorbed on Pt from that on CeO<sub>2</sub> by spectroscopic method to avoid the overestimation [45]. They integrated the IR peak arising from CO adsorbed on Pt, and excluded CO adsorbed on CeO<sub>2</sub> from their consideration [45]. Even though CO chemisorption would overestimate the Pt dispersion on Pt/CeO<sub>2</sub>, it could provide the valuable information of Pt-CeO<sub>2</sub> interaction. Table 2-1 shows the amount of chemisorbed CO on CeO<sub>2</sub> 500C after the reductive treatment at 200, 350, and 500 °C, as well as on Pt(2)/CeO<sub>2</sub> 500C after the reductive treatment at 200 and 350 °C. Trace amounts of CO were chemically adsorbed on CeO<sub>2</sub> 500C (200R). When reduction temperature was raised to 350 °C and 500 °C, the amounts of chemisorbed CO were increased to 0.04 and 0.133mmol/g, respectively. Such results are in consistent with H<sub>2</sub> TPR of Figure 2-2 that the extent of reduction of CeO<sub>2</sub> surface increased with increasing temperature. Combined H<sub>2</sub>-TPR and CO chemisorption results provide the correlation between the reduction temperature of CeO<sub>2</sub> and the amounts of chemisorbed CO. It can be inferred that CO adsorbs on the oxygen vacancies of CeO<sub>2</sub> surface.

In the case of Pt(2)/CeO<sub>2</sub> 500C sample, there was no difference in the amount of CO chemisorption after the reductive treatment at 200 and 350 °C, as shown in Table 2-1. Such phenomenon can be explained by H<sub>2</sub> TPR of Pt(2)/CeO<sub>2</sub> in Figure 2-2, where Pt(2)/CeO<sub>2</sub> 500C surface was fully reduced below 200 °C. It should be noted that when Pt(2)/CeO<sub>2</sub> 500C surface was fully reduced at 200 or 350 °C (Figure 2-2), the amount of CO chemisorbed (0.132mmol/g) was comparable to that on CeO<sub>2</sub> 500C, after the reductive treatment at 500 °C (0.133 mmol/g). This result implies that Pt could not increase the amount of chemisorbed CO on Pt/CeO<sub>2</sub>. Therefore, after the reductive pretreatment of Pt/CeO<sub>2</sub>, Pt would be located on the surface oxygen vacancies of CeO<sub>2</sub> surface. Although both Pt and oxygen vacancies of CeO<sub>2</sub> can adsorb CO, the presence of Pt in the surface oxygen vacancy does not increase the amount of chemisorbed CO. Similarly, Sanchez et al. suggested that metal atoms are anchored on the oxygen vacancies on the support, which they named it 'nesting' model [40].

Figure 2-3 displays the Raman spectra of CeO<sub>2</sub> 500C, Pt(0.05)/CeO<sub>2</sub> 500C, and Pt(2)/CeO<sub>2</sub> 500C. Raman spectra on Figure 2-3 are normalized with respect to the Raman signal at 460 cm<sup>-1</sup>. According to Daniel and his coauthor, the main peak at ~460 cm<sup>-1</sup> can be attributed to triply degenerate F<sub>2g</sub> mode of CeO<sub>2</sub> with fluorite structure, while the peaks at 600 and 1180 cm<sup>-1</sup> can be assigned to defect induced (D) mode and second-order longitudinal optical (2LO) mode of CeO<sub>2</sub>, respectively [47]. When 0.05 wt% of Pt was impregnated on CeO<sub>2</sub>, those Raman peaks still remained but with decreased intensity. For the case of Pt(2)/CeO<sub>2</sub> 500C, Raman peaks at 600

and  $1180\text{ cm}^{-1}$  disappeared and new peaks at  $567$  and  $655\text{ cm}^{-1}$  emerged. According to Brogan et al., Raman peaks at  $567$  and  $655\text{ cm}^{-1}$  can be assigned to the bridging Pt-O-Ce vibration and Pt-O vibration of Pt-O-Ce bond, respectively [48]. Therefore, when Pt is impregnated on  $\text{CeO}_2$ , it forms Pt-O-Ce bonds with  $\text{CeO}_2$  surface.

Figure 2-4 presents in-situ Raman spectra of Pt(2)/ $\text{CeO}_2$  500C (a) and 800C (b) obtained at elevated temperature under the reducing condition from 50 to 250 °C. The Pt-O-Ce Raman bands at  $567$  and  $\sim 655\text{ cm}^{-1}$  disappeared at 200 and 225 °C in the Raman spectra of Pt(2)/ $\text{CeO}_2$  500C and 800C samples, respectively. The comparison between Pt(2)/ $\text{CeO}_2$  500C and 800C will be further addressed later with the  $\text{H}_2$  TPR experiment. In addition, it was observed that Raman peak at  $460\text{ cm}^{-1}$ , the main Raman peak from  $\text{CeO}_2$ , was weakened under the  $\text{H}_2$  flow. Surface defects, such as oxygen vacancy, would weaken and broaden the Raman intensity from  $\text{CeO}_2$  [49].

The reduction temperature of  $\text{PtO}_x$  on different oxide supports were reported previously [50]. Using the in-situ Raman spectroscopy, Lin et al. observed that  $\text{PtO}_x$  phase on  $\text{CeO}_2$  is more stable under reducing environment than that on  $\text{Al}_2\text{O}_3$  and  $\text{SiO}_2$  supports [50]. The authors reported that Pt-O-Ce bonds can maintain up to 150 °C under the reducing condition, in good agreement with our results [50].

Figure 2-5 depicts the schematic diagram to explain the changes in Pt/CeO<sub>2</sub> system after the oxidative and reductive treatment. As noticed from Raman spectra of Figure 2-3, when Pt is impregnated on CeO<sub>2</sub> and exposed to the oxidation environment, Pt-O-Ce bond was formed (Figure 2-5 (a)). Under the reducing treatment above 250 °C, however, Pt-O-Ce bond disappeared and Pt could be located on the oxygen vacancy of CeO<sub>2</sub> surface (Figure 2-5 (b)). In agreement with the present result, Zhang et al. suggested that Au is strongly bound on surface oxygen vacancies of CeO<sub>2</sub>, based on their DFT study [51]. After the reduction treatment at higher temperature (~ 500 °C), deformation of CeO<sub>2</sub> structure can occur significantly because bulk oxygen in CeO<sub>2</sub> is reduced. The role of surface oxygen and bulk oxygen of CeO<sub>2</sub> in terms of the thermal stability is further addressed in the next section.

| <b>Sample</b>                     | <b>In-situ reduction temperature (°C)</b> | <b>The amount of CO chemisorbed (mmol/g)</b> |
|-----------------------------------|---|--|
| <b>CeO<sub>2</sub> 500C</b>       | 200                                       | ~0   |
|                                   | 350                                       | 0.041  |
|                                   | 500                                       | 0.133  |
| <b>Pt(2)/CeO<sub>2</sub> 500C</b> | 200                                       | 0.135  |
|                                   | 350                                       | 0.132  |

**Table 2-1.** The amount of chemisorbed CO on CeO<sub>2</sub> and Pt(2)/CeO<sub>2</sub>, after in-situ reduction treatment at different temperature.

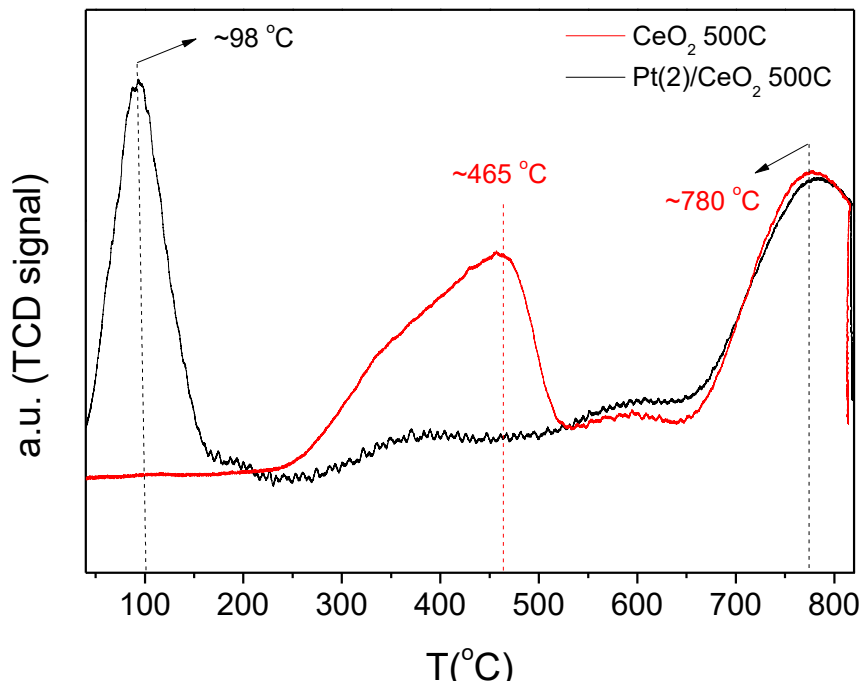


**Figure 2-2.** H<sub>2</sub> Temperature Programmed Reduction curves of CeO<sub>2</sub> 500C and Pt(2)/CeO<sub>2</sub> 500C samples.

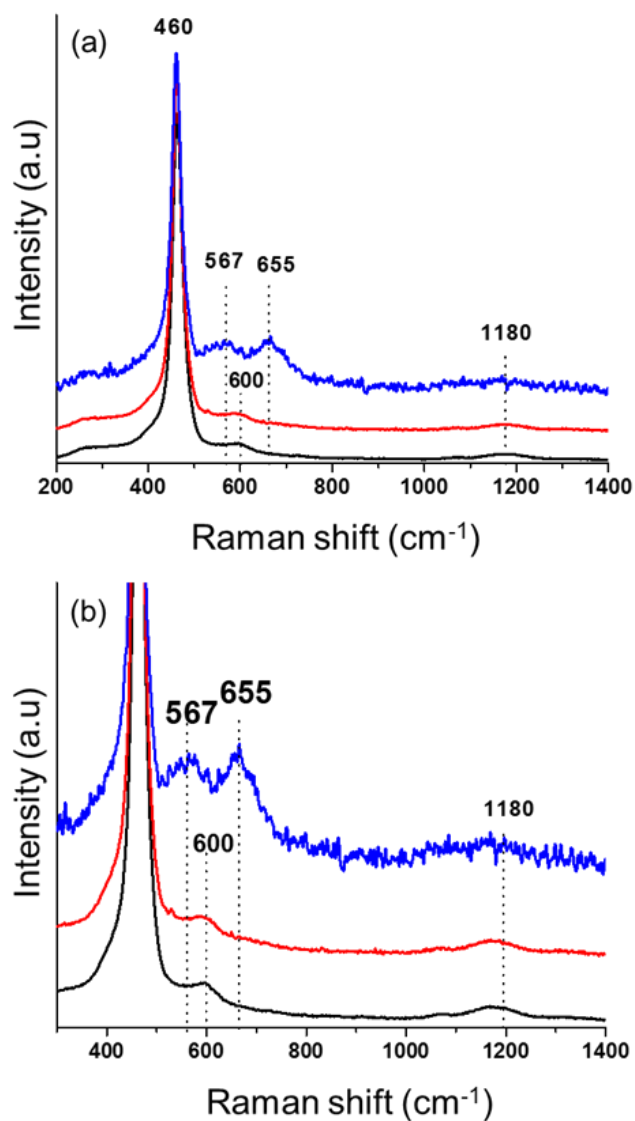


**Figure 2-3.** (a) Ex-situ Raman spectra of CeO<sub>2</sub> 500C, Pt(0.05)/CeO<sub>2</sub> 500C and Pt(2)/CeO<sub>2</sub> 500C samples (from bottom to top). (b) Magnified region of 300 cm<sup>-1</sup>~1400 cm<sup>-1</sup>.

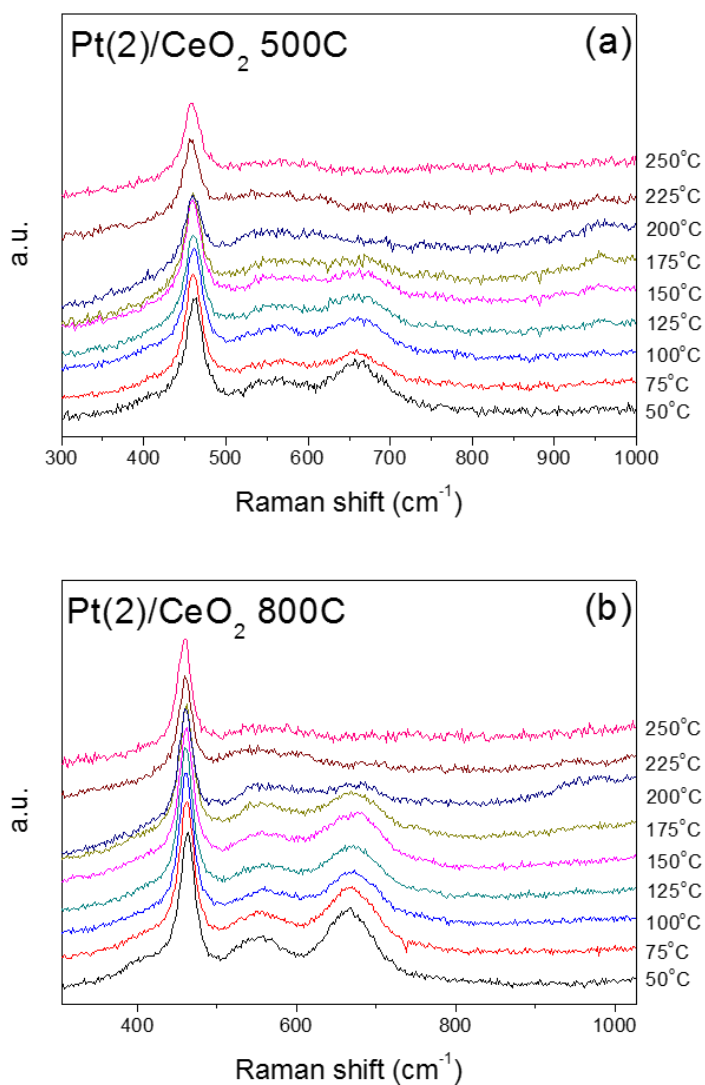
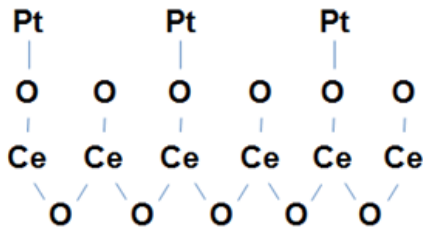


**Figure 2-4.** In-situ Raman spectra of Pt(2)/CeO<sub>2</sub> (a) 500C and (b) 800C obtained at temperature from 50 °C to 250 °C with a temperature step of 25 °C, under the reducing condition. 20 min was maintained at each temperature and spectra were obtained after cooling down to 50 °C.

(a) After oxidation



(b) After mild reduction

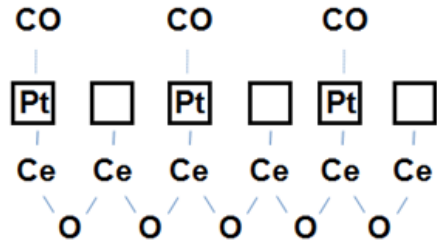


**Figure 2-5.** (a) After the oxidative treatment, Pt-O-Ce bond is formed between Pt and CeO<sub>2</sub>. CeO<sub>2</sub> surface is also oxidized. (b) After the reductive treatment, CeO<sub>2</sub> surface is reduced and oxygen vacancies are generated on the surface. Pt is located in the oxygen vacancies.

**2.3.2. The role of Pt-O-Ce bond in the thermal stability of CeO<sub>2</sub>** Figure 2-6 shows the XRD patterns of CeO<sub>2</sub> and Pt(2)/CeO<sub>2</sub> samples, after oxidation at various temperatures. XRD peaks at 28.7 °, 33.2 °, 47.5 °, 56.4 °, 59.2 °, 69.5 °, 79.3 °, and 88.6 ° can be attributed to the Miller indices (111), (200), (220), (311), (222), (400), (331), and (420) of the cubic lattice of CeO<sub>2</sub> (CaF<sub>2</sub> structural type), respectively. Note that XRD peaks related to Pt were not observed on XRD patterns of Pt(2)/CeO<sub>2</sub> (Metallic Pt phase gives a characteristic XRD peak at 40 °). XRD peaks of CeO<sub>2</sub> grow sharper when treated under the oxidizing condition at higher temperature (Figure 2-6 (a)). On the other hand, XRD patterns of Pt(2)/CeO<sub>2</sub> were not changed with increasing oxidation temperatures from 500 to 800 °C, where the crystalline size of CeO<sub>2</sub> in Pt/CeO<sub>2</sub>, calculated from Scherrer equation, hardly changed as summarized in Table 2-2. Enhancement in thermal stability of CeO<sub>2</sub> with Pt deposition was evident even after the oxidative treatment at 1000 °C. Crystalline size (from XRD) of CeO<sub>2</sub> 1000C was 44.3 nm, while that of Pt(2)/CeO<sub>2</sub> 1000C was 29.8 nm (data not shown).

Figure 2-7 shows the pore size distribution curves of CeO<sub>2</sub> and Pt(2)/CeO<sub>2</sub> samples obtained after different treatments. When CeO<sub>2</sub> was oxidized at 800 °C, its pore structure collapsed and the mean pore size increased from 9.6 to 16.9 nm (Figure 2-7 (a)). Pt(2)/CeO<sub>2</sub>, on the other hand, maintained its pore structure even after the oxidation treatment at 800 °C. In addition, surface area of CeO<sub>2</sub> was steadily decreased from 129 to 65 m<sup>2</sup>/g when the calcination temperature was increased from 500 to 800 °C. The change in the textural property of Pt(2)/CeO<sub>2</sub> was completely different from the case of CeO<sub>2</sub>, where its BET surface area doubled that of CeO<sub>2</sub>

after the 800 °C treatment (Table 2-2). N<sub>2</sub> adsorption/desorption results are in good agreement with the XRD result that the presence of Pt strengthens the thermal stability of CeO<sub>2</sub>. Recently, Jones et al. also observed that atomic Pt trapped on CeO<sub>2</sub> surface helps to preserve the surface area of CeO<sub>2</sub> from high temperature aging treatment [52].

To further investigate the role of surface oxygen in the thermal stability of CeO<sub>2</sub>, surface oxygen of Pt(2)/CeO<sub>2</sub> was selectively removed at 250 °C by H<sub>2</sub> and temperature was raised to 800 °C under the inert N<sub>2</sub> atmosphere (Pt(2)/CeO<sub>2</sub> 500C 250R 800NC). N<sub>2</sub> treatment at 800 °C is expected to induce the thermal effect without reducing surface or bulk of Pt/CeO<sub>2</sub>. Figure 2-7 (b) shows that when the surface oxygen was selectively removed at 250 °C, in other words, in the absence of Pt-O-Ce bond, the pore structure of Pt(2)/CeO<sub>2</sub> collapsed at elevated temperature (Table 2-3). On the other hand, the pore structure and BET surface area of Pt(2)/CeO<sub>2</sub> did not change by the thermal treatment under N<sub>2</sub> flow (Pt(2)/CeO<sub>2</sub> 800NC and Pt(2)/CeO<sub>2</sub> 500C 800NC samples on Figure 2-7 (b) and Table 2-3). Therefore, the presence of surface oxygen would be crucial to obtain the excellent thermal stability of CeO<sub>2</sub>. When Pt(2)/CeO<sub>2</sub> 500C was treated at 800 °C under the reducing condition (Pt(2)/CeO<sub>2</sub> 500C 800R), where the CeO<sub>2</sub> bulk was reduced, the pore structure further collapsed, as evidenced by the highest mean pore diameter amongst the samples examined (Figure 2-7 (b)). Comparing Pt(2)/CeO<sub>2</sub> 500C 800R and Pt(2)/CeO<sub>2</sub> 500C 250R 800NC, it can be claimed that the presence of bulk oxygen is also important in maintaining the textural property of CeO<sub>2</sub>.

As can be noticed on Figure 2-7 (c), higher Pt content led to the improvement in thermal stability of Pt/CeO<sub>2</sub> (Table 2-3). Even a small amount of Pt addition (0.05 wt%) resulted in a noticeable improvement in maintaining the textural property. As was described on Raman spectra of Figure 2-3, Pt forms Pt-O-Ce bond on CeO<sub>2</sub> surface. As Pt loading increases from 0.05 wt% to 2 wt%, the mean pore diameter decreases from 11 to 7 nm on Figure 2-7, indicating that as more Pt is anchored with surface oxygen of CeO<sub>2</sub> to form Pt-O-Ce bonds more abundantly, the thermal stability of Pt/CeO<sub>2</sub> is improved significantly.

Combined BET (Table 2-2), BJH curve (Figure 2-7 (a)) and XRD (Figure 2-6) results strongly support that Pt/CeO<sub>2</sub> has the higher thermal stability than CeO<sub>2</sub> under the oxidizing environment. When Pt is impregnated on CeO<sub>2</sub>, it forms strong Pt-O-Ce bond with the surface oxygen of CeO<sub>2</sub> (Figure 2-3). When surface oxygen was selectively removed, Pt/CeO<sub>2</sub> could not endure the high temperature treatment at 800 °C (Figure 2-7 (b)). Also, the higher Pt loading resulted in the enhanced thermal stability of Pt/CeO<sub>2</sub> (Figure 2-7 (c)). Therefore, it should be claimed that when surface O-Ce species of CeO<sub>2</sub> are converted to Pt-O-Ce species, agglomeration of CeO<sub>2</sub> is suppressed. On the other hand, under the reducing condition where Pt-O-Ce bond disappears at elevated temperature (Figure 2-4), Pt cannot maintain the textural property of CeO<sub>2</sub> (Figure 2-7 (b)). The influence of the strong metal-support interaction on the suppression of the phase transition of metal was previously reported by Kwak et al., who showed that penta-coordinated Al<sup>3+</sup> sites on  $\gamma$ -Al<sub>2</sub>O<sub>3</sub> support play a key role in suppressing the phase transition of impregnated Pt species from

atomically dispersed to the two-dimensional raft state, based on the ultrahigh magnetic field NMR spectroscopy [53].

| Sample                                    | CeO <sub>2</sub> particle size <sup>a</sup> (nm) | surface area <sup>b</sup> (m <sup>2</sup> /g) | Pore volume <sup>c</sup> (cm <sup>3</sup> /g) | mean pore size <sup>c</sup> (nm) | Chemisorbed CO (mmol/g) | H <sub>2</sub> consumed <sup>d</sup> (mmol/g) |
|---|--|---|---|----------------------------------|-------------------------|---|
| CeO <sub>2</sub> 500C                     | 8.6  | 129   | 0.31  | 9.6                              | 0.138                   | 0.284   |
| CeO <sub>2</sub> 600C                     | 8.6  | 118   | 0.28  | 9.4                              | 0.161                   | 0.266   |
| CeO <sub>2</sub> 700C                     | 11.2   | 101   | 0.28  | 10.9                             | 0.084                   | 0.203   |
| CeO <sub>2</sub> 800C                     | 17.2   | 65  | 0.28  | 16.9                             | 0.032                   | 0.108   |
| Pt(2)/CeO <sub>2</sub> 500C               | 8.7  | 125   | 0.27  | 8.5                              | 0.134                   | 0.274   |
| Pt(2)/CeO <sub>2</sub> 600C               | 8.9  | 126   | 0.27  | 8.6                              | 0.165                   | 0.533   |
| Pt(2)/CeO <sub>2</sub> 700C               | 8.9  | 126   | 0.27  | 8.6                              | 0.161                   | 0.443   |
| Pt(2)/CeO <sub>2</sub> 800C               | 9.8  | 111   | 0.27  | 9.8                              | 0.135                   | 0.484   |
| Pt(2)/Al <sub>2</sub> O <sub>3</sub> 500C | -  | 219   | 0.43  | 8.1                              | 0.058                   | -   |

a. From XRD, Scherrer equation b. From N<sub>2</sub> adsorption branch, BET c. From N<sub>2</sub> desorption branch, BJH d. From H<sub>2</sub> TPR, integrated area below 500 °C

**Table 2-2.** Physiochemical properties of CeO<sub>2</sub>, Pt(2)/CeO<sub>2</sub> and Pt(2)/Al<sub>2</sub>O<sub>3</sub> samples, oxidized at various temperatures. In-situ reduction for CO chemisorption was proceeded at 350 °C for Pt/CeO<sub>2</sub> (and Pt/Al<sub>2</sub>O<sub>3</sub>) and 500 °C for CeO<sub>2</sub> samples.

| Sample                                    | Surface area <sup>a</sup><br>(m <sup>2</sup> /g) | Pore volume <sup>b</sup><br>(cm <sup>3</sup> /g) | Mean pore size <sup>b</sup><br>(nm) | H <sub>2</sub> consumed <sup>c</sup><br>(mmol/g) |
|---|--|--|-------------------------------------|--|
| Pt(0.05)/CeO <sub>2</sub> 800C            | 69   | 0.27   | 15.7                                | -  |
| Pt(0.5)/CeO <sub>2</sub> 800C             | 76   | 0.26   | 13.3                                | -  |
| Pt(2)/CeO <sub>2</sub> 500C               | 125  | 0.27   | 8.5                                 | 0.274  |
| Pt(2)/CeO <sub>2</sub> 800C               | 111  | 0.27   | 8.5                                 | 0.484  |
| Pt(2)/CeO <sub>2</sub> 500NC              | 128  | 0.27   | 8.5                                 | 0.317  |
| Pt(2)/CeO <sub>2</sub> 800NC              | 106  | 0.27   | 10                                  | 0.405  |
| Pt(2)/CeO <sub>2</sub> 500C<br>800NC      | 113  | 0.28   | 9.7                                 | 0.446  |
| Pt(2)/CeO <sub>2</sub> 500C<br>250R 800NC | 33   | 0.23   | 28.5                                | -  |
| Pt(2)/CeO <sub>2</sub> 500C<br>800R       | 17   | 0.18   | ~50                                 | -  |

a. From N<sub>2</sub> adsorption branch, BET b. From BJH curves obtained from N<sub>2</sub> desorption branch c. From

H<sub>2</sub> TPR, integrated area below 500 °C

**Table 2-3.** Physiochemical properties of Pt/CeO<sub>2</sub> samples, with various Pt loading and after different kinds of thermal treatments.

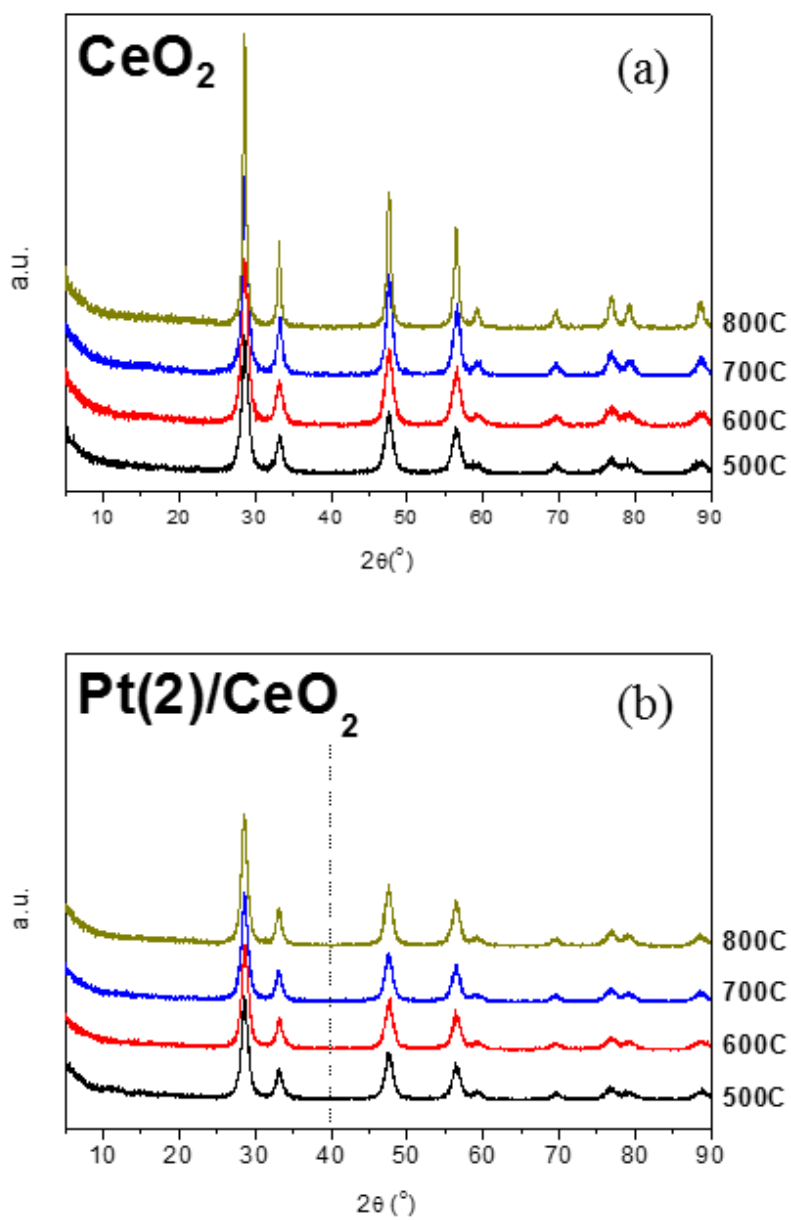


**Figure 2-6.** XRD patterns of (a)  $\text{CeO}_2$  and (b)  $\text{Pt}(2)/\text{CeO}_2$  samples, taken after oxidative treatment at 500, 600, 700 and 800  $^\circ\text{C}$  for 2 h.

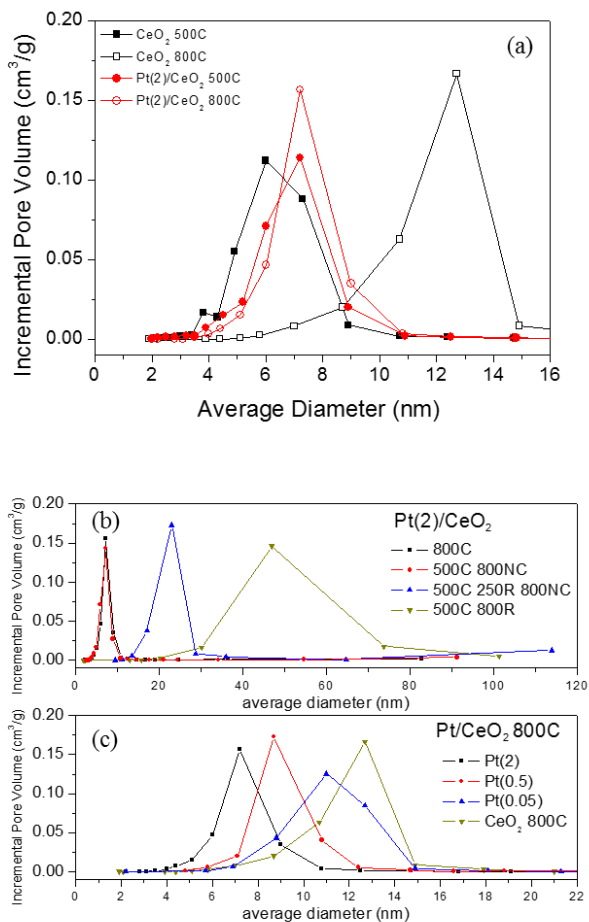


**Figure 2-7.** BJH pore size distribution curves of CeO<sub>2</sub> and Pt/CeO<sub>2</sub> samples. Desorption branch of N<sub>2</sub> was analyzed. (a) CeO<sub>2</sub> and Pt(2)/CeO<sub>2</sub> treated at 500 °C and 800 °C. (b) The role of surface oxygen and bulk oxygen of Pt(2)/CeO<sub>2</sub> 500C in sustaining the CeO<sub>2</sub> structure from high temperature treatment, (c) The effect of Pt loadings on the pore size distribution of Pt/CeO<sub>2</sub> under the oxidative condition.

**2.3.3. Pt-CeO<sub>2</sub> interaction under the oxidizing environment** Figure 2-8 shows H<sub>2</sub> TPR curves of Pt(2)/CeO<sub>2</sub> 500C, 600C, 700C and 800C. When the oxidation temperature was increased, the surface reduction peak gradually shifted to the higher temperature, while the bulk reduction peak was not affected. The maxima of surface reduction peak was shifted by 140 °C to the higher temperature in Pt(2)/CeO<sub>2</sub> 800C than Pt(2)/CeO<sub>2</sub> 500C. It is observed that surface of Pt(2)/CeO<sub>2</sub> 500C was fully reduced at 150 °C, while that of Pt(2)/CeO<sub>2</sub> 800C was hardly reduced until 150 °C. Such shift should be attributed to the change in Pt-CeO<sub>2</sub> interaction, since little structural change was observed on Pt(2)/CeO<sub>2</sub> after the oxidative treatment at high temperature based on XRD and BET results. The change in the interaction between Pt and CeO<sub>2</sub> is also in good agreement with the in-situ Raman spectra of Pt(2)/CeO<sub>2</sub> 500C and 800C on Figure 2-4. At reduction temperature of 150 °C, Raman signals from Pt-O-Ce bond almost disappeared on Pt(2)/CeO<sub>2</sub> 500C while it was appreciably visible on Pt(2)/CeO<sub>2</sub> 800C. To sum up, Pt-O-Ce bond on Pt(2)/CeO<sub>2</sub> 800C appeared to be more resistant against the reductive treatment than that on Pt(2)/CeO<sub>2</sub> 500C. Interesting to note is that the bulk reduction peak of CeO<sub>2</sub> at 800 °C was not affected for all samples by neither the presence of Pt nor the calcination temperature because Pt-CeO<sub>2</sub> interaction is confined on the surface region of CeO<sub>2</sub>.

XPS results of Pt(2)/CeO<sub>2</sub> 500C, 600C, 700C, and 800C are listed on Table 2-4. Comparing Pt(2)/CeO<sub>2</sub> after the oxidative treatment at 500 and 800 °C, Pt/Ce on surface was decreased from 0.063 to 0.042. In other words, when oxidation temperature was increased, relative Pt concentration on surface was decreased. Some extent of Pt sintering could be expected on Pt/CeO<sub>2</sub> when the temperature was raised. However, no metallic Pt phase was observed on XPS results of Pt(2)/CeO<sub>2</sub> 500C and 800C. In addition, no Pt related peaks were observed on XRD patterns of Pt(2)/CeO<sub>2</sub> 800C (Figure 2-6). It is known that the presence of metallic Pt facilitates the reduction of CeO<sub>2</sub> surface [50], which contradicts the shift of the surface reduction peak to the higher temperature after the oxidative treatment at high temperature (Figure 2-8). If Pt was agglomerated, the reduction peak should have shifted to the lower temperature. Hence, the decrease in Pt concentration on Pt(2)/CeO<sub>2</sub> after the oxidation at 800 °C, measured by XPS, does not seem to originate from Pt sintering. Instead, Pt would diffuse into CeO<sub>2</sub> at elevated temperature, resulting in lower relative Pt concentration as detected by XPS, making Pt-O-Ce bonds more resistive to the reductive treatments as observed by H<sub>2</sub> TPR. The Pt diffusion model at elevated temperature will be further explained later in the discussion section.

| <b>wt%</b>   | <b>Pt(2)/CeO<sub>2</sub><br/>500C</b> | <b>Pt(2)/CeO<sub>2</sub><br/>600C</b> | <b>Pt(2)/CeO<sub>2</sub><br/>700C</b> | <b>Pt(2)/CeO<sub>2</sub><br/>800C</b> |
|--------------|---------------------------------------|---------------------------------------|---------------------------------------|---------------------------------------|
| <b>Pt 4f</b> | 4.68                                  | 4.69                                  | 3.09                                  | 3.08                                  |
| <b>O 1s</b>  | 20.85                                 | 23.69                                 | 23.22                                 | 22.9                                  |
| <b>Ce 3d</b> | 74.47                                 | 71.62                                 | 73.7                                  | 74.02                                 |
| <b>Pt/Ce</b> | 0.063                                 | 0.065                                 | 0.042                                 | 0.042                                 |

**Table 2-4.** Relative surface concentration (wt%) of Pt, Ce, and O of Pt(2)/CeO<sub>2</sub> samples from XPS.

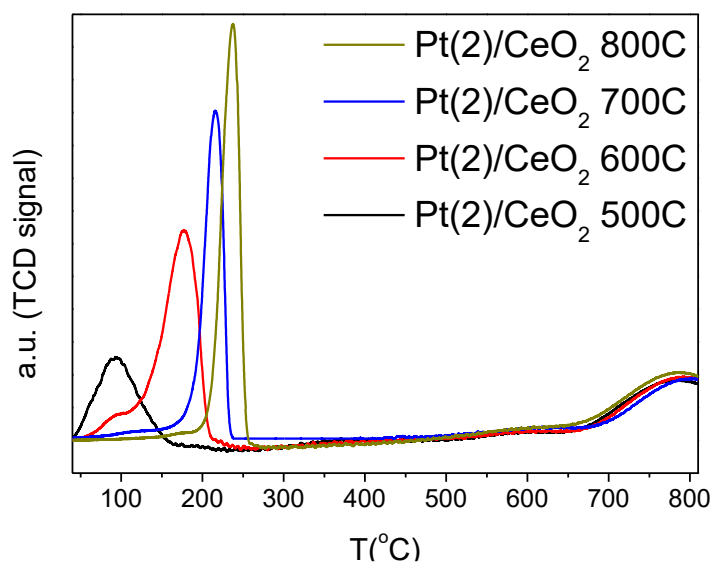


**Figure 2-8.** H<sub>2</sub> Temperature Programmed Reduction curves of Pt(2)/CeO<sub>2</sub> samples, after oxidation at 500, 600, 700 and 800 °C for 2 h.

## 2.4. Discussion

Figure 2-9 is the schematic explaining the changes in Pt/CeO<sub>2</sub> under the oxidizing environment at high temperature. BJH curve results indicate that when CeO<sub>2</sub> was treated at high temperature, CeO<sub>2</sub> structure collapsed (Figure 2-7 (a)). Crystalline size of CeO<sub>2</sub> also increased from 8.6 to 17.2 nm when the oxidation temperature was raised from 500 to 800 °C (Figure 2-6 and Table 2-2). However, when Pt is impregnated on CeO<sub>2</sub>, CeO<sub>2</sub> structure did not collapse (Figure 2-7 (b)), and the crystalline size of CeO<sub>2</sub> was only slightly increased from 8.7 to 9.8 nm upon the same thermal treatment (Figure 2-6 and Table 2-2). When Pt-nitrate is impregnated on CeO<sub>2</sub> and thermally treated above 200 °C, Pt-O-Ce bonds are formed between Pt and CeO<sub>2</sub> through the surface oxygen of CeO<sub>2</sub>, as evidenced by Raman spectra (Figure 2-3) [54]. Therefore, the strong Pt-O-Ce bonds would prevent the CeO<sub>2</sub> structure from collapsing during the high temperature treatment. However, since CeO<sub>2</sub> collapses at high temperature in the absence of Pt, Pt seems to diffuse into CeO<sub>2</sub> structure while maintaining the CeO<sub>2</sub> structure at high temperature, which could explain the decreased relative surface concentration of Pt on Pt(2)/CeO<sub>2</sub> 800C compared to Pt(2)/CeO<sub>2</sub> 500C, as evidenced by XPS (Table 2-4).

When Pt is impregnated on CeO<sub>2</sub>, the surface reduction peak (at ~450 °C) shifted to the lower temperature (~100 °C) (Figure 2-2). Pt is known to spill-over H<sub>2</sub> and facilitates the reduction of CeO<sub>2</sub> surface. Based on H<sub>2</sub> TPR results, Acerbi et al. proposed that the electronic interaction between precious metal and CeO<sub>2</sub> facilitates

the reduction of CeO<sub>2</sub> surface, and the d-band center of precious metal could be the important parameter in determining how the reducibility of the support is enhanced [44]. Lin et al. proposed that the metallic Pt, generated from the reduction of Pt-O species, promotes the reduction of CeO<sub>2</sub> surface based on in-situ Raman and in-situ DRIFT results. They found that the surface hydroxyl species (-OH) of CeO<sub>2</sub> measured from DRIFT spectra began to disappear when Raman signals of Pt-O and Pt-O-Ce in Pt/CeO<sub>2</sub> began to diminish in intensity [50]. This is in agreement with our present result, where H<sub>2</sub> TPR curve (Figure 2-2) and in situ Raman spectra (Figure 2-3) of Pt(2)/CeO<sub>2</sub> 500C show that Pt-O-Ce Raman signals disappeared when the temperature reaches high enough to fully reduce the surface of Pt/CeO<sub>2</sub> (200 °C). The presence of Pt metal on CeO<sub>2</sub> is known to lower the formation energy of surface oxygen vacancy [55, 56]. However, if Pt diffuses into CeO<sub>2</sub>, Pt-O-Ce species would become harder to be reduced since Pt atom of Pt-O-Ce bond would situate in closer proximity to the negatively charged O species, and metallic Pt would become harder to be formed. In such cases, surface reduction of CeO<sub>2</sub> could be initiated when the strengthened Pt-O-Ce bond is reduced to form the Pt(metallic)-CeO<sub>2</sub> junction, leading to the shift of the reduction peak to higher temperature (Figure 2-8).

The same amount of CO was chemisorbed on Pt(2)/CeO<sub>2</sub> 500C and CeO<sub>2</sub> 500C when surface of both samples were fully reduced (Table 2-1). Impregnated Pt on CeO<sub>2</sub> did not increase the number of CO adsorption sites. Therefore, when Pt/CeO<sub>2</sub> was reduced at 200 or 350 °C, where Pt-O-Ce bonds are fully reduced (Figure 2-2), Pt seems to be stabilized in the oxygen vacancies on CeO<sub>2</sub> surface. There have been

several reports that surface oxygen vacancies stabilize precious metal. Farmer et al. reported on their calorimetric measurement that small Ag particles are more stabilized on reduced  $\text{CeO}_2(111)$  surface and that metal support interaction was stronger around the surface oxygen vacancies [57]. The role of surface oxygen on stabilizing impregnated metal seems reasonable, since Vijay and Mills also reported that Au is more stabilized on reduced  $\text{TiO}_2(110)$  surface than on stoichiometric surface [58].

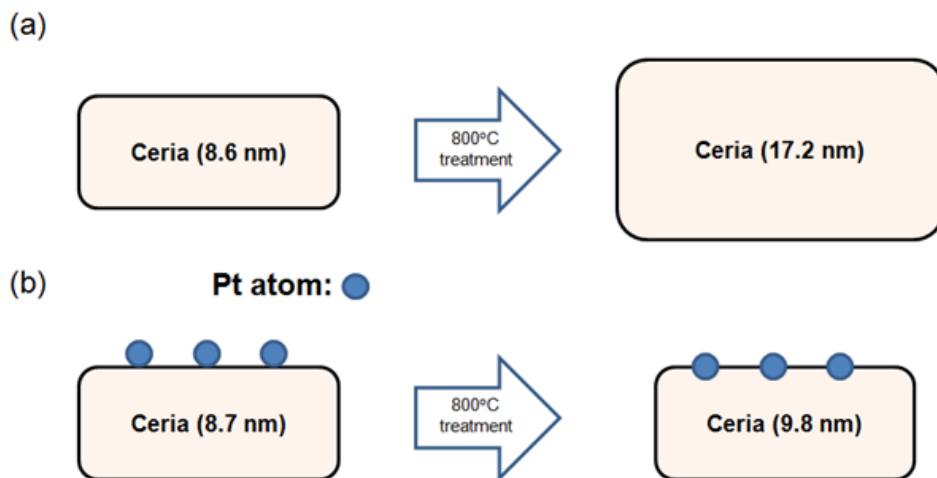


**Figure 2-9.** Schematic diagram comparing the behavior of (a)  $\text{CeO}_2$  and (b)  $\text{Pt}(2)/\text{CeO}_2$  after the oxidation treatment at high temperature. After 800 °C oxidation treatment, crystalline size of  $\text{Pt}(2)/\text{CeO}_2$  was only slightly increased, while that of  $\text{CeO}_2$  was greatly increased from 8.6 nm to 17.2 nm. After the 800 °C oxidation treatment, Pt diffused into  $\text{CeO}_2$  structure, while maintaining the  $\text{CeO}_2$  structure from the oxidative treatment.

# **Chapter 3. Weakening the metal-support interaction to improve catalytic activities of PGM supported catalysts (Pt/CeO<sub>2</sub>&Pt/TiO<sub>2</sub>)**

## **3.1. Introduction**

One of the primary concerns for the application of PGM catalysts lies in how to attain the high metal dispersion on support. In addition to attaining the high metal dispersion, PGM based catalysts should be able to maintain their high metal dispersion during the high temperature treatment, since many catalytic applications are operated at the high temperature. For example, PGM based catalysts are frequently exposed to the hot effluent gas above 800 °C during the regeneration of diesel particulate filter (DPF) [59, 60]. The agglomeration of PGMs at the high temperature could give rise to the loss of active sites, resulting in the deterioration of the catalytic activity. CeO<sub>2</sub> could be used as a support for PGM based catalysts with the high metal dispersion and the enhanced thermal stability [33]. Nagai et al. showed the formation of Pt-O-Ce bond prevents the Pt sintering at the elevated temperature (~800 °C) and maintains the high Pt dispersion in the wide temperature range [31]. Jones et. al. also reported that CeO<sub>2</sub> could trap vaporized PtO<sub>2</sub> because of the strong metal-support interaction, and the Pt sintering could be significantly suppressed when CeO<sub>2</sub> was added as the catalytic component [52].

The presence of  $\text{Pt}^{2+}$  species in Pt-O-Ce bond could be beneficial in some reactions. For example,  $\text{Pt}^{2+}$  is reported to be the active site for WGS reaction [25, 61]. However, despite the significant role of  $\text{Pt}^{2+}$  species in Pt-O-Ce bond in preventing the Pt sintering as well as in promoting the WGS reaction rate, the presence of the strong Pt-O-Ce bond could be unfavorable for the oxidation reactions. Gatla et al. reported that the CO oxidation of Pt/CeO<sub>2</sub> was improved with the formation of the elongated Pt-O-Ce bond, with O more loosely connecting Pt and Ce atoms [62]. Tang et al. also reported that CH<sub>4</sub> oxidation activity was improved by replacing Ce atoms in the surface layer with Pt atoms, which weakened the bond of surrounding oxygen atoms to the oxide surface [63]. Therefore, the CO oxidation ability of Pt/CeO<sub>2</sub> catalysts would be enhanced if the interaction between Pt and CeO<sub>2</sub> could be modulated to the proper strength. Fu et. al. previously reported that when they annealed CeO<sub>2</sub> at the high temperature (800 °C),  $\text{Pt}^{2+}$  species were not formed, which suggests that Pt-CeO<sub>2</sub> interaction could be modulated by thermally treating CeO<sub>2</sub> [61]. The present work aims at investigating the influence of the change in Pt-CeO<sub>2</sub> interaction on the CO oxidation ability and the Pt sintering behavior of Pt/CeO<sub>2</sub> catalysts. The CO oxidation ability of Pt/CeO<sub>2</sub> and Pt/ $\gamma$ -Al<sub>2</sub>O<sub>3</sub> catalysts were comparatively studied because Pt/ $\gamma$ -Al<sub>2</sub>O<sub>3</sub> catalyst is known to have the weak metal-support interaction [50]. The present work proposes that although the strong metal-support interaction is beneficial in achieving the high thermal stability, the catalytic activity could be improved by weakening the metal-support interaction [15].

Similar logic could be applied to Pt supported TiO<sub>2</sub> catalysts [16]. Pt nanoparticles could strongly interact with TiO<sub>2</sub> surface. To weaken the Pt-TiO<sub>2</sub> interaction, S-doped TiO<sub>2</sub> was used as a support where S is expected to interfere with the Pt-TiO<sub>2</sub> interaction. Sulfation of TiO<sub>2</sub> surface has been implemented to suppress phase transformation of TiO<sub>2</sub> from anatase into rutile. Periyat et al. reported that the stability of anatase TiO<sub>2</sub> phase could be improved by incorporating sulfur species into TiO<sub>2</sub>; 100 % anatase was maintained on the sulfated TiO<sub>2</sub> even after the oxidative treatment at 800 °C where phase transformation of TiO<sub>2</sub> usually occurs in the temperature range between 600 and 700 °C [64]. In addition, the decoration of TiO<sub>2</sub> surface with sulfur would dramatically change the electronic band structure of TiO<sub>2</sub> surface, since sulfur species are known to be highly electrophilic. For example, Umabayashi et al. reported that S doping shifted the absorption edge of TiO<sub>2</sub> to the lower energy region [65-67]. Addition of acidic species, such as sulfate, to TiO<sub>2</sub> are also known to play a role as the strong acid sites [68]. For example, it was previously reported that SO<sub>4</sub><sup>2-</sup> species on TiO<sub>2</sub>, which function as the strong acid site, promote Selective Catalytic Reduction (SCR) of NO with NH<sub>3</sub> at high temperature (> 400 °C) [68]. Considering the unique characteristics of sulfate species on TiO<sub>2</sub>, the presence of sulfate on TiO<sub>2</sub> surface would also have an effect on the Pt-TiO<sub>2</sub> interaction. Previously, Hidalgo et. al. reported that the co-presence of sulfate and Pt on TiO<sub>2</sub> surface brought about the synergic effect in photocatalytic phenol oxidation reaction [69]. They suggested that the presence of sulfate on TiO<sub>2</sub> surface suppressed Pt sintering, based on XPS study, which benefited the photochemical phenol oxidation

reaction [69]. However, the influence of sulfated  $\text{TiO}_2$  surface on the metal-support interaction and the catalytic activity is yet to be understood in the complete sense. Therefore, current work addresses the comparative study of Pt- $\text{TiO}_2$  interactions in the presence and absence of surface sulfate [16].

## 3.2. Experimental

**Catalyst Synthesis** Pt was loaded on CeO<sub>2</sub> (Rhodia, 135 m<sup>2</sup>/g) or Alumina (Sasol, 250 m<sup>2</sup>/g) by the incipient wetness impregnation method with aqueous Pt(NH<sub>3</sub>)<sub>4</sub>(NO<sub>3</sub>)<sub>2</sub> (Sigma Aldrich, 99.99 % grade, metal basis) solution as a metal precursor at room temperature. To weaken the metal-support interaction, CeO<sub>2</sub> was annealed at 800 °C in flowing 100 mL/min of 15 % O<sub>2</sub>/N<sub>2</sub> for 2 h prior to the Pt loading. Synthesized catalysts were denoted as Pt(x)/CeO<sub>2</sub> or Pt(x)/ $\gamma$ -Al<sub>2</sub>O<sub>3</sub> or Pt(x)/(800C)CeO<sub>2</sub> where x is the wt% of Pt loaded on the catalyst. After the impregnation procedure, catalysts were dried at 100 °C for 24 h. Afterward, dried catalysts were treated in the flowing 100 mL/min of 15 % O<sub>2</sub>/N<sub>2</sub> at 500 or 800 °C for 2 h. Oxidizing conditions were denoted after the sample name with the capital letter C. For example, Pt(2)/CeO<sub>2</sub> 500C means that Pt(2)/CeO<sub>2</sub> catalyst was oxidized at 500 °C for 2 h.

Figure 3-1 displays Raman spectra of CeO<sub>2</sub> 500C and CeO<sub>2</sub> 800C. Raman bands at 460 and 595 cm<sup>-1</sup> are assigned to the triply degenerate F<sub>2g</sub> mode and the defect induced (D) mode of the fluorite structured CeO<sub>2</sub>, respectively [50]. The relative intensity of 595 to 460 cm<sup>-1</sup> was larger on CeO<sub>2</sub> than that on CeO<sub>2</sub> 800C (Figure 3-1 (a) and (b)), which indicates that the surface defect sites on the CeO<sub>2</sub> surface decreased after the annealing treatment at 800 °C.

Anatase TiO<sub>2</sub> (DT-51 Millenium Chemicals, with the S content of 1.25 atomic % and surface area of 88 m<sup>2</sup> /g) was used as the TiO<sub>2</sub> support containing S. It

is denoted as S-TiO<sub>2</sub>. For the comparative purposes, S-free TiO<sub>2</sub> was synthesized by using conventional sol-gel method [70]. 30 ml titanium tetraisopropoxide (97 %, Aldrich) was dissolved in 90 ml of ethanol (200 proof, Aldrich). The solution was added to 360 ml of distilled water at room temperature while stirring vigorously, resulting in the immediate formation of white suspension. It was continuously stirred for 24 h at 60 °C to complete hydrolysis reaction. The resultant gel-like solution was filtrated and thoroughly washed with distilled water to eliminate impurities, and subsequently dried at 105 °C for 12 h. Obtained powder was further calcinated in the muffle furnace at 400 °C for 4 h. Pt was impregnated on TiO<sub>2</sub> by the excess water impregnation method with aqueous Pt(NH<sub>3</sub>)<sub>4</sub>(NO<sub>3</sub>)<sub>2</sub> (Sigma Aldrich, 99.99 % grade, metal basis) solution as a metal precursor at room temperature. Catalysts are denoted as Pt(x)/TiO<sub>2</sub>, where the number in the parenthesis is the wt.% of Pt loaded. Afterward, catalysts were dried at 100 °C for 24 h and calcined in flowing 100 mL/min of 15 % O<sub>2</sub>/N<sub>2</sub> or 10 % H<sub>2</sub>/N<sub>2</sub> at 500 °C for 2 h. Oxidative and reductive treatments are denoted with the capital letter C and R, respectively. For example, if Pt/TiO<sub>2</sub> was oxidized (or reduced) at 500 °C, then it is denoted as Pt/TiO<sub>2</sub> 500C (or 500R).

**X-ray photoelectron spectroscopy (XPS)** XPS analysis was performed on the AXIS-HSi (Kratos) instrument with 450W of Mg K $\alpha$  radiation. The charging effects were corrected with respect to the C 1s binding energy of 284.5 eV. The spectra were analyzed using casaXPS software. XP contributions from Pt<sup>0</sup>, Pt<sup>2+</sup> and Pt<sup>4+</sup> species were identified. The chemical composition of the catalysts was calculated using the integral intensities of the peaks of each component, subject to the atomic sensitivity

factors reported in the reference [39]. For the case of Pt/ $\gamma$ -Al<sub>2</sub>O<sub>3</sub> catalysts, K-alpha (Thermo U.K.) with Al monochromatic ( $h\nu=1486.6$  eV) source was used to acquire Pt 4d XP spectra since the overlapping of Pt 4f and Al 2p makes it difficult to obtain the information about the oxidation state of Pt on alumina.

**H<sub>2</sub> temperature programmed reduction (TPR)** Cryo-H<sub>2</sub>-temperature programmed reduction (Cryo-H<sub>2</sub>-TPR) was performed using a BEL-CAT-II (BEL Japan Inc.). The samples were pretreated in a flow of 21 % O<sub>2</sub>/N<sub>2</sub> at 400 °C for 2 h prior to the analysis. Afterward, the sample was cooled down to -90 °C, exposed to 5 % H<sub>2</sub>/Ar and stabilized under the flow for 30 min. Temperature was raised from -90 to 900 °C at a rate of 10 °C /min.

**CO chemisorption.** Detailed procedures of CO chemisorption are same as those depicted in Chapter 2.2. 0.2 g of Pt/CeO<sub>2</sub> and 0.12 g of Pt/TiO<sub>2</sub> samples were used for analysis. Before CO adsorption, samples were reduced with H<sub>2</sub> gas for 2 h at the desired temperature to convert the metal oxide into the metallic state. The reduction temperatures of 200, 350 and 500 °C were used and denoted after the sample name in the parenthesis. For example, Pt(2)/CeO<sub>2</sub> 500C (350R) means that Pt(2)/CeO<sub>2</sub> 500C catalyst was in-situ reduced at 350 °C.

**Powder X-ray diffraction (XRD), Surface area measurement and Raman Spectroscopy** Experimental procedures are same as those depicted in Chapter 2.2.

**X-ray Absorption Near Edge Structure (XANES)** XANES spectra around the Pt L3-edge ( $E_0 = 11565$ eV) were obtained in 7D beamline of the Pohang Light Source

(PLS) using Si[111] monochromator. The energy scale was calibrated with respect to the Pt main-edge feature from the standard Pt foil for all the measurements. The intensity of X-ray was measured in a fluorescence mode with He and N<sub>2</sub> gas-filled ionization chambers as detectors. All the measurements were recorded at room temperature in air condition. The background subtraction and normalization, and subsequent linear combination fitting (LCF) were performed by using Athena software package. Pt foil and PtO<sub>2</sub> were used as standard material in LCF analyses with the fitting range of 11545 to 11605 eV. Mean square sum of the misfit at each data point was reduced to minimize the discrepancy between the raw data and the fitted model.

**Extended X-ray Adsorption Fine Structure (EXAFS)** EXAFS data were analyzed using the IFEFFIT (Athena and Artemis) software. Data fitting was performed in the R space on the Fourier-transformed  $k^3$  weighted EXAFS spectra (in the 3-13 Å<sup>-1</sup>k range).

**High-angle annular-dark-field Scanning transmission electron microscopy (HAADF-STEM) and Energy-dispersive spectroscopy (EDS)** HAADF-STEM and EDS analysis were carried out at an accelerating voltage of 200 kV in a JEM-2100F (JEOL) electron microscope, equipped with Field emission gun. By applying low dwell time and averaging over several accumulations, the beam damage of samples was minimized. During scanning, beam tracking was used to avoid the drift. To prepare STEM specimens, catalysts were suspended in ethanol and then ultrasonically dispersed. Drops of the suspension were deposited onto a carbon coated

copper grid and dried overnight in 100 °C oven prior to analysis. To obtain Pt particle size distribution curves, more than 200 Pt particles from several different HAADF-STEM images were counted. Image J was used to measure the Pt particle size. The average particle sizes of Pt on TiO<sub>2</sub> and S-TiO<sub>2</sub> were calculated using the following formula [71];

$$d_p = (\sum nd^3 / \sum nd^{2.19})^{1.23}$$

where  $d_p$ ,  $d$  and  $n$  represent the average particle size, the particle size and the number of Pt particles with  $d$  size, respectively.

**CO oxidation** The CO oxidation ability of Pt/CeO<sub>2</sub> catalysts were measured in a fixed-bed quartz reactor. A 0.05 g of catalyst was mixed with 0.1 g of  $\alpha$ -Al<sub>2</sub>O<sub>3</sub> to dissipate the heat produced during the reaction. Catalysts and  $\alpha$ -Al<sub>2</sub>O<sub>3</sub> were sieved to a size of 150 to 180  $\mu$ m for the reaction tests. The feed gas consisting of 1000 ppm of CO and 10 % of O<sub>2</sub>, balanced by N<sub>2</sub>, was introduced into the reactor using the mass flow controllers. The total flow rate was 200 mL/min, which corresponds to the gas hourly space velocity (GHSV) of 120,000 h<sup>-1</sup>. The reaction temperature was recorded with a K-type thermocouple placed on the top of the catalyst bed. The CO concentration in the outlet gas was measured by using ULTRAMAT 23 gas analyzer (SIEMENS). Temperature was increased from room temperature to 500 °C with the ramping rate of 4 °C/min. Before ramping the temperature, catalysts were exposed to the feed gas at the room temperature for 120 min and the CO break-through curves were obtained. In the case of Pt(2)/(800C)CeO<sub>2</sub> 500C catalyst, catalyst was exposed

to the feed stream for 300 min to reach the CO break-through point. Prior to reaction tests, catalysts were oxidized at 500 °C for 30 min. The reproducibility was confirmed in the repeated reaction tests.

The CO oxidation ability of Pt/CeO<sub>2</sub> was also investigated by using the CO concentration of 1 %. The CO concentration was measured using Fourier Transformed Infrared (FT-IR) Spectrometer (iS-50, Thermo-scientific) with a 3 m gas cell heated to 130 °C. FT-IR was used instead of ULTRAMAT 23 gas analyzer, because the latter could not measure the CO concentrations higher than 1500 ppm. 0.05 g of catalyst was blended with a 0.5 g of  $\alpha$ -Al<sub>2</sub>O<sub>3</sub> to dissipate heat produced during the reaction. After exposing the catalysts to the feed stream (1 % CO, 10 % O<sub>2</sub> and N<sub>2</sub> balance) for 30 min, temperature was raised to 400 °C at the ramping rate of 4 °C/min. The total flow rate was 200 mL/min.

In order to obtain the turnover frequency (TOF) of CO oxidation, the CO conversion data between 5 and 10 % was used. The number of active sites on the CO oxidation was measured by the CO chemisorption analysis. In addition to Pt species, CeO<sub>2</sub> is also known to adsorb CO [46]. Since not only Pt/CeO<sub>2</sub> but also Pt-free CeO<sub>2</sub> was also active in the CO oxidation reaction (See Chapter 3.3.1.), the sum of the amount of CO chemisorbed on Pt and CeO<sub>2</sub> in Pt/CeO<sub>2</sub> was used as the number active sites in the CO oxidation reaction (Table 3-2). The TOF of CO oxidation, defined as the number of CO molecules converted per second on each active site, was calculated by the following equation:

$$\text{TOF (s}^{-1}\text{)} = \frac{\mathbf{v} \times \mathbf{X}}{\mathbf{C}}$$

where  $v$  is the number of CO molecules passing through the catalysts per second,  $X$  is the conversion of CO and  $C$  is the amount of CO chemisorbed on catalysts (Table 2). In addition, the activation energy ( $E_a$ ) of CO oxidation was calculated from the slope of the Arrhenius-type plot of the TOFs.

The CO oxidation ability of Pt/TiO<sub>2</sub> catalysts were measured in a fixed-bed quartz reactor. 0.03 g of catalysts were mixed with 0.1 g of  $\alpha$ -Al<sub>2</sub>O<sub>3</sub> to dissipate the heat produced during the reaction. The feed gas consisting of 1000 ppm of CO and 15 % of O<sub>2</sub>, balanced by N<sub>2</sub>, was introduced into the reactor using mass flow controllers. The total flow rate was 200 mL/min. The CO concentration of the outlet gas was measured by using ULTRAMAT 23 gas analyzer (SIEMENS). Temperature was increased from room temperature to 400 °C with the ramping rate of 4 °C/min after exposing catalysts to the feed gas at room temperature for 60 min.

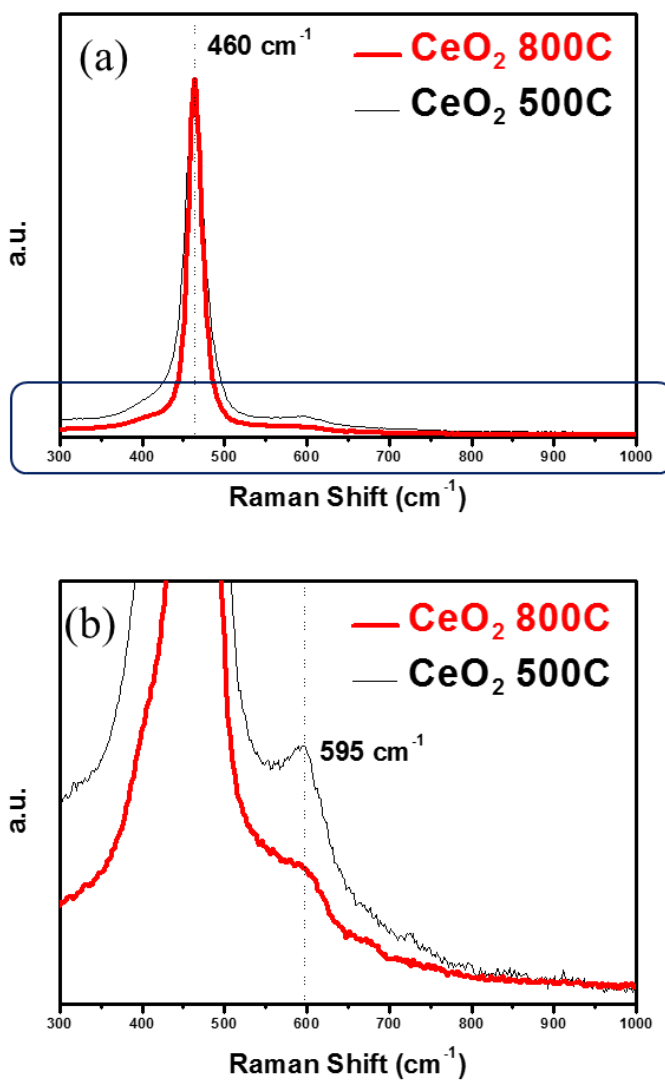


**Figure 3-1.** (a) Raman spectra of CeO<sub>2</sub> 500C and CeO<sub>2</sub> 800C. To observe the rise of Raman peak at 595 cm<sup>-1</sup>, Raman spectra of (a) is magnified 15 times on (b).

### 3.3. Results

**3.3.1. The CO oxidation ability of Pt(2)/CeO<sub>2</sub> and CeO<sub>2</sub>** The CO oxidation ability was compared over CeO<sub>2</sub> and Pt(2)/CeO<sub>2</sub> after the oxidative treatments at 500 and 800 °C. CeO<sub>2</sub> 500C showed the higher CO oxidation rate compared to CeO<sub>2</sub> 800C (Figure 3-2 (a)). For instance, at 190 °C, the TOF of the former catalyst is 0.0010 s<sup>-1</sup> while that of the latter catalyst was only 0.0002 s<sup>-1</sup>. The activation energy of the former catalyst (91 kJ/mol) was also much lower than the latter catalyst (281 kJ/mol) (Table 1). It should be noted that Pt-free CeO<sub>2</sub> surface is also active in the CO oxidation. Therefore, the TOF of the CO oxidation was calculated based on the amount of CO chemisorbed on the catalysts.

The CO oxidation ability of Pt(2)/CeO<sub>2</sub> 500C and 800C was also compared in Figure 3-2 (b). The CO oxidation rate of the former catalyst is superior to that of the latter catalyst (Figure 3-2 (b) and Table 1). It could be observed that the extent of the catalytic deactivation after the oxidative treatment at 800 °C was less severe on Pt(2)/CeO<sub>2</sub> than on CeO<sub>2</sub>. For instance, after the oxidative treatment at 800 °C, the TOF at 190 °C decreased from 0.0010 to 0.0002 s<sup>-1</sup> over CeO<sub>2</sub> while it decreased from 0.0018 to 0.0017 s<sup>-1</sup> over Pt/CeO<sub>2</sub>. The addition of Pt to CeO<sub>2</sub> also promoted the CO oxidation ability, especially in the high CO conversion region. Pt(2)/CeO<sub>2</sub> catalysts reached 100 % CO conversion at the temperature below 350 °C, while CeO<sub>2</sub> catalysts required 500 °C to reach 100 % CO conversion (Figure 3-2). In summary, the addition of Pt to CeO<sub>2</sub> improved the CO oxidation performance of catalysts.

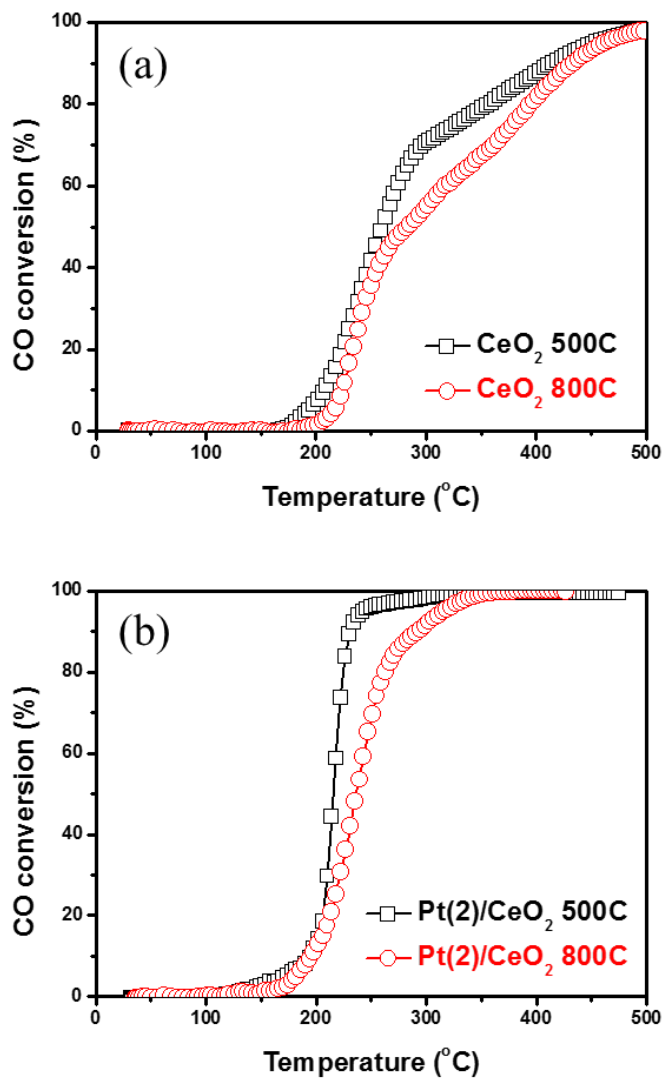


**Figure 3-2.** Light-off curves of CO oxidation over (a) CeO<sub>2</sub> and (b) Pt(2)/CeO<sub>2</sub> catalysts, after oxidative treatments at 500 and 800 °C.

### **3.3.2. The influence of the change in Pt-CeO<sub>2</sub> interaction induced by the thermal treatment of CeO<sub>2</sub> prior to the Pt loading**

**3.3.2.1. The influence on the Pt sintering behavior** Figure 3-3 shows XRD patterns of Pt(2)/(800C)CeO<sub>2</sub> and Pt(2)/ $\gamma$ -Al<sub>2</sub>O<sub>3</sub> catalysts after oxidative treatments at 500 and 800 °C. After the oxidative treatment at 800 °C, appreciable XRD patterns from the Pt metal were clearly observed on Pt(2)/ $\gamma$ -Al<sub>2</sub>O<sub>3</sub> catalyst at 39.8, 46.2, 67.4, 81.3 and 85.7 ° which correspond to (111), (200), (220), (311) and (222) facets of metallic Pt, respectively. However, XRD pattern from Pt clusters was hardly observed on Pt(2)/(800C)CeO<sub>2</sub> catalysts, indicating that Pt is relatively well dispersed on (800C)CeO<sub>2</sub> even after the oxidative treatment at 800 °C.

When the region between 38 and 42 ° is enlarged (Figure 3-3 (b)), the small XRD peak from Pt metal was clearly observed on Pt(2)/(800C)CeO<sub>2</sub> 800C, while it was not detected on Pt(2)/CeO<sub>2</sub> 800C. This indicates that Pt-CeO<sub>2</sub> interaction is stronger on Pt(2)/CeO<sub>2</sub> catalysts than on Pt(2)/(800C)CeO<sub>2</sub> catalysts. Thermally treating CeO<sub>2</sub> at 800 °C prior to the Pt loading weakened the metal-support interaction, which resulted in some extent of the Pt aggregation on (800C)CeO<sub>2</sub> when the catalyst was exposed to the elevated temperature of 800 °C.

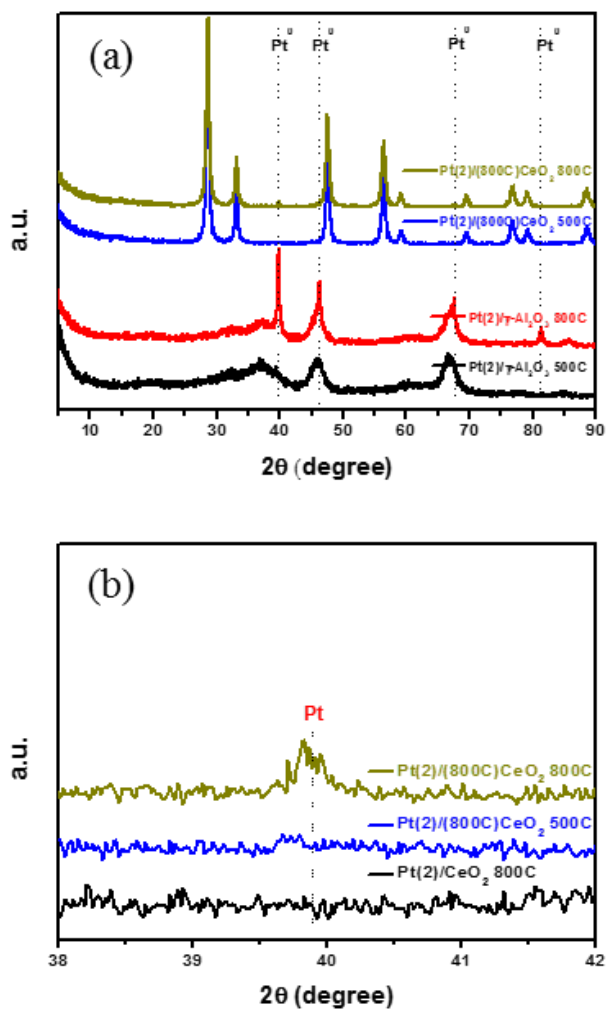


**Figure 3-3.** (a) XRD pattern of Pt(2)/(800C)CeO<sub>2</sub> and Pt(2)/ $\gamma$ -Al<sub>2</sub>O<sub>3</sub> catalysts after the oxidative treatments at 500 and 800 °C. (b) XRD pattern of Pt(2)/(800C)CeO<sub>2</sub> 500C, 800C and Pt(2)/CeO<sub>2</sub> 800C catalysts.

**3.3.2.2. The influence on the CO oxidation ability** Figure 3-4 and 3-5 show the reaction rate of the CO oxidation over Pt(2)/CeO<sub>2</sub> and Pt(2)/ $\gamma$ -Al<sub>2</sub>O<sub>3</sub> after the oxidative treatments at 500 and 800 °C. As displayed in Figure 3-4, the CO oxidation ability of Pt(2)/ $\gamma$ -Al<sub>2</sub>O<sub>3</sub> catalysts was not affected substantially depending on the calcination temperatures (e.g., 500 and 800 °C), which were superior to that of Pt(2)/CeO<sub>2</sub> catalysts. For instance, when the reaction rates are compared at 190 °C, the TOF of Pt(2)/ $\gamma$ -Al<sub>2</sub>O<sub>3</sub> 500C was 0.0462 s<sup>-1</sup> while that of Pt(2)/CeO<sub>2</sub> 500C was 0.0018 s<sup>-1</sup> (Figure 3-5 and Table 3-1). This implies that although the strong Pt-O-Ce bonds improved the thermal stability of catalysts as discussed in Chapter 2, the presence of most of Pt species in the form of Pt-O-Ce bonds resulted in the low CO oxidation ability. Cationic Pt<sup>2+</sup> species are known to be less active in CO oxidation than Pt<sup>0</sup> species [18, 52]. Ding et al. reported that CO adsorbed on cationic Pt is not reactive at low temperature, while that adsorbed on metallic Pt reacts readily with O<sub>2</sub> [18]. Jones et al. also reported that CO adsorbed on metallic Pt species is more reactive with O<sub>2</sub> than that adsorbed on ionic Pt species [52]. The strong interaction between Pt and CeO<sub>2</sub> seems to inhibit the CO oxidation ability. On the contrary, Pt species interact with alumina rather weakly than with CeO<sub>2</sub>, which will be addressed later in more detail. It can be concluded that the weak interactions between Pt and alumina benefited the CO oxidation ability.

Figure 3-4 (b) and 3-5 (b) compare the reaction rates of the CO oxidation over Pt(2)/(800C)CeO<sub>2</sub> and Pt(2)/ $\gamma$ -Al<sub>2</sub>O<sub>3</sub> catalysts after the oxidative treatments at 500 and 800 °C. Figure 3-5 (b) demonstrates that the CO oxidation performance of

Pt(2)/(800C)CeO<sub>2</sub> 500C and 800C catalysts is superior to that of Pt(2)/ $\gamma$ -Al<sub>2</sub>O<sub>3</sub> 500C. Especially, the activation energies of Pt(2)/(800C)CeO<sub>2</sub> 500C and 800C catalysts (33 and 56 kJ/mol, respectively) are estimated to be much lower than that of Pt(2)/ $\gamma$ -Al<sub>2</sub>O<sub>3</sub> 500C catalyst (177 kJ/mol) (Table 3-1). In other words, the thermal treatment of CeO<sub>2</sub> prior to the Pt loading enhanced the CO oxidation reaction rate. Interestingly, Pt(2)/(800C)CeO<sub>2</sub> 500C showed the much higher reaction rate in CO oxidation compared to Pt(2)/ $\gamma$ -Al<sub>2</sub>O<sub>3</sub> as well as Pt(2)/CeO<sub>2</sub>. Comparing Pt(2)/(800C)CeO<sub>2</sub> 500C with Pt(2)/ $\gamma$ -Al<sub>2</sub>O<sub>3</sub> 500C and Pt(2)/CeO<sub>2</sub> 500C, T<sub>50</sub> of the former was located at the lower temperature by 44 and 76 °C, respectively (Table 3-1). The activation energy of Pt(2)/(800C)CeO<sub>2</sub> 500C (33 kJ/mol) is comparable to some of the lowest values reported in the literature for the CO oxidation of Pt catalysts [52, 72]. In summary, the CO oxidation activity shows the following trend: (1) 500C sample, Pt(2)/(800C)CeO<sub>2</sub> > Pt(2)/ $\gamma$ -Al<sub>2</sub>O<sub>3</sub> > Pt(2)/CeO<sub>2</sub> and (2) 800C sample, Pt(2)/ $\gamma$ -Al<sub>2</sub>O<sub>3</sub> ~ Pt(2)/(800C)CeO<sub>2</sub> > Pt(2)/CeO<sub>2</sub>. It has already been discussed that Pt-CeO<sub>2</sub> interaction could be attenuated by loading Pt on pre-calcined CeO<sub>2</sub>. Therefore, the weakened Pt-CeO<sub>2</sub> interaction would be beneficial for CO oxidation.

CO break-through curves with time-on-stream during the CO oxidation (1000 ppm CO and 10 % O<sub>2</sub>) at room temperature over Pt(2)/CeO<sub>2</sub> 500C, Pt(2)/(800C)CeO<sub>2</sub> 500C and 800C catalysts are shown in Figure 3-6. The CO break-through curve with the empty cell is also displayed in Figure 3-6 as a reference. The CO break-through is reached to the inlet level on Pt(2)/CeO<sub>2</sub> 500C as soon as CO is introduced to the catalyst. However, longer than 240 min was required for

Pt(2)/(800C)CeO<sub>2</sub> 500C catalyst to reach the CO break-through point. ~195 μmol of CO was consumed on Pt(2)/(800C)CeO<sub>2</sub> 500C during 240 min of CO exposure (1000 ppm) at the room temperature, which is about 38 times larger than the amount of Pt loaded (5.1 μmol) on (800C)CeO<sub>2</sub>. The CO adsorption on CeO<sub>2</sub> could be excluded since the steady-state CO value was reached on CeO<sub>2</sub> 500C as soon as CO was introduced (data not shown). This result supports that Pt species loaded on annealed CeO<sub>2</sub> support possess the notable CO oxidation ability even at room temperature, which is gradually degraded with time-on-stream due to the Pt poisoning by CO. Mars-van Krevelen type mechanism seems to be activated on Pt(2)/(800C)CeO<sub>2</sub> 500C at the room temperature, where CO adsorbed on Pt reacts with O from CeO<sub>2</sub>. Figure 3-6 (b) shows that the low temperature CO oxidation ability can be also affected by the final calcination temperature (e.g., 500C and 800C) in addition to the annealing temperature of CeO<sub>2</sub>. CO break-through was reached to the inlet level on Pt(2)/(800C)CeO<sub>2</sub> 800C as soon as CO was introduced to the catalyst, contrary to the case on Pt(2)/(800C)CeO<sub>2</sub> 500C. This confirms that the low-temperature activity of Pt(2)/(800C)CeO<sub>2</sub> was completely lost after the oxidative treatment at 800 °C. In other words, Mars-van Krevelen type mechanism does not work on Pt(2)/(800C)CeO<sub>2</sub> 800C at room temperature.

### 3.2.2.3. The relationships between the Pt dispersion and the CO oxidation ability

Comparing Pt(2)/(800C)CeO<sub>2</sub> 800C with Pt(2)/ $\gamma$ -Al<sub>2</sub>O<sub>3</sub> 800C, it is observed that the Pt dispersion is much higher on the former (47 %) than on the latter (1 %) based on combined XRD (Figure 3-3) and CO chemisorption results (Table 3-2). Interestingly, in Figure 3-4, the CO oxidation performance of Pt(2)/ $\gamma$ -Al<sub>2</sub>O<sub>3</sub> was comparable to that of Pt(2)/(800C)CeO<sub>2</sub> 800C in spite of the much lower Pt dispersion of Pt(2)/ $\gamma$ -Al<sub>2</sub>O<sub>3</sub> 800C. T<sub>50</sub> of Pt(2)/ $\gamma$ -Al<sub>2</sub>O<sub>3</sub> 800C was observed at 172 °C, while that of Pt(2)/(800C)CeO<sub>2</sub> 800C was observed at 188 °C (Table 3-1). According to the literature, the CO oxidation is structure sensitive on Pt based catalysts [73]. The CO oxidation reaction rate is known to be higher on the terrace sites of single-crystal catalysts than on the defect sites [74, 75]. Atalik and Uner observed that the activation energy of the CO oxidation over Pt/ $\gamma$ -Al<sub>2</sub>O<sub>3</sub> decreased as the Pt particle size increased [76]. In line with the previous reports, the activation energy of the CO oxidation on Pt(2)/ $\gamma$ -Al<sub>2</sub>O<sub>3</sub> decreased from 177 to 102 kJ/mol when the oxidation temperature increased from 500 to 800 °C (Table 3-1). This huge reduction in the activation energy will counteract the effect of the low Pt dispersion in the reaction. Pt(2)/ $\gamma$ -Al<sub>2</sub>O<sub>3</sub> 800C catalyst has the largest Pt particle size among the catalysts investigated in this work. The formation of terrace sites on large Pt particle of Pt(2)/ $\gamma$ -Al<sub>2</sub>O<sub>3</sub> 800C would give rise to the excellent CO oxidation ability. The Pt particle size on the other tested catalysts is smaller than 5 nm, the detection limit of the XRD, and therefore the structure sensitivity would not explain their activity differences.

When the CO concentration in the feed is 1000 ppm, however, it is expected that the influence of the different Pt dispersion of Pt(2)/(800C)CeO<sub>2</sub> 800C and Pt(2)/ $\gamma$ -Al<sub>2</sub>O<sub>3</sub> 800C on the CO oxidation ability would not be significant because the reaction rate would be determined mainly by the small fraction of Pt terrace sites, which are more reactive. To validate the effect of the Pt dispersion on the CO oxidation ability, the CO concentration in the feed was increased to 1 %. When the CO concentration is high in the feed, the CO oxidation rate on Pt sites with the low activation energy would be saturated. It provides CO molecules more chances to collide with the Pt sites having the high activation energy with the higher frequency. In such circumstances, the Pt dispersion would have the larger influence on the CO oxidation rate. In Figure 3-7, Pt(2)/(800C)CeO<sub>2</sub> 800C showed the better CO oxidation ability than Pt(2)/ $\gamma$ -Al<sub>2</sub>O<sub>3</sub> 800C as opposed to the CO oxidation results with 1000 ppm of CO in the feed in Figure 3-4. The activation energy of the CO oxidation was calculated by plotting the reaction rates in the CO conversion region from 5 to 15 % as a function of temperature as shown in Figure 3-7 (b). The activation energy was lower on Pt(2)/ $\gamma$ -Al<sub>2</sub>O<sub>3</sub> 800C (85 kJ/mol) than on Pt(2)/(800C)CeO<sub>2</sub> 800C (93 kJ/mol), even though Pt(2)/(800C)CeO<sub>2</sub> 800C displayed better catalytic performance. Such fact indicates that the high Pt dispersion on Pt(2)/(800C)CeO<sub>2</sub> 800C compensated its high activation energy. The active sites with the low activation energy would mainly facilitate the reaction at the low CO concentration (1000 ppm), while the active sites with the high activation energy would be involved more dominantly in the CO oxidation at the high CO concentration (1%).

| Sample  |      | Activation Energy<br>( $E_a$ ) (kJ/mol) | TOF (@ 190 °C)<br>(1/s) | T <sub>50</sub><br>(°C) | T <sub>90</sub><br>(°C) |
|---|------|---|-------------------------|-------------------------|-------------------------|
| CeO <sub>2</sub>                                | 500C | 91                                      | 0.0010                  | 260                     | 412                     |
|   | 800C | 281                                     | 0.0002                  | 285                     | 435                     |
| Pt(2)/CeO <sub>2</sub>                          | 500C | 55                                      | 0.0018                  | 216                     | 231                     |
|   | 800C | 79                                      | 0.0017                  | 237                     | 295                     |
| Pt(2)/(800C)CeO <sub>2</sub>                    | 500C | 33                                      | 0.0511 <sup>a</sup>     | 140                     | 149                     |
|   | 800C | 56                                      | 0.0450 <sup>a</sup>     | 188                     | 196                     |
| Pt(2)/ $\gamma$ -Al <sub>2</sub> O <sub>3</sub> | 500C | 177                                     | 0.0462 <sup>a</sup>     | 184                     | 192                     |
|   | 800C | 102                                     | 2.9286 <sup>a</sup>     | 172                     | 180                     |
| Pt(100) from<br>Berlowitz et al. (38)           |      | 54                                      |                         |                         |                         |

<sup>a</sup>. The CO conversion has already reached over 70 % at 190 °C.

**Table 3-1.** Activation energy, TOF (at 190 °C), T<sub>50</sub> and T<sub>90</sub> of CO oxidation over CeO<sub>2</sub>, Pt(2)/CeO<sub>2</sub>, Pt(2)/(800C)CeO<sub>2</sub> and Pt(2)/ $\gamma$ -Al<sub>2</sub>O<sub>3</sub> catalysts after oxidative treatment at 500 and 800 °C.

| Sample  |      | The amount of chemisorbed CO (mmol/g) <sup>a</sup> | Pt dispersion (%) | The ratio between the amount of Pt loaded and the amount of chemisorbed CO |
|---|------|--|-------------------|--|
| CeO <sub>2</sub>                                | 500C | 0.133 <sup>b</sup>                                 | 119 <sup>d</sup>  | -  |
|   | 800C | 0.034 <sup>b</sup>                                 | 33 <sup>d</sup>   | -  |
| Pt(2)/CeO <sub>2</sub>                          | 500C | 0.135 <sup>c</sup>                                 | 120               | 0.76   |
|   | 800C | 0.135 <sup>c</sup>                                 | 120               | 0.76   |
| Pt(2)/(800C)CeO <sub>2</sub>                    | 500C | 0.058 <sup>c</sup>                                 | 57                | 1.78   |
|   | 800C | 0.048 <sup>c</sup>                                 | 47                | 2.15   |
| Pt(2)/ $\gamma$ -Al <sub>2</sub> O <sub>3</sub> | 500C | 0.054 <sup>c</sup>                                 | 53                | 1.91   |
|   | 800C | 0.001 <sup>c</sup>                                 | 1                 | 103  |

<sup>a</sup>. Measured by extrapolating the CO pressure to 0 kPa on CO chemisorption curves. <sup>b</sup>. Sample was reduced *in-situ* at 500 °C before adsorbing CO. <sup>c</sup>. Sample was reduced *in-situ* at 350 °C before adsorbing CO. <sup>d</sup>. Pt dispersion was calculated assuming that 2 wt% of Pt is supported on CeO<sub>2</sub>.

**Table 3-2.** The amount of chemisorbed CO, the Pt dispersion, and the ratio between the amount of Pt loaded and the amount of chemisorbed CO of CeO<sub>2</sub>, Pt(2)/CeO<sub>2</sub>, Pt(2)/(800C)CeO<sub>2</sub> and Pt(2)/ $\gamma$ -Al<sub>2</sub>O<sub>3</sub> after the oxidative treatment at 500 and 800 °C.

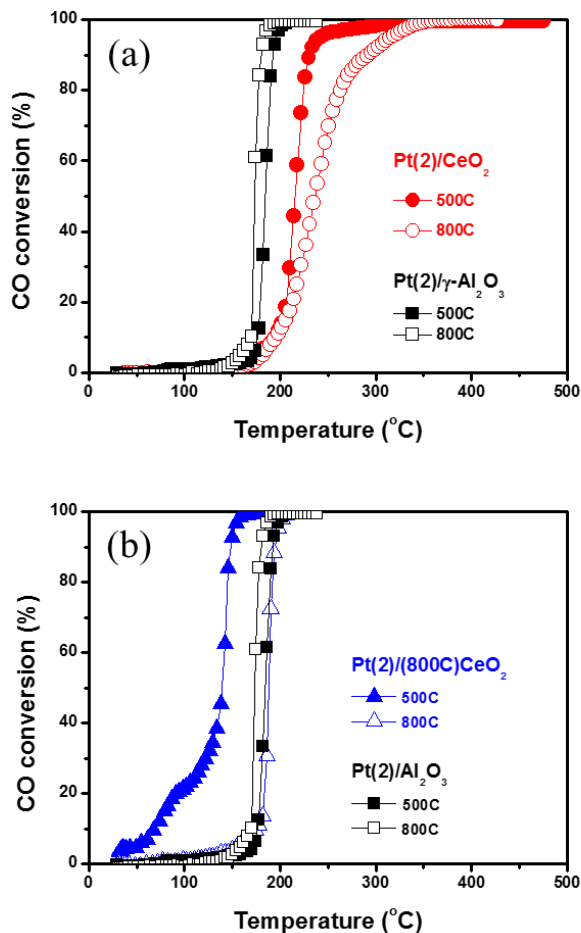


**Figure 3-4.** (a) Light-off curves of CO oxidation over Pt(2)/CeO<sub>2</sub> and Pt(2)/γ-Al<sub>2</sub>O<sub>3</sub> catalysts, after oxidative treatments at 500 and 800 °C. (b) Light-off curves of CO oxidation over Pt(2)/(800C)CeO<sub>2</sub> and Pt(2)/γ-Al<sub>2</sub>O<sub>3</sub> catalysts, after oxidative treatment at 500 and 800 °C. Pt(2)/(800C)CeO<sub>2</sub> 500C was exposed to 1000 ppm of CO for 5 h at room temperature to reach the steady state CO concentration before reaction.

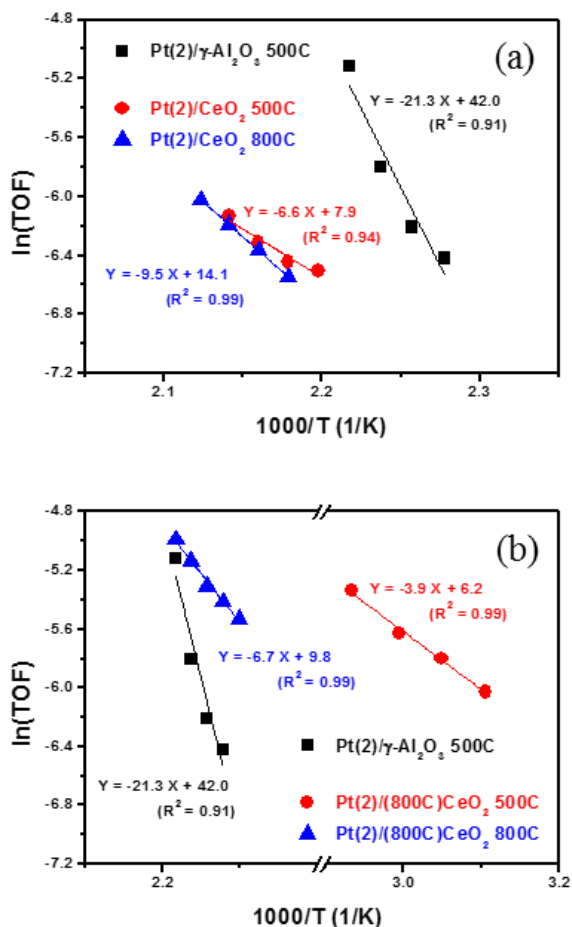


**Figure 3-5.** (a) The temperature dependence of TOF of Pt(2)/CeO<sub>2</sub> 500C and 800C catalysts. (b) The temperature dependence of TOF of Pt(2)/(800C)CeO<sub>2</sub> 500C and 800C catalysts. For a comparison, TOFs of Pt(2)/ $\gamma$ -Al<sub>2</sub>O<sub>3</sub> 500C are provided in the figure.

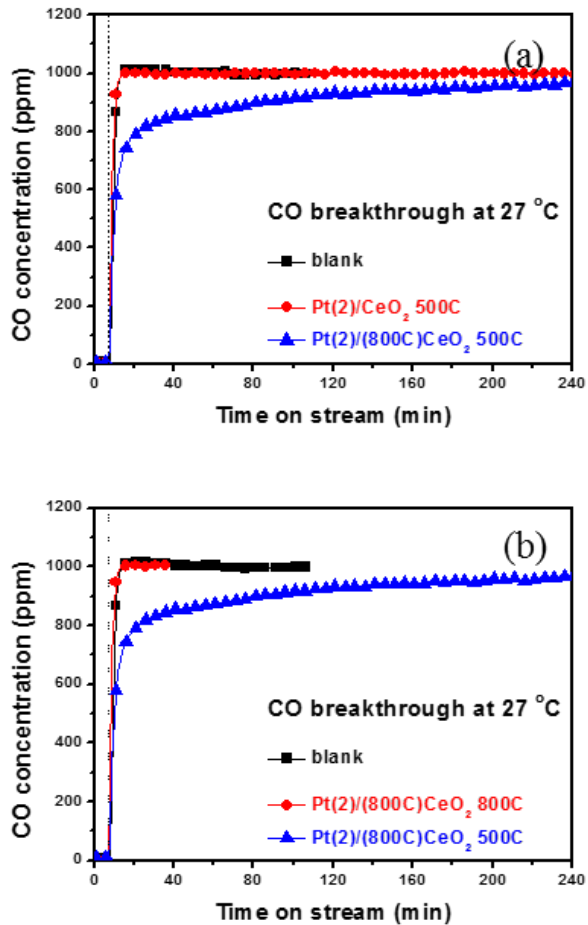


**Figure 3-6.** (a) CO break-through curves with time-on-stream during the CO oxidation (1000 ppm CO and 10 % O<sub>2</sub>) at the room temperature over Pt(2)/CeO<sub>2</sub> 500C and Pt(2)/(800C)CeO<sub>2</sub> 500C catalysts. (b) CO break-through curves with time-on-stream during the CO oxidation at the room temperature over Pt(2)/(800C)CeO<sub>2</sub> 500C and 800C catalysts.

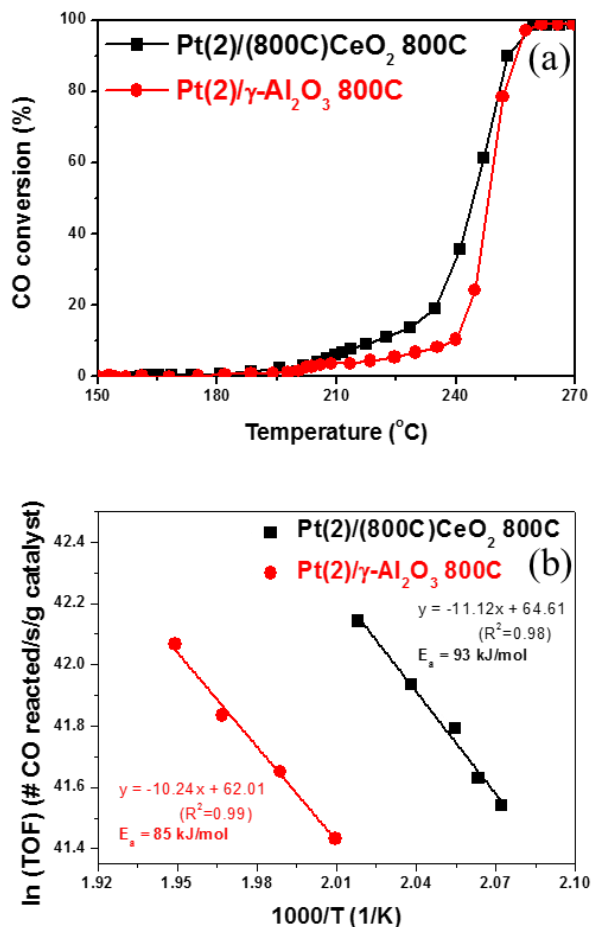


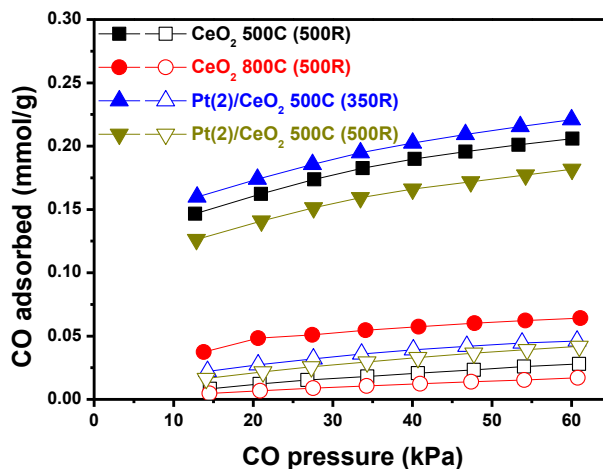
**Figure 3-7.** (a) Light-off curves of the CO oxidation over Pt(2)/(800C)CeO<sub>2</sub> 800C and Pt(2)/γ-Al<sub>2</sub>O<sub>3</sub> 800C catalysts with 1 % of CO in the feed. (b) The activation energy (E<sub>a</sub>) was calculated from the slope of the Arrhenius-type plot of the TOFs.

### **3.3.3 Chemical states of the Pt species on CeO<sub>2</sub>, (800C)CeO<sub>2</sub> and $\gamma$ -Al<sub>2</sub>O<sub>3</sub> supports**

#### **3.3.3.1 Investigation of the chemical states of Pt species by CO chemisorption**

Figure 3-8 shows the CO chemisorption curves of CeO<sub>2</sub> 500C, 800C and Pt(2)/CeO<sub>2</sub> 500C catalysts. In Chapter 2, it was found that the amount of oxygen vacancy on CeO<sub>2</sub> surface is strongly related to the amount of CO chemisorbed on CeO<sub>2</sub>. To maximize the amount of chemisorbed CO on CeO<sub>2</sub>, the in-situ reduction temperature for the CO chemisorption was set at 500 °C. 0.133 and 0.034 mmol/g of CO were chemisorbed on CeO<sub>2</sub> 500C and 800C, respectively. On the other hand, when 2 wt% of Pt is impregnated on CeO<sub>2</sub>, Pt facilitates the reduction of CeO<sub>2</sub>, and the CeO<sub>2</sub> surface is fully reduced already below 200 °C [14]. The amount of CO chemisorbed on Pt(2)/CeO<sub>2</sub> 500C reaches the maximum value of 0.135 mmol/g at the reduction temperature of 350 °C and decreases to 0.107 mmol/g at the reduction temperature of 500 °C, which correspond to the Pt dispersion of 121 and 105 %, respectively (Table 3-2). Since the amount of CO chemisorbed on CeO<sub>2</sub> 500C and Pt(2)/CeO<sub>2</sub> 500C is similar, Pt species would be located at oxygen vacancies on the CeO<sub>2</sub> surface [14]. The CO chemisorption overestimates the Pt dispersion; the amount of CO chemisorbed on Pt(2)/CeO<sub>2</sub> (0.135 mmol/g) was larger than the amount of Pt loaded on CeO<sub>2</sub> (0.103 mmol/g). This is because the amount of reducible surface oxygen on CeO<sub>2</sub>, which transforms into oxygen vacancy after the reductive treatment, is larger than the amount of Pt loaded. This would drive most of Pt species to form Pt-O-Ce bonds, as discussed in Chapter 2.

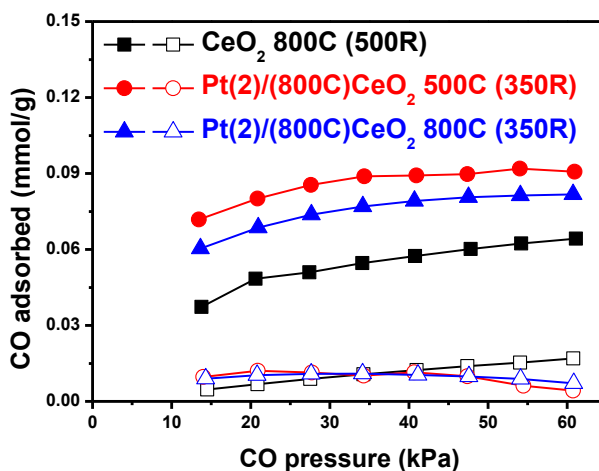
Figure 3-9 shows the CO chemisorption curves of Pt(2)/(800C)CeO<sub>2</sub> 500C, 800C and CeO<sub>2</sub> 800C, which demonstrate that the amount of Pt loaded on (800C)CeO<sub>2</sub> (0.103 mmol/g) is larger than the amount of CO chemisorbed on (800C)CeO<sub>2</sub> (0.034 mmol/g) (Table 3-2). When 2 wt% of Pt was loaded on (800C)CeO<sub>2</sub>, the amount of CO chemisorbed increased to 0.058 and 0.048 mmol/g on Pt(2)/(800C)CeO<sub>2</sub> 500C and 800C, respectively. After the reductive pretreatment at 350 °C, where Pt(2)/(800C)CeO<sub>2</sub> surface is reduced (Figure 3-11), the surface oxygen vacancies on CeO<sub>2</sub> would be fully occupied by Pt species, and some of Pt species may also reside on CeO<sub>2</sub> surface other than the oxygen vacancies leading to the increased amount of chemisorbed CO. The Pt dispersion of Pt(2)/(800C)CeO<sub>2</sub> 500C and 800C catalysts is estimated as 57 and 47 % from the CO chemisorption, respectively, which are the upper limit of the actual Pt dispersion. Such high Pt dispersions are supported by XRD results in Figure 3-3, where XRD pattern from Pt was hardly observed on both catalysts. Figure 3-8 and 3-9 indicate that the ratio of the amount of Pt loaded to the amount of CO chemisorbed on bare CeO<sub>2</sub> support (without Pt) could be the important parameter in determining the strength of the Pt-CeO<sub>2</sub> interaction (Table 2). When the amount of Pt loaded exceeds the amount of CO chemisorbed on bare CeO<sub>2</sub>, some Pt atoms may not form Pt-O-Ce bond and small Pt agglomerates would be formed. Consequently, minor Pt sintering was observed on Pt(2)/(800C)CeO<sub>2</sub> after the oxidative treatment at 800 °C. However, the presence of Pt species without forming Pt-O-Ce bonds greatly improved the CO oxidation ability of Pt(2)/(800C)CeO<sub>2</sub> compared with Pt/CeO<sub>2</sub> catalysts (Figure 3-4 and 3-5).



| Amount of  | (mmol/g) |
|--|----------|
| CO chemisorbed on<br>CeO <sub>2</sub> 500C (500R) <sup>1</sup>       | 0.133    |
| CO chemisorbed on<br>Pt(2)/CeO <sub>2</sub> 500C (350R) <sup>1</sup> | 0.135    |
| CO chemisorbed on<br>Pt(2)/CeO <sub>2</sub> 500C (500R) <sup>1</sup> | 0.107    |
| Pt loaded on Pt(2)/CeO <sub>2</sub>                                  | 0.103    |

<sup>1</sup> Quantity measured after extrapolating to 0 kPa CO pressure

**Figure 3-8.** CO chemisorption curves of CeO<sub>2</sub> and Pt(2)/CeO<sub>2</sub> catalysts, after the oxidative treatments at 500 and 800 °C. In-situ reduction temperature is marked in the parenthesis. Filled symbol represents the sum of the amount of chemisorbed and physisorbed CO while the empty symbol represents the amount of physisorbed CO. On the table listed is the amount of chemisorbed CO and the amount of Pt impregnated on CeO<sub>2</sub>.



| Amount of  | (mmol/g) |
|--|----------|
| CO chemisorbed on<br>CeO <sub>2</sub> 800C (500R) <sup>1</sup>             | 0.034    |
| CO chemisorbed on<br>Pt(2)/(800C)CeO <sub>2</sub> 500C (350R) <sup>1</sup> | 0.058    |
| CO chemisorbed on<br>Pt(2)/(800C)CeO <sub>2</sub> 800C (350R) <sup>1</sup> | 0.048    |
| Pt loaded on Pt(2)/(800C)CeO <sub>2</sub>                                  | 0.103    |

<sup>1</sup> Quantity measured after extrapolating to 0 kPa CO pressure

**Figure 3-9.** CO chemisorption curves of Pt(2)/(800C)CeO<sub>2</sub> 500C, 800C and CeO<sub>2</sub> 800C catalysts. The in-situ reduction temperature is marked in the parenthesis. Filled symbol represents the sum of the amount of chemisorbed and physisorbed CO while the empty symbol represents the amount of physisorbed CO. On the table listed is the amount of chemisorbed CO and the amount of Pt impregnated on (800C)CeO<sub>2</sub>.

### 3.3.3.2. Investigation of the chemical states of Pt species by XP spectroscopy

Figure 3-10 shows XP spectra of Pt(2)/CeO<sub>2</sub> and Pt(2)/(800C)CeO<sub>2</sub> catalysts in Pt 4f region after 500C and 800C treatments. The XP contributions from Pt<sup>0</sup>, Pt<sup>2+</sup> and Pt<sup>4+</sup> species are de-convoluted and marked in Figure 3-10. Pt<sup>2+</sup> is the dominant state over Pt(2)/CeO<sub>2</sub> 500C and 800C catalysts.

On the other hand, in the case of Pt(2)/(800C)CeO<sub>2</sub> 500C and 800C catalysts, the appreciable contributions from Pt<sup>4+</sup> species were observed in Figure 3-10 (c) and (d). Pt<sup>2+</sup>/Pt<sup>4+</sup> ratio of Pt(2)/(800C)CeO<sub>2</sub> 500C and 800C were 1.79 and 0.69, respectively, which is lower than the values of Pt(2)/CeO<sub>2</sub> 500C (15.00) and 800C (5.91) indicating the presence of the larger proportion of Pt<sup>4+</sup> (Table 3-3). XP peak from Pt<sup>0</sup> was also observed in XP spectra of Pt(2)/(800C)CeO<sub>2</sub> 800C in Figure 3-10 (d) in agreement with XRD results in Figure 3-3 where Pt(2)/(800C)CeO<sub>2</sub> 800C displayed the XRD pattern from the Pt metal. When the oxidation temperature was raised from 500 to 800 °C, the relative surface concentration of Pt/Ce ratio on Pt(2)/(800C)CeO<sub>2</sub> decreased from 0.083 to 0.064, the majority of which originates from the loss of the detectable Pt<sup>2+</sup> species, since Pt<sup>2+</sup>/Pt<sup>4+</sup> ratio decreased from 1.79 to 0.69 (Table 3-3). Such decrease in Pt/Ce ratio on Pt(2)/(800C)CeO<sub>2</sub> after the oxidative treatment at 800 °C should be ascribed to the diffusion of Pt species into CeO<sub>2</sub> and the Pt sintering [14]. The presence of Pt<sup>4+</sup> species on (800C)CeO<sub>2</sub> would lead to the superior CO oxidation ability of Pt(2)/(800C)CeO<sub>2</sub> catalysts to Pt(2)/CeO<sub>2</sub> catalysts (Figure 3-4 and 3-5). PtO<sub>2</sub> species are volatile [52], and PtO<sub>2</sub>-like species on (800C)CeO<sub>2</sub> would be more reactive toward the CO oxidation than Pt-O-Ce

species. In addition, both XRD patterns (Figure 3-3) and XP spectra (Figure 3-10) indicate the formation of metallic Pt agglomerates on Pt(2)/(800C)CeO<sub>2</sub> 800C. Pt agglomeration into metallic Pt cluster seems to be detrimental to the CO oxidation ability since Pt(2)/(800C)CeO<sub>2</sub> 800C did not show the CO oxidation activity at room temperature unlike Pt(2)/(800C)CeO<sub>2</sub> 500C where metallic Pt was not present.

| Atomic ratio                       | Pt(2)/CeO <sub>2</sub> |       | Pt(2)/(800C)CeO <sub>2</sub> |       |
|------------------------------------|------------------------|-------|------------------------------|-------|
|                                    | 500C                   | 800C  | 500C                         | 800C  |
| Pt/Ce                              | 0.095                  | 0.063 | 0.083                        | 0.064 |
| Pt <sup>2+</sup> /Pt <sup>4+</sup> | 15.0                   | 5.91  | 1.79                         | 0.69  |

**Table 3-3.** The relative atomic concentration of Pt to Ce and Pt<sup>2+</sup> to Pt<sup>4+</sup> of Pt(2)/CeO<sub>2</sub> and Pt(2)/(800C)CeO<sub>2</sub> catalysts obtained from X-ray Photoelectron Spectroscopy.

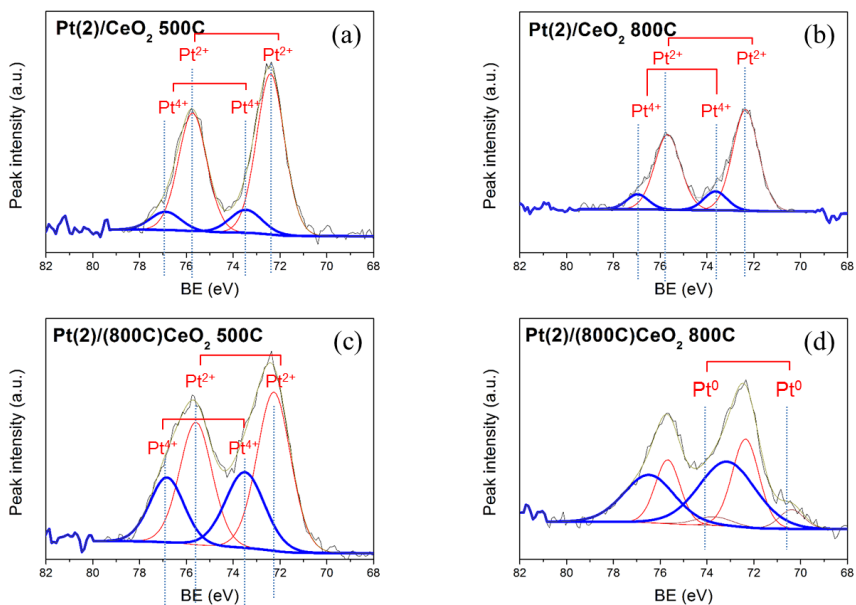


**Figure 3-10.** XPS spectra of (a) Pt(2)/CeO<sub>2</sub> 500C, (b) Pt(2)/CeO<sub>2</sub> 800C, (c) Pt(2)/(800C)CeO<sub>2</sub> 500C and (d) Pt(2)/(800C)CeO<sub>2</sub> 800C. The contributions from Pt<sup>2+</sup>, Pt<sup>4+</sup>, and Pt<sup>0</sup> species are de-convoluted and marked on the figures.

### 3.3.3.3. Investigation of the chemical states of Pt species by H<sub>2</sub>-TPR Figure 3-11

(a) shows H<sub>2</sub>-TPR curves of Pt(2)/CeO<sub>2</sub> 500C and 800C catalysts. The reduction peak at ~850 °C originates from the reduction of CeO<sub>2</sub> bulk, while the reduction peaks below 300 °C originate from the reduction of CeO<sub>2</sub> surface and Pt-O-Ce bonds [14]. As shown in Figure 3-11 (a), when the oxidation temperature was raised from 500 to 800 °C, the surface reduction peak of Pt(2)/CeO<sub>2</sub> shifted from 165 to 240~270 °C, while the bulk reduction peak was not affected. The surface reduction peak of Pt(2)/(800C)CeO<sub>2</sub> also shifted from 60 and 115 °C to 64 and 143 °C, respectively, when the oxidation temperature was increased from 500 to 800 °C (Figure 3-11 (b)). This could be attributed to the diffusion of Pt species into CeO<sub>2</sub>'s structure [14]. In addition, the reduction peak of Pt(2)/(800C)CeO<sub>2</sub> below 300 °C dwindled in intensity when the oxidation temperature was raised from 500 to 800 °C, probably because of the Pt sintering with the loss of PtO<sub>2</sub> species. The extent of shift is not significant in Pt(2)/(800C)CeO<sub>2</sub> than in Pt(2)/CeO<sub>2</sub>. Pt species on (800C)CeO<sub>2</sub> may hardly diffuse into the support at the high temperature unlike Pt species on CeO<sub>2</sub>, since much of the Pt species on (800C)CeO<sub>2</sub> are not bound in the form of Pt-O-Ce bond as proposed based on CO chemisorption curves (Figure 3-8 and 3-9) and XP spectra (Figure 3-10). Quantitative analysis of XPS results in Table 3-3 supports the proposal. When the oxidation temperature was raised from 500 to 800 °C, the Pt/Ce ratio was decreased by 34 % on Pt(2)/CeO<sub>2</sub>, while the Pt/Ce ratio on Pt(2)/(800C)CeO<sub>2</sub> was decreased by 23%. The limited diffusion of Pt species on (800C)CeO<sub>2</sub> may result in the smaller decrease in the Pt/Ce ratio on Pt(2)/(800C)CeO<sub>2</sub> than on Pt(2)/CeO<sub>2</sub>. The

weakened interaction between Pt and CeO<sub>2</sub> on Pt(2)/(800C)CeO<sub>2</sub> would decrease the extent of the peak shift in H<sub>2</sub>-TPR after the oxidative treatment at 800 °C.

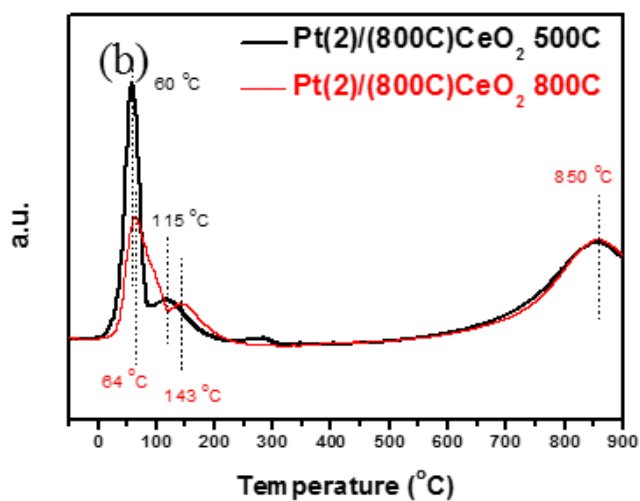
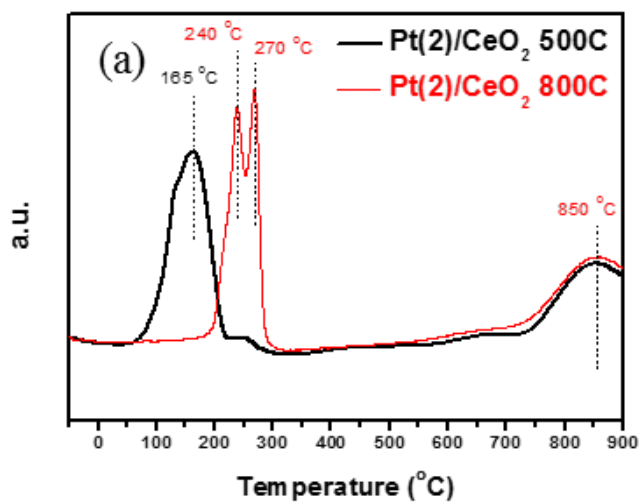


**Figure 3-11.** Cryo H<sub>2</sub>-TPR curves of (a) Pt(2)/CeO<sub>2</sub> and (b) Pt(2)/(800C)CeO<sub>2</sub> catalysts after oxidative treatments at 500 and 800 °C.

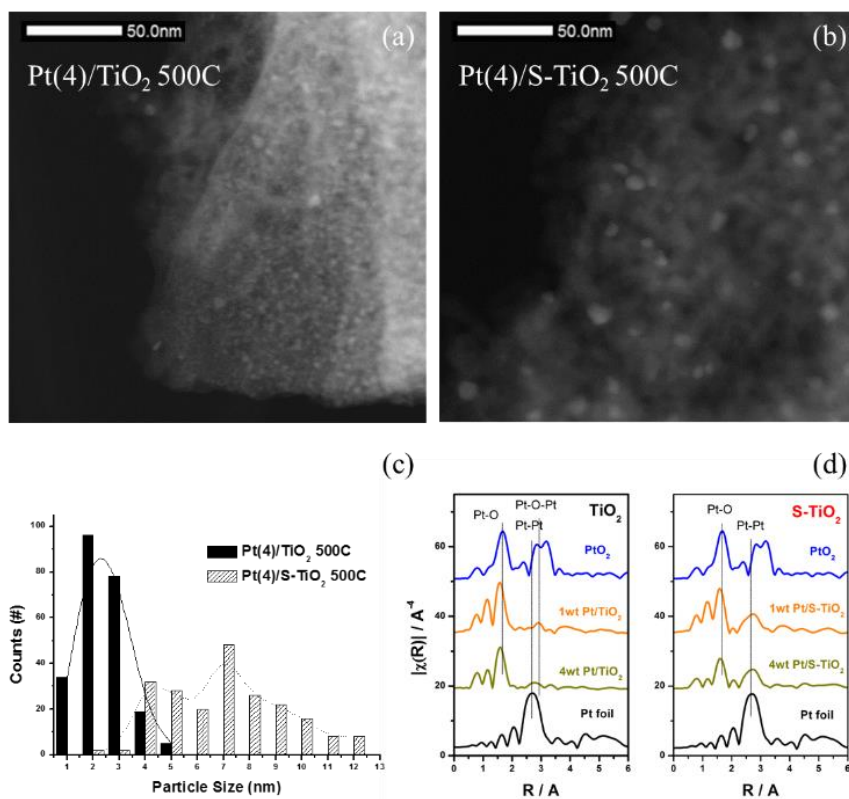
**3.3.4. S dopants on TiO<sub>2</sub> surface weakens the Pt-TiO<sub>2</sub> interaction and improves the CO oxidation ability of Pt/TiO<sub>2</sub> catalysts** Commercial TiO<sub>2</sub> (DT-51) contains 1.25 wt.% of sulfur (from elemental analysis) [77], and it is designated as S-TiO<sub>2</sub> in this work. Sulfur-free titania (TiO<sub>2</sub>) was synthesized by conventional sol-gel method to resemble the physical properties of S-TiO<sub>2</sub>. After calcination at 500 °C, BET surface area of S-TiO<sub>2</sub> is 88 m<sup>2</sup>/g while that of TiO<sub>2</sub> is 86 m<sup>2</sup>/g. Crystalline structure (from XRD pattern), BET surface area and pore structure of both TiO<sub>2</sub> and S-TiO<sub>2</sub> were preserved after Pt impregnation and calcination at 500 °C (data not shown). HAADF-STEM images of Pt(4)/TiO<sub>2</sub> and Pt(4)/S-TiO<sub>2</sub> are compared in Figure 3-12. In the case of Pt(4)/TiO<sub>2</sub>, small Pt particles with the average size of 2.5 nm are highly dispersed on TiO<sub>2</sub>. However, relatively large Pt particles with the average size of 7.5 nm are observed on Pt(4)/S-TiO<sub>2</sub> (See also particle size distribution curves in Figure 3-12 (c)). EXAFS spectra in Figure 3-12 (d) also show that the coordination number of Pt-Pt shell was larger on Pt/S-TiO<sub>2</sub> than Pt/TiO<sub>2</sub>, indicating that larger Pt clusters are formed on the former sample.

Figure 3-13 shows Pt L3-edge XANES spectra over Pt/TiO<sub>2</sub> and Pt/S-TiO<sub>2</sub>. The white line intensity is closely related to the oxidation state of Pt [78]. XANES spectra of Pt(1 and 4)/TiO<sub>2</sub> are very similar to that of PtO<sub>2</sub> reference, indicating that the Pt species are almost fully oxidized to Pt<sup>4+</sup> state. On the other hand, the white line intensity of Pt species on S-TiO<sub>2</sub> was relatively low, pointing out that Pt species are not fully oxidized. In addition, the white line intensity is slightly lower on catalysts

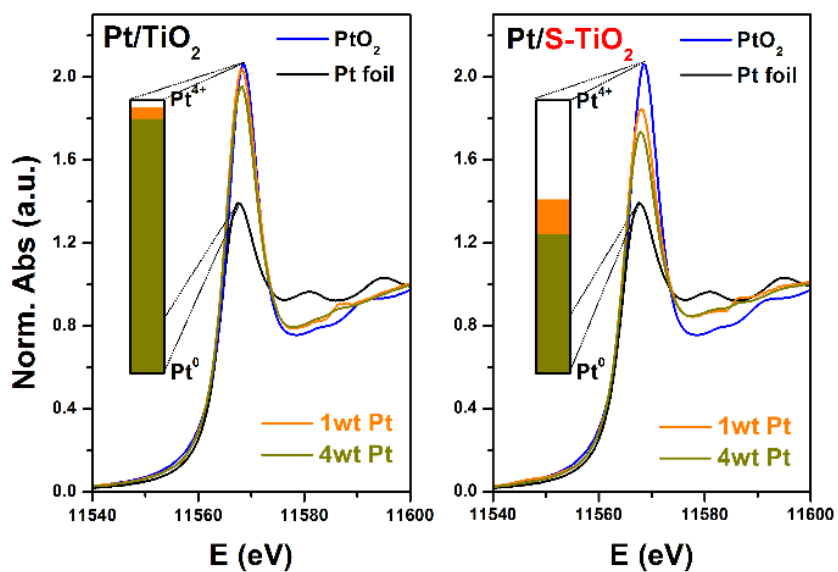
with the higher Pt loading, implying that Pt aggregated to form the larger metallic clusters at high Pt loading.

Figure 3-14 (a) shows the light-off curves of CO oxidation over Pt/TiO<sub>2</sub> 500C and Pt/S-TiO<sub>2</sub> 500C catalysts. It should be noted that the same light-off curves were obtained in the subsequent repeated reactions. Interestingly, Pt(1)/S-TiO<sub>2</sub> shows significantly higher catalytic activity compared with Pt(1)/TiO<sub>2</sub>; T<sub>50</sub> of the former is 50 °C lower than the latter. In addition, Pt(4)/S-TiO<sub>2</sub> also exhibited the lower T<sub>50</sub> than Pt(4)/TiO<sub>2</sub> by more than 50 °C. According to STEM images of Figure 3-12, Pt dispersion is much higher on Pt/TiO<sub>2</sub> catalysts than on Pt/S-TiO<sub>2</sub> catalysts. Since CO oxidation ability of Pt/TiO<sub>2</sub> is much lower than that of Pt/S-TiO<sub>2</sub>, Pt dispersion would not be the decisive factor in determining the CO oxidation ability. Note also that the amount of Pt loaded is not the dominant factor because the CO oxidation ability of Pt(4)/TiO<sub>2</sub> is quite similar to that of Pt(1)/S-TiO<sub>2</sub>. Assuming that Pt species exist either as Pt<sup>0</sup> or Pt<sup>4+</sup>, XANES spectra were curve-fitted by the linear combination of XANES spectrum of Pt foil and PtO<sub>2</sub> reference materials. T<sub>50</sub> of each catalyst is plotted as a function of the relative amount of metallic Pt in Figure 3-14 (b); as the amount of metallic Pt increased, T<sub>50</sub> of catalysts decreased. This phenomenon is in agreement with the proposal made by Ding et al., who reported that metallic Pt clusters showed the better CO oxidation ability than ionic Pt species [18]. Thus, S-TiO<sub>2</sub> can effectively retain metallic Pt species under the oxidizing condition, which is beneficial for CO oxidation.

Therefore, it can be summarized that when loading Pt, sulfate species on TiO<sub>2</sub> may have weakened the interaction between Pt and TiO<sub>2</sub> [16]. This can lead to a low dispersion of Pt loaded on S-TiO<sub>2</sub> and the formation of relatively large Pt clusters, which gives Pt species more metallic properties, resulting in the higher CO oxidation ability of Pt/S-TiO<sub>2</sub> than Pt/TiO<sub>2</sub> counterparts [16].



**Figure 3-12.** HAADF-STEM images of (a) Pt(4)/TiO<sub>2</sub> 500C and (b) Pt(4)/S-TiO<sub>2</sub> 500C catalysts. (c) Particle size distributions of Pt particles. (d) Fourier Transform of k<sup>3</sup>-weighted EXAFS spectra at the Pt L3-edge of Pt/TiO<sub>2</sub> 500C and Pt/S-TiO<sub>2</sub> 500C catalysts compared to those of reference Pt foil and PtO<sub>2</sub>.



**Figure 3-13.** XANES spectra at the Pt L3-edge of Pt/TiO<sub>2</sub> 500C and Pt/S-TiO<sub>2</sub> 500C in comparison with those of reference PtO<sub>2</sub> and Pt foil.

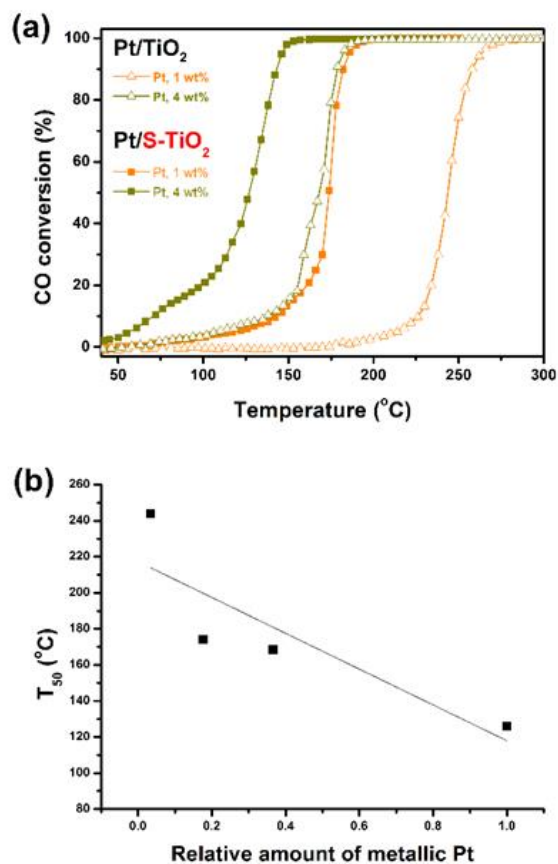


**Figure 3-14.** (a) Comparison of the CO conversion curves for Pt/TiO<sub>2</sub> 500C and Pt/S-TiO<sub>2</sub> 500C catalysts. (b) The temperature of 50 % conversion (T<sub>50</sub>) in CO oxidation over various Pt/TiO<sub>2</sub> 500C catalysts as a function of the relative amount of metallic Pt in catalysts. Relative amount of metallic Pt was obtained from the linear combination analysis of XANES spectra of Pt/TiO<sub>2</sub> catalysts, assuming only Pt and PtO<sub>2</sub> species are present on the catalysts. XANES spectra of Pt foil and PtO<sub>2</sub> were taken as references.

# **Chapter 4. Synthesis of Pt nanoparticles encapsulated in CeO<sub>2</sub> over-layers by controlled reduction treatment to suppress CH<sub>4</sub> formation in high-temperature Water-Gas-Shift reaction**

## **4.1. Introduction**

In recent years, TM(Transition Metal)/CeO<sub>2</sub> (e.g. Pt/CeO<sub>2</sub>) has received considerable research attention as the candidate catalyst for the Water-Gas-Shift (WGS) reaction [9, 61, 79, 80]. However, most researches have focused on Low-Temperature (LT) (< 350 °C) WGSR, while High Temperature (HT) (> 400 °C) WGSR activity of TM/CeO<sub>2</sub> catalysts have gained little attention. Yeung et al. pointed out that many current studies on the WGSR activity of TM/CeO<sub>2</sub> catalysts focus on low-temperature mobile applications (i.e., fuel cell vehicles) because TM/CeO<sub>2</sub> catalysts are more active than commercially available shift catalysts [81]. For stationary applications, however, high concentration of H<sub>2</sub> and CO promote undesirable side reactions at high temperatures on TM during WGSR, such as methanation reaction [81]. For this reason, TM/CeO<sub>2</sub> catalysts have not been considered as the high-temperature WGSR catalyst in spite of their high activity in WGSR [81]. Therefore, to utilize TM/CeO<sub>2</sub> as HT-WGSR catalysts, CH<sub>4</sub> formation on TM should be suppressed.

There have been several attempts to suppress methanation reaction during WGS on TM/CeO<sub>2</sub> catalysts. For example, Kawi et al. have attempted various strategies, such as adding alkali metal additives or forming Ni-Cu alloys, to suppress the undesired CH<sub>4</sub> production on Ni/CeO<sub>2</sub> based WGS catalysts [82, 83]. They tried to change the CO adsorption properties of active Ni sites to suppress the CH<sub>4</sub> formation [82, 83]. Tsang et al. have also published a series of papers that synthesized Pt@CeO<sub>2</sub> core-shell catalysts to block the exposed Pt sites, the active site of methanation reaction, with CeO<sub>2</sub> [81, 84, 85]. They observed the complete suppression of CH<sub>4</sub> formation when Pt is not exposed.

In addition, Tsang et al. reported that electronic interaction between Pt and CeO<sub>2</sub> transformed catalytically inactive CeO<sub>2</sub> surface into catalytically active one [81]. This was the interesting observation because many previous works have focused on the catalytic activities of atomically dispersed Pt<sup>2+</sup> species or the interfacial region between Pt NP and CeO<sub>2</sub>.

Although the core-shell type Pt@CeO<sub>2</sub> catalysts first reported by Tsang et al. were successful in inhibiting methanation reaction during HT-WGS, the micro-emulsion technique used for the synthesis requires the use of expensive cetyltrimethylammonium bromide (CTAB) [81]. In this contribution, the new approach to prepare Pt/CeO<sub>2</sub> catalysts with suppressed CH<sub>4</sub> formation during HT-WGS is proposed. The controlled reductive treatments were applied to modify the structure of 'Pt on CeO<sub>2</sub>'. The prepared 'Pt in CeO<sub>2</sub>' showed the comparable WGS activity to the conventional 'Pt on CeO<sub>2</sub>' while the CH<sub>4</sub> formation was greatly

suppressed. Compared to many previous struggles to encapsulate TM particles, our approach has the advantage in utilizing simple thermal treatments to prepare 'Pt in CeO<sub>2</sub>'. In addition, the catalytic nature of CeO<sub>2</sub> over-layers on Pt NP was studied in detail by using various characterization techniques such as CO chemisorption, XPS and in-situ DRIFT.

## 4.2. Experimental

**Catalyst Synthesis** CeO<sub>2</sub> (Rhodia) has a surface area of 135 m<sup>2</sup>/g. 2 wt% of Pt was loaded on CeO<sub>2</sub> by incipient wetness impregnation method with aqueous Pt(NH<sub>3</sub>)<sub>4</sub>(NO<sub>3</sub>)<sub>2</sub> (Sigma Aldrich, 99.99 % grade, metal basis) solution as a metal precursor at room temperature. After impregnation, catalysts were dried in an oven at 100 °C for 24 h. Dried catalysts were oxidized under 15 % O<sub>2</sub>/N<sub>2</sub> for 2 h at specific temperature. For example, Pt(2)/CeO<sub>2</sub> 500C represents that Pt(2)/CeO<sub>2</sub> was oxidized at 500 °C.

The structure of Pt(2)/CeO<sub>2</sub> was modified by two different methods. In the first method, samples were reduced under 10 % H<sub>2</sub>/N<sub>2</sub> for 2 h at specific temperature (R treatment). For example, Pt(2)/CeO<sub>2</sub> 800R represents that Pt(2)/CeO<sub>2</sub> 500C was reduced at 800 °C. In the second method, after reduction at 250 °C for 2 h (with 10 % H<sub>2</sub>/N<sub>2</sub>), samples were N<sub>2</sub> treated for 2 h at specific temperature (NC treatment). For example, Pt(2)/CeO<sub>2</sub> 800NC represents that Pt(2)/CeO<sub>2</sub> 500C was reduced at 250 °C and sequentially N<sub>2</sub> treated at 800 °C. Flow rate was 100 mL/min and ramping rate was 10 °C/min.

**CO chemisorption.** The pulsed-CO chemisorption was performed on BET-CAT-II (BEL Japan Inc.) at -78 and 50 °C with the experimental procedures proposed by Tanabe et al. [46]. 0.05 g of sample was oxidized at 400 °C for 15 min. After purging with He, the sample was reduced at the same temperature for 15 min under the 10% H<sub>2</sub>/N<sub>2</sub> flow. After cooling the temperature to -78 or 50 °C, the CO pulses were

introduced to the catalysts until the adsorption reached the saturation.

**Catalytic evaluation.** WGSR was performed in a fixed bed reactor at atmospheric pressure. 0.06 g of catalyst was used. The feed mixtures were prepared using mass flow controllers (MKS Instruments, Inc.). The WGSR activity was evaluated under several different reaction conditions; **i**) 3 % CO, 24 % H<sub>2</sub>O, **ii**) 3 % CO, 24 % H<sub>2</sub>O, 3 % CO<sub>2</sub>, **iii**) 3 % CO, 24 % H<sub>2</sub>O, 20 % H<sub>2</sub>, and **iv**) 3 % CO, 24 % H<sub>2</sub>O, 3 % CO<sub>2</sub>, 20 % H<sub>2</sub>. The methanation reaction was conducted with 3 % CO, 20 % H<sub>2</sub>. The total flow rate was 70 mL/min. He was used as the balance gas. Gas streams before and after the catalytic reaction were analyzed online using a TCD and a parallel gas chromatography (GC, Younglin, Inc.) equipped with a Carboxen 1000 column and a flame ionization detector (FID). In addition, a methanizer was employed to convert CO and CO<sub>2</sub> to CH<sub>4</sub> for product quantification by FID. The conversion data were collected during 30 min of steady-state operation at each temperature. Prior to each catalytic measurement, the catalysts were pretreated in 5% H<sub>2</sub>/He at 500 °C for 1 h.

In this work, H<sub>2</sub>O/CO is 8. When H<sub>2</sub>O/CO is high, the rate of WGSR can be assumed to be first-order in CO as follows (equation (1)) [86]:

$$r_{co} = kC_{co} \quad (1)$$

where k is reaction rate constant (s<sup>-1</sup>) and C<sub>co</sub> is the molar CO concentration (mol/m<sup>3</sup>). The differential equation can be derived by using the plug flow reactor model (equation (2)) [87]:

$$\frac{dC_{co}}{dV_{cat}} = -\frac{P_t r_{co}}{FR T} = -\frac{P_t k}{FR T} C_{co} \quad (2)$$

where  $F$  is the total gas molar flow rate (mol/s),  $V_{cat}$  is the catalyst bed volume ( $m^3$ ),  $r$  is the reaction rate per catalyst bed volume (mol/s/ $m^3$ ),  $P_t$  is the total pressure,  $R$  is the ideal gas constant (8.314 J/mol/K) and  $T$  is the temperature (K). By absorbing the temperature in equation (2) into reaction rate constant  $k$ , equation (2) can be rewritten as (equation (3)):

$$\frac{dC_{co}}{dV_{cat}} = -\frac{P_t}{FR} k' C_{co} = -\frac{P_t}{FR} A' e^{-E'/RT} C_{co} \quad (3)$$

where  $A'$  is the pre-exponential factor and  $E'$  is the apparent activation energy (J/mol). Integration of equation (3) yields equation (4):

$$\ln(1 - x) = -\frac{P_t}{FR} V_{cat} A' e^{-E'/RT} \quad (4)$$

where  $x$  is the CO fractional conversion. Equation (4) can be rewritten into equation (5):

$$\ln(-\ln(1 - x)) = -\frac{E'}{RT} + \ln\left(\frac{P_t}{FR} V_{cat} A'\right) \quad (5)$$

Linear fitting of  $1/T$  vs  $\ln(-\ln(1 - x))$  can derive apparent activation energy ( $E'$ ).

**X-ray photoelectron spectroscopy (XPS)** XPS analysis was conducted on a AXIS-HSi (Kratos) instrument with Mg K $\alpha$  radiation (450 W). The charging effect was corrected with respect to the C 1s binding energy of 284.5 eV and the Ce 4f binding energy ( $u''$ ) of 916.7 eV. Spectra were processed using casaXPS. The chemical composition of catalysts was calculated using the integral intensities of lines of each component considering atomic sensitivity factors [39]. XPS spectra were measured five times to calculate the standard deviation of Pt to Ce molar ratio. Depth-profiling XPS analysis was conducted on a K-alpha (Thermo VG, U.K.) instrument with monochromated Al X-ray radiation (360W). XP spectra were collected sequentially after Ar sputtering treatments (500 eV, raster size 2 mm x 2 mm).

**Diffuse Reflectance Infrared Fourier Transform spectroscopy (DRIFT) study** In-situ DRIFT experiments were conducted in a diffuse reflectance cell (Praying Mantis, Harrick) installed in a Fourier transform infrared (FT-IR) spectrometer (iS-50, Thermo Fisher Scientific) with an MCT detector. Before measuring spectra, samples were reduced at 500 °C for 30 min with 10 % H<sub>2</sub>/N<sub>2</sub> followed by the N<sub>2</sub> treatment at 500 °C for 30 min. Background spectra were obtained after cooling the sample temperature to 100 °C under N<sub>2</sub> flow. 2 % CO was added to the sample for 60 min, after which spectra did not change. This is followed by the N<sub>2</sub> purging for 60 min. 1.5  $\mu$ L/min of H<sub>2</sub>O was added to the sample for 60 min with the syringe pump. The total flow rate was 50 mL/min with N<sub>2</sub> balance gas.

**Powder X-ray diffraction (XRD), Surface area measurement, H<sub>2</sub> temperature programmed reduction (H<sub>2</sub>-TPR), High-angle annular-dark-field Scanning transmission electron microscopy (HAADF-STEM) and Energy-dispersive spectroscopy (EDS)** Experimental procedures are same as those depicted in Chapter 2.2. and 3.2.

## 4.3. Results

**4.3.1. Synthesis of ‘Pt in CeO<sub>2</sub>’ with the controlled reductive treatment** To bury Pt NP beneath CeO<sub>2</sub> over-layers, the catalytic structure of Pt(2)/CeO<sub>2</sub> was modified by using two different methods; **1.** by the reductive treatment to reduce CeO<sub>2</sub> bulk (R treatment) and **2.** by the reductive treatment at 250 °C followed by the thermal treatment with N<sub>2</sub> (NC treatment).

The pore structure of Pt(2)/CeO<sub>2</sub> did not change considerably by the oxidative treatment at 800 °C since the strong Pt-O-Ce bonds maintained the Pt/CeO<sub>2</sub> structure from high temperature treatments [14]. However, under the reducing environment, Pt-O-Ce bonds are reduced almost completely at 250 °C, and the textural property of Pt(2)/CeO<sub>2</sub> significantly changed after high temperature treatments [33]. Figure 4-1 (a) shows the BJH pore distribution curves of Pt(2)/CeO<sub>2</sub> after R treatments. The average pore diameter of Pt(2)/CeO<sub>2</sub> changed only little after 500R treatment. However, the reduction temperature above 500 °C can reduce CeO<sub>2</sub> bulk and significantly modified the structure of Pt(2)/CeO<sub>2</sub>. The average pore diameter of Pt(2)/CeO<sub>2</sub> increased from 8.5 to 11.3, 23.8 and 50 nm after the 600R, 700R and 800R treatments, respectively (Table 4-1). Figure 4-1 (b) shows the BJH pore distribution curves of Pt(2)/CeO<sub>2</sub> 500C after the NC treatments. The average pore diameter of Pt(2)/CeO<sub>2</sub> 500C was increased from 8.5 to 9.3, 17.4 and 28.5 nm after the 600NC, 700NC and 800NC treatments, respectively (Table 4-1). The average pore diameter of Pt/CeO<sub>2</sub> is smaller after NC treatment than after R treatment.

Since N<sub>2</sub> flow cannot reduce the CeO<sub>2</sub> bulk, the residual bulk oxygen in the former catalyst would protect the structure of catalysts from collapsing [14].

Pulsed CO chemisorption was performed at -78 °C to accurately measure Pt dispersion. Figure 4-1 (c) and Table 4-2 display the estimated Pt dispersion after various treatments. R treatment decreased Pt dispersion more drastically than NC treatment. For example, Pt dispersion already decreased to 1.9 % after 600R treatment while it was 14.1 % after 600NC treatment. In addition, 800R and 800NC treatments decreased the Pt dispersion of Pt(2)/CeO<sub>2</sub> 500C significantly from 61.1 to 0.5 and 5.1 %, respectively. The pulsed CO chemisorption results indicate that the Pt NP size should be very large; 218.4 nm and 22.1 nm after 800R and 800NC treatments, respectively (Table 4-2).

However, such large Pt NP were not observed in HAADF-STEM images of Pt(2)/CeO<sub>2</sub> 800R (Figure 4-2 (a)) and 800NC (Figure 4-2 (b)). XRD patterns in Figure 4-2 (f) also indicate that large Pt NPs do not exist in Pt(2)/CeO<sub>2</sub> 800R and 800NC, since the intensity of XRD peak at 39.5 ° from Pt NP is small. Figure 4-2 (c) shows Pt NP size distribution curves of Pt(2)/CeO<sub>2</sub> 800R and 800NC. Most of Pt NP were below 5 nm in size, although some Pt NP larger than 5 nm were also observed in 800R treated sample. In addition, the small XRD peak from Pt NP was observed only in 800R treated sample (Figure 4-2 (f)). Since the detecting limit of XRD apparatus used in this study is 5 nm, this supports the observation from size distribution curves that Pt NP larger than 5 nm exist only in 800R treated sample. This difference between 800R and 800NC samples would be caused by the more severe change in the structure

after R treatment as discussed in Figure 4-1. Indeed, XRD patterns in Figure 4-1 (e) indicate that the size of CeO<sub>2</sub> agglomerate was 31.1 and 48.4 nm on Pt(2)/CeO<sub>2</sub> 800NC and 800R, respectively. The Pt dispersion of Pt(2)/CeO<sub>2</sub> 800R and 800NC catalysts measured by CO chemisorption and Pt particle size distribution curves from TEM images are compared in Figure 4-2 (d). According to particle size distribution curves, Pt dispersion is 37 and 56 % after 800R and 800NC treatments, respectively, indicating that the majority of decrease in the amount of CO chemisorption does not originate from Pt sintering. Instead, CeO<sub>2</sub> over-layers on Pt NP would inhibit CO adsorption on Pt surface.

Figure 4-3 illustrates how R and NC treatments encapsulated Pt NP by CeO<sub>2</sub> over-layers. R treatment could reduce the oxygen in both surface and bulk of CeO<sub>2</sub>. Upon the reduction of CeO<sub>2</sub> bulk, Pt NP would sink into the voids of CeO<sub>2</sub> bulk. On the other hand, NC treatment could only reduce the surface of Pt/CeO<sub>2</sub>. At high temperature under the N<sub>2</sub> flow, Pt NPs are covered by CeO<sub>2</sub> over-layers. However, Pt NPs could not sink into CeO<sub>2</sub>'s structure in NC treated samples because there are no voids in CeO<sub>2</sub> bulk. In the next section, WGS activities of 'Pt in CeO<sub>2</sub>' catalysts will be investigated.

| <b>Pt(2)/CeO<sub>2</sub><br/>Sample</b> | <b>CeO<sub>2</sub> particle<br/>size<br/>(nm)<sup>a</sup></b> | <b>Surface<br/>area<br/>(m<sup>2</sup>/g)<sup>b</sup></b> | <b>Pore<br/>volume<br/>(cm<sup>3</sup>/g)<sup>c</sup></b> | <b>Mean Pore<br/>Size<br/>(nm)<sup>c</sup></b> |
|---|---|---|---|--|
| <b>500C</b>                             | <b>8.7</b>  | <b>125</b>  | <b>0.27</b>   | <b>8.5</b>                                     |
| 800C                                    | 9.8   | 111   | 0.27  | 9.8  |
| 500R                                    | -   | 116   | 0.27  | 9  |
| 600R                                    | -   | 94  | 0.27  | 11.3   |
| 700R                                    | -   | 45  | 0.27  | 23.8   |
| <b>800R</b>                             | <b>48.4</b>   | <b>17</b>   | <b>0.04</b>   | <b>~50</b>                                     |
| 600NC                                   | -   | 115   | 0.27  | 9.3  |
| 700NC                                   | -   | 58  | 0.25  | 17.4   |
| <b>800NC</b>                            | <b>31.1</b>   | <b>33</b>   | <b>0.23</b>   | <b>28.5</b>                                    |

**a.** From XRD, Scherrer equation **b.** From N<sub>2</sub> adsorption branch, BET **c.** From N<sub>2</sub> desorption branch, BJH

**Table 4-1.** Physiochemical properties of Pt(2)/CeO<sub>2</sub> catalysts, after various thermal treatments.

| Pt(2)/CeO <sub>2</sub> catalysts | The amount of CO adsorbed @ -78 °C (mmol/g) | Pt dispersion (%) <sup>a</sup> | Pt particle size (nm) <sup>a</sup> | Pt dispersion (%) <sup>b</sup> | Pt particle size (nm) <sup>b</sup> |
|----------------------------------|---|--------------------------------|------------------------------------|--------------------------------|------------------------------------|
| 500C                             | 0.064                                       | 61.1                           | 1.9                                | -                              | -                                  |
| 600R                             | 0.002                                       | 1.9                            | 59.7                               | -                              | -                                  |
| 700R                             | 0.003                                       | 3.1                            | 36.7                               | -                              | -                                  |
| 800R                             | 0.001                                       | 0.5                            | 218.4                              | 37                             | 2.4                                |
| 600NC                            | 0.015                                       | 14.1                           | 8.1                                | -                              | -                                  |
| 700NC                            | 0.013                                       | 12.1                           | 9.3                                | -                              | -                                  |
| 800NC                            | 0.005                                       | 5.1                            | 22.1                               | 56                             | 4.0                                |

**a.** From pulsed CO chemisorption at -78 °C **b.** From HAADF STEM,  $d_p = (\sum nd^3 / \sum nd^{2.19})^{1.23}$ ,  $D (\%) = 115.4/d_p^{0.81}$

**Table 4-2.** Average Pt NP size and Pt dispersion, measured from pulsed CO chemisorption at -78 °C and particle size distribution curves obtained from HAADF-STEM images.

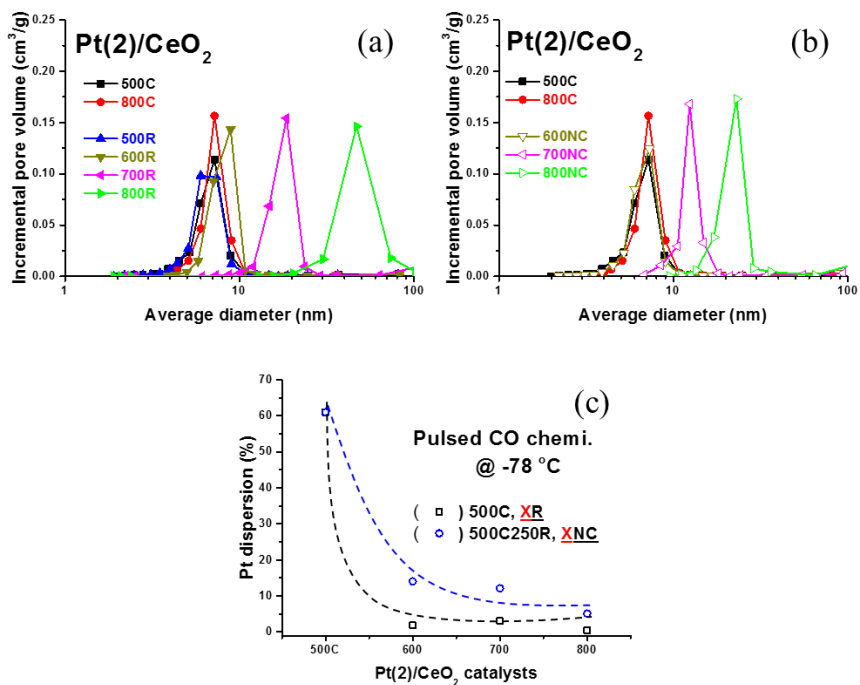


**Figure 4-1.** BJH pore distribution curve of Pt(2)/CeO<sub>2</sub> XR and XNC catalysts are displayed in (a) and (b), respectively. (c) Apparent Pt dispersion was measured from pulsed CO chemisorption at -78 °C.

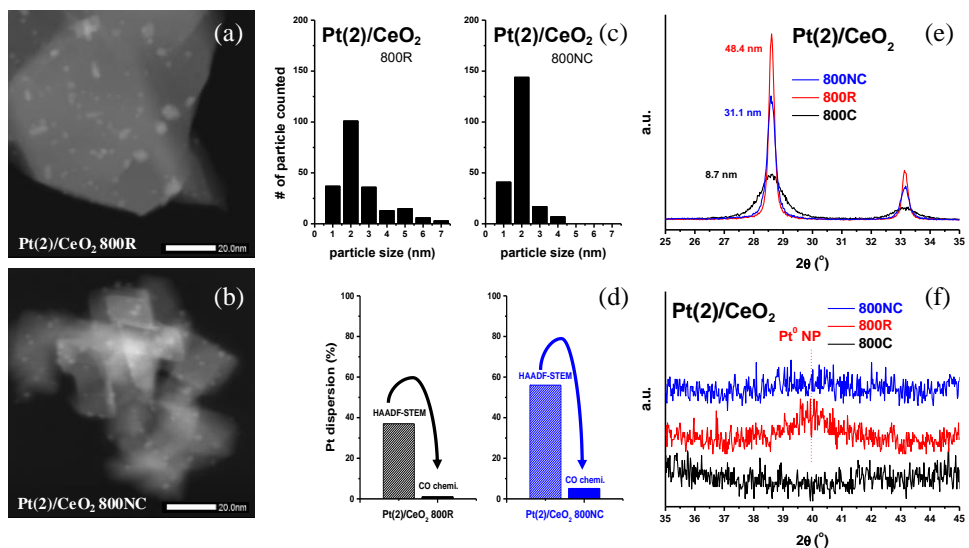


**Figure 4-2.** HAADF-STEM images of Pt(2)/CeO<sub>2</sub> 800R (a) and 800NC (b); corresponding particle size distribution curves are displayed in (c). (d) The comparison of Pt dispersion measured by HAADF-STEM images and CO chemisorption, which indicate that Pt nanoparticles are covered by CeO<sub>2</sub> over-layers. (e) XRD patterns of Pt/CeO<sub>2</sub> catalysts in the 2θ region between 25 and 35 ° to observe peaks from fluorite structured CeO<sub>2</sub> particles. (f) XRD patterns of Pt/CeO<sub>2</sub> catalysts in the 2θ region between 35 and 45 ° to observe the peak from agglomerated Pt clusters at 39.5 °.

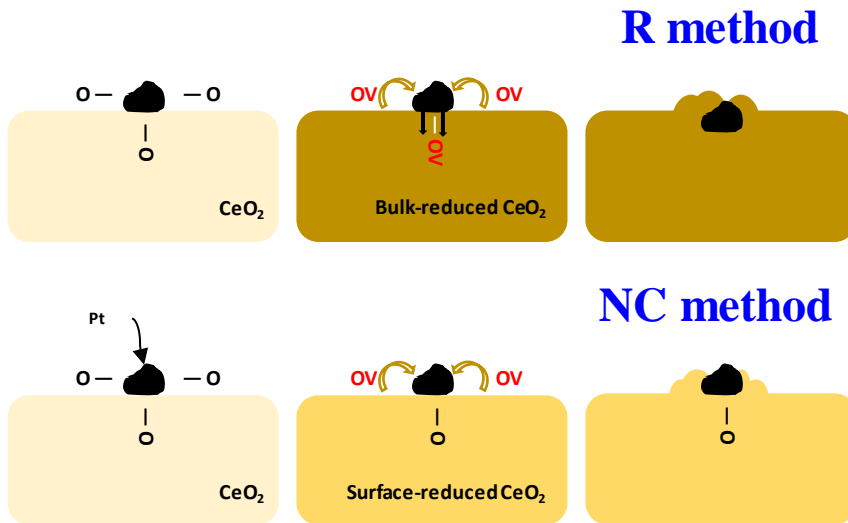


**Figure 4-3.** Schematics displaying the effect of XR and XNC treatments in the structure of Pt/CeO<sub>2</sub> catalysts.

**4.3.2. Comparison of WGS activity and CH<sub>4</sub> yield of ‘Pt on CeO<sub>2</sub>’ and ‘Pt in CeO<sub>2</sub>’ catalysts** Pt/CeO<sub>2</sub> catalysts are known to have high WGS activity [9, 88]. However, Pt NP also promote CO-H<sub>2</sub> reaction to produce CH<sub>4</sub>. Yeung et al. synthesized Pt@CeO<sub>2</sub> core-shell catalysts, with Pt core and CeO<sub>2</sub> shell, which showed good HT-WGS activity with suppressed CH<sub>4</sub> formation [81]. They suggested that (i) Pt surface should not be exposed to CO to avoid CH<sub>4</sub> formation and (ii) the Pt-CeO<sub>2</sub> interaction could promote WGS on CeO<sub>2</sub> surface. In this study, by modifying the catalysts’ structure, CeO<sub>2</sub> over-layers are formed on Pt NP without using expensive organic compounds. Therefore, presently synthesized catalysts may meet the criteria for having good HT-WGS activity with suppressed CH<sub>4</sub> formation.

**4.3.2.1. WGS activity** WGS activities of Pt(2)/CeO<sub>2</sub> 800R and Pt(2)/CeO<sub>2</sub> 800NC (‘Pt in CeO<sub>2</sub>’) were tested, and their activities were compared to that of Pt(2)/CeO<sub>2</sub> 500C (‘Pt on CeO<sub>2</sub>’). In addition, WGS activities were tested under various gaseous streams with or without H<sub>2</sub> and CO<sub>2</sub> gases. H<sub>2</sub> and CO<sub>2</sub> gases are always included in the reactant stream of practical applications, and it would be important to understand they influence catalysts’ activity.

Figure 4-4 displays WGS activities of Pt(2)-CeO<sub>2</sub> catalysts under various conditions. The addition of H<sub>2</sub> or CO<sub>2</sub> decreased WGS activity Pt(2)/CeO<sub>2</sub> 500C (‘Pt on CeO<sub>2</sub>’) (Figure 4-4 (a)). When H<sub>2</sub> and CO<sub>2</sub> are added together, HT-WGS activity of ‘Pt on CeO<sub>2</sub>’ (at 400 and 450 °C) reached the thermodynamic limit [23].

On the other hand, the addition of H<sub>2</sub> or CO<sub>2</sub> enhanced WGS activity of Pt(2)/CeO<sub>2</sub> 800NC ('Pt in CeO<sub>2</sub>') (Figure 4-4 (b)). In addition, co-feeding of H<sub>2</sub> and CO<sub>2</sub> changed the reactivity of 'Pt in CeO<sub>2</sub>'; LT activity (<350 °C) improved while HT activity (> 350 °C) decreased with respect to the reactivity obtained with CO and H<sub>2</sub>O (Figure 4-4 (b)). When comparing WGS activity under the full feed (CO, H<sub>2</sub>O, H<sub>2</sub> and CO<sub>2</sub>), 'Pt in CeO<sub>2</sub>' showed the higher activity below 300 °C, while 'Pt on CeO<sub>2</sub>' showed the higher activity in the temperature range between 300 and 400 °C (Figure 4-5 (a)). When the activation energies were calculated assuming the plug flow reactor model, it was 6.5 and 19.2 kcal/mol on 'Pt in CeO<sub>2</sub>' and 'Pt on CeO<sub>2</sub>', respectively (Figure 4-5 (b)). This explains the higher LT activity of 'Pt in CeO<sub>2</sub>'. However, at 450 °C, both catalysts approached the thermodynamic limit [23], displaying the similar activity. Figure 4-4 (a) and (b) strongly propose that active sites and reaction mechanisms on 'Pt on CeO<sub>2</sub>' and 'Pt in CeO<sub>2</sub>' catalysts are completely different.

Table 4-3 summarizes HT-WGS activities (at 400 and 450 °C) of 'Pt on CeO<sub>2</sub>' (Pt(2)/CeO<sub>2</sub> 500C) and 'Pt in CeO<sub>2</sub>' (Pt(2)/CeO<sub>2</sub> 800R and 800NC) under various reactant compositions. Pt(2)/CeO<sub>2</sub> 800R displayed negligible WGS activity, but Pt(2)/CeO<sub>2</sub> 800NC showed the comparable activity to Pt(2)/CeO<sub>2</sub> 500C. For example, under the reactant stream composed of CO, H<sub>2</sub>O and CO<sub>2</sub>, the catalytic activity of Pt(2)/CeO<sub>2</sub> 800NC surpassed that of Pt(2)/CeO<sub>2</sub> 500C both at 400 and 450 °C. In addition, at 450 °C under the reactant stream composed of CO, H<sub>2</sub>O, H<sub>2</sub> and CO<sub>2</sub> (full gas), the catalytic activities of both Pt(2)/CeO<sub>2</sub> 500C and 800NC approached thermodynamic limit (~51 %) [23].

**4.3.2.2. CH<sub>4</sub> yield** Figure 4-4 (c) and Table 4-3 demonstrate that the CH<sub>4</sub> yield on ‘Pt in CeO<sub>2</sub>’ is lower than that on ‘Pt on CeO<sub>2</sub>’. CH<sub>4</sub> is produced from H<sub>2</sub> and CO [89]. Therefore, in the absence of H<sub>2</sub>, only small amount of CH<sub>4</sub> is formed. However, when H<sub>2</sub> is added to the feed, CH<sub>4</sub> formation is promoted. At 450 °C, the CH<sub>4</sub> yields on ‘Pt on CeO<sub>2</sub>’ and ‘Pt in CeO<sub>2</sub>’ were 8.3 and 2.7 %, respectively under CO, H<sub>2</sub>O and H<sub>2</sub>. Under this condition, the selectivity toward CH<sub>4</sub> of ‘Pt on CeO<sub>2</sub>’ and ‘Pt in CeO<sub>2</sub>’ is 9.2 and 3.2 %, respectively. Interestingly, when CO<sub>2</sub> was added to the feed, the CH<sub>4</sub> yield on ‘Pt in CeO<sub>2</sub>’ was further suppressed from 2.7 to 0.9 % (Figure 4-4 (c)). The addition of CO<sub>2</sub> decreased the selectivity toward CH<sub>4</sub> of ‘Pt in CeO<sub>2</sub>’ from 3.2 to 1.4 %. On the contrary, the addition of CO<sub>2</sub> did not alter the CH<sub>4</sub> yield of ‘Pt on CeO<sub>2</sub>’ (Figure 4-4 (c)). Under CO<sub>2</sub>, the selectivity to CH<sub>4</sub> of ‘Pt on CeO<sub>2</sub>’ increased from 9.2 to 16.8 %. In summary, CH<sub>4</sub> formation was suppressed on Pt/CeO<sub>2</sub> by forming CeO<sub>2</sub> over-layers on Pt NP. Besides, the CH<sub>4</sub> formation on ‘Pt in CeO<sub>2</sub>’ could be further suppressed by CO<sub>2</sub>.

The methanation reaction activities of Pt(2)/CeO<sub>2</sub> 500C (‘Pt on CeO<sub>2</sub>’) and Pt(2)/CeO<sub>2</sub> 800NC (‘Pt in CeO<sub>2</sub>’) are compared in Figure 4-6. Even though negligible amount of CH<sub>4</sub> was produced on ‘Pt in CeO<sub>2</sub>’ during WGS (Figure 4-4 (c)), the large amount of CH<sub>4</sub> was produced under the feed containing 3 % CO and 20 % H<sub>2</sub>. At 450 °C, the CH<sub>4</sub> yields of ‘Pt on CeO<sub>2</sub>’ and ‘Pt in CeO<sub>2</sub>’ were 45 and 34 %, respectively (Figure 4-6). Although ‘Pt in CeO<sub>2</sub>’ displayed the lower methanation activity than ‘Pt on CeO<sub>2</sub>’, the methanation activity results in Figure 4-6 cannot explain the low CH<sub>4</sub> yield observed on ‘Pt in CeO<sub>2</sub>’ during WGS. The low CH<sub>4</sub> yield of ‘Pt in CeO<sub>2</sub>’

during WGSR could be understood by the inhibitory effects of H<sub>2</sub>O and CO<sub>2</sub> in methanation reaction. Firstly, H<sub>2</sub>O decreased the CH<sub>4</sub> production by activating WGSR which is energetically more favorable [89]. H<sub>2</sub>O decreased the CH<sub>4</sub> production both on 'Pt on CeO<sub>2</sub>' and 'Pt in CeO<sub>2</sub>' (Figure 4-6). Second, CO<sub>2</sub> further suppressed the CH<sub>4</sub> formation but only on 'Pt in CeO<sub>2</sub>' (Figure 4-4 (c)). In 'Pt in CeO<sub>2</sub>', instead of Pt, CeO<sub>2</sub> over-layers would behave as active sites of methanation reaction. CO<sub>2</sub> strongly adsorbs on CeO<sub>2</sub> surface by forming carbonates or formates [90-92]; gaseous CO<sub>2</sub> would block CeO<sub>2</sub> surface to suppress CH<sub>4</sub> formation. However, CO<sub>2</sub> cannot prohibit the CH<sub>4</sub> formation on Pt NP of 'Pt on CeO<sub>2</sub>'. To sum up, by modifying catalysts' structure, the CH<sub>4</sub> formation was suppressed especially in the presence of H<sub>2</sub>O and CO<sub>2</sub>.

**4.3.2.3. R and NC treatments at other temperatures (600 & 700 °C)** The influence of R and NC treatments at various other temperatures on WGS activity was also investigated. R treatments decreased WGS activity of Pt/CeO<sub>2</sub> both under the simple feed (CO and H<sub>2</sub>O, Figure 4-7) and the full feed (CO, H<sub>2</sub>O, H<sub>2</sub> and CO<sub>2</sub>, Figure 4-8). Especially, WGS activity after 800R treatment was completely lost (Figure 4-7). This can be understood by the reduced number of active sites after R treatments (Figure 4-1 (c)). Hence, R treatments are inadequate in preparing HT-WGS catalysts. On the other hand, after 600NC and 700NC treatments, LT activity increased while HT activity decreased (Figure 4-9). The improvement in LT-WGS activity after 600NC and 700NC treatments is interesting. However, it is beyond the scope of present work. The CH<sub>4</sub> production at high temperature (> 400 °C) increased after 600NC and 700NC treatments probably due to the incomplete covering of Pt NPs by CeO<sub>2</sub> over-layers (Figure 4-9). Therefore, 600NC and 700NC treatments are inadequate in preparing HT-WGS catalysts. Although both 800R and 800NC treatments successfully covered Pt NP with CeO<sub>2</sub> over-layers (Chapter 4.3.1.), only 800NC treated sample displayed WGS activity. In Chapter 4.3.3., what caused such differences in R and NC treated samples will be explored.

| Reactant composition               | CO+H <sub>2</sub> O |                           | CO+H <sub>2</sub> O+H <sub>2</sub> |                           | CO+H <sub>2</sub> O+CO <sub>2</sub> |                           | CO+H <sub>2</sub> O+H <sub>2</sub> +CO <sub>2</sub> |                           |
|------------------------------------|---------------------|---------------------------|------------------------------------|---------------------------|-------------------------------------|---------------------------|---|---------------------------|
|                                    | CO conversion (%)   | CH <sub>4</sub> yield (%) | CO conversion (%)                  | CH <sub>4</sub> yield (%) | CO conversion (%)                   | CH <sub>4</sub> yield (%) | CO conversion (%)                                   | CH <sub>4</sub> yield (%) |
| <b>WGSR, @400 °C</b>               |                     |                           |                                    |                           |                                     |                           |   |                           |
| <b>Pt(2)/CeO<sub>2</sub> 500C</b>  | 98.8                | 0.17                      | 88.5                               | 2.7                       | 94.7                                | 0.3                       | 70.9  | 2.1                       |
| <b>Pt(2)/CeO<sub>2</sub> 800R</b>  | 3.9                 | 0.07                      | n.m. <sup>a</sup>                  | n.m. <sup>a</sup>         | n.m. <sup>a</sup>                   | n.m. <sup>a</sup>         | n.m. <sup>a</sup>                                   | n.m. <sup>a</sup>         |
| <b>Pt(2)/CeO<sub>2</sub> 800NC</b> | 79.1                | 0.01                      | 83.4                               | 0.8                       | 96.4                                | 0.1                       | 43.5  | 0.3                       |
| Reactant composition               | CO+H <sub>2</sub> O |                           | CO+H <sub>2</sub> O+H <sub>2</sub> |                           | CO+H <sub>2</sub> O+CO <sub>2</sub> |                           | CO+H <sub>2</sub> O+H <sub>2</sub> +CO <sub>2</sub> |                           |
| WGSR, @450 °C                      | CO conversion (%)   | CH <sub>4</sub> yield (%) | CO conversion (%)                  | CH <sub>4</sub> yield (%) | CO conversion (%)                   | CH <sub>4</sub> yield (%) | CO conversion (%)                                   | CH <sub>4</sub> yield (%) |
| <b>Pt(2)/CeO<sub>2</sub> 500C</b>  | 98.1                | 0.39                      | 90.1                               | 8.3                       | 91.6                                | 0.5                       | <b>51.7</b>   | <b>8.7</b>                |
| <b>Pt(2)/CeO<sub>2</sub> 800R</b>  | 3.6                 | 0.02                      | n.m. <sup>a</sup>                  | n.m. <sup>a</sup>         | n.m. <sup>a</sup>                   | n.m. <sup>a</sup>         | n.m. <sup>a</sup>                                   | n.m. <sup>a</sup>         |
| <b>Pt(2)/CeO<sub>2</sub> 800NC</b> | 97.1                | 0.03                      | 85.3                               | 2.7                       | 94.4                                | 0.3                       | <b>51.1</b>   | <b>0.7</b>                |

<sup>a</sup> not measured

**Table 4-3.** WGS reaction activity and CH<sub>4</sub> selectivity of Pt(2)/CeO<sub>2</sub> 500C, Pt(2)/CeO<sub>2</sub> 800R and Pt(2)/CeO<sub>2</sub> 800 NC at 400 and 450 °C. Reactant was composed of 3 % CO, 24 % H<sub>2</sub>O, (3 % CO<sub>2</sub>), (20 % H<sub>2</sub>), and He balance gas with the total flow rate of 70 mL/min.

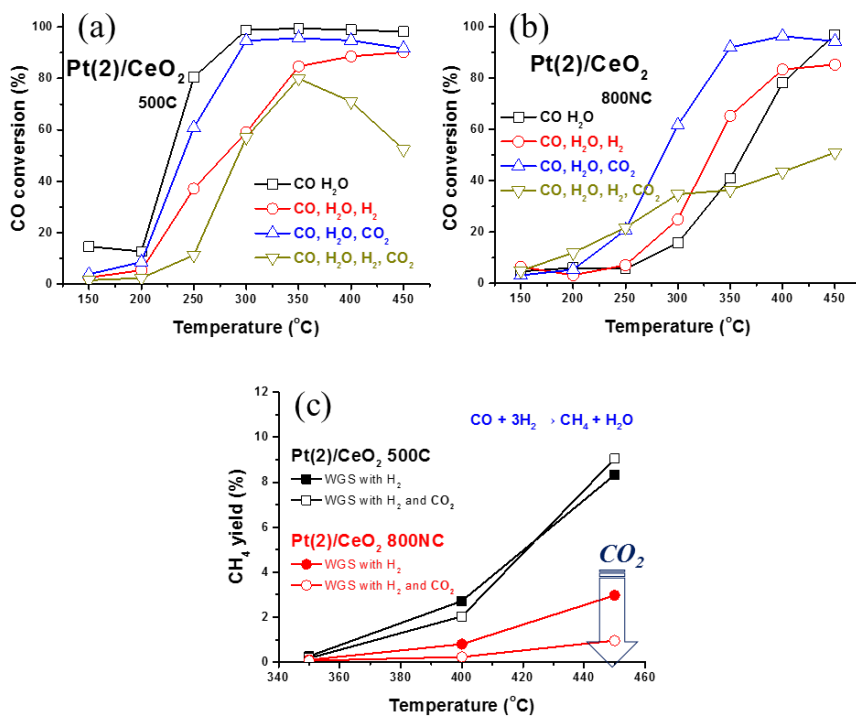


**Figure 4-4.** WGS reaction activity of Pt(2)/CeO<sub>2</sub> 500C (a) and Pt(2)/CeO<sub>2</sub> 800NC (b) catalysts under various feed conditions. The CH<sub>4</sub> yield of Pt/CeO<sub>2</sub> 500C and 800NC catalysts are compared in (c).

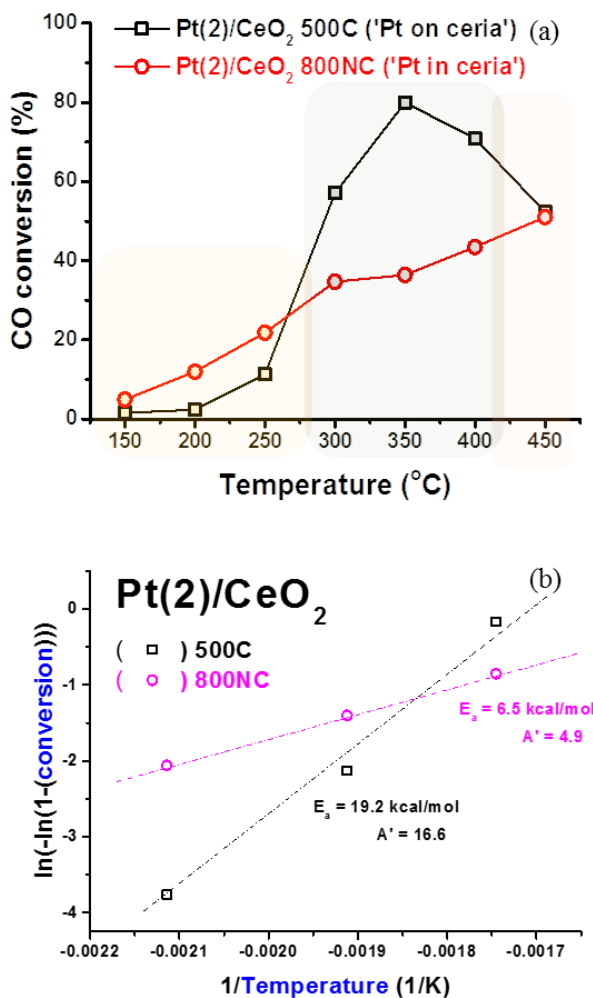


**Figure 4-5.** (a) Comparison of WGS activity of Pt(2)/CeO<sub>2</sub> 500C ('Pt on CeO<sub>2</sub>') and Pt(2)/CeO<sub>2</sub> 800NC ('Pt in CeO<sub>2</sub>') under 3 % CO, 24 % H<sub>2</sub>O, 3 % CO<sub>2</sub>, 20 % H<sub>2</sub> with He balance gas. (b) The activation energies of WGS reaction of Pt(2)/CeO<sub>2</sub> 500C and 800NC catalysts under the full gas feed are compared.

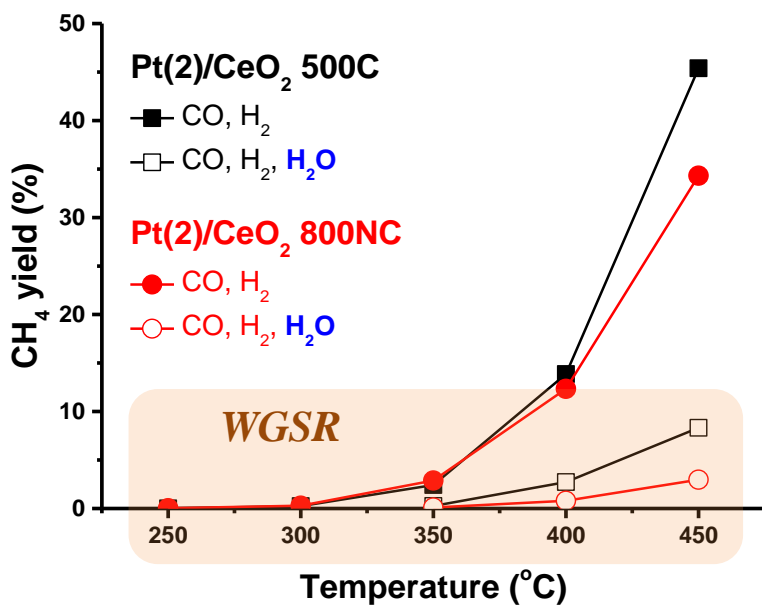


**Figure 4-6.** The effect of the presence of 5 % H<sub>2</sub>O in the CH<sub>4</sub> yield of Pt/CeO<sub>2</sub> 500C and 800NC catalysts. Reactants are composed of 3 % CO, 20 % H<sub>2</sub>, (5% H<sub>2</sub>O) and He balance gas with the total flow rate of 70 mL/min.

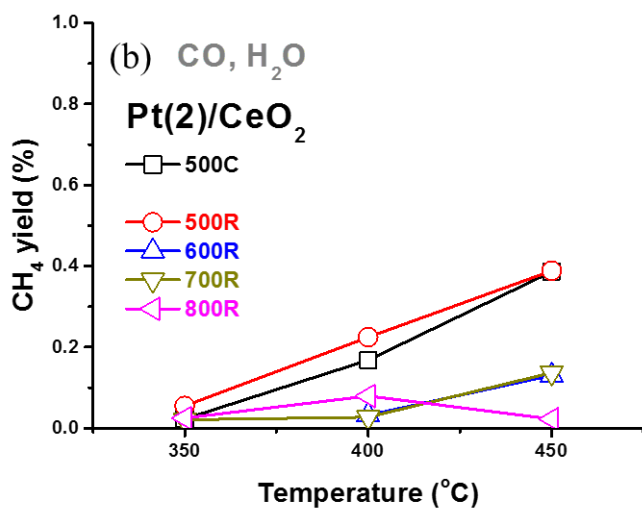
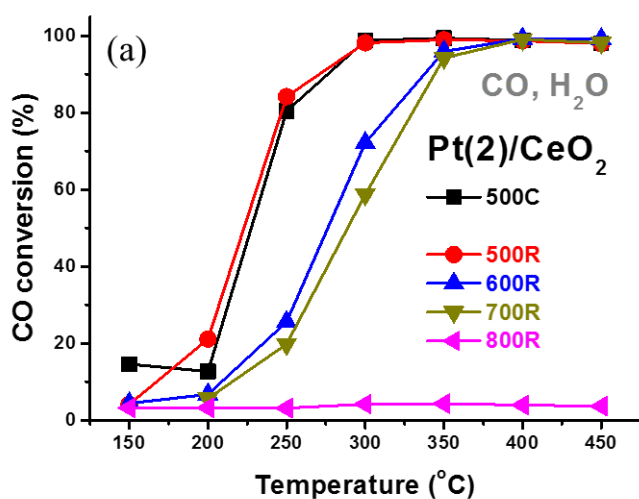


**Figure 4-7.** (a) WGS reactivity and (b) CH<sub>4</sub> yield of Pt(2)/CeO<sub>2</sub> 500C, 500R, 600R, 700R and 800R under the feed of 3 % CO, 24 % H<sub>2</sub>O and He balance gas.

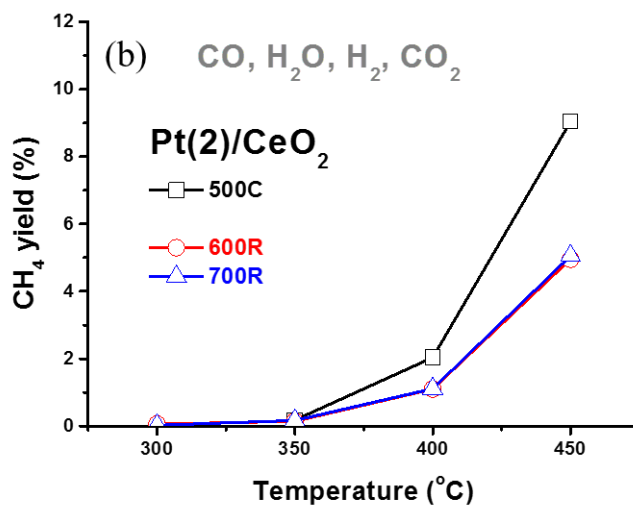
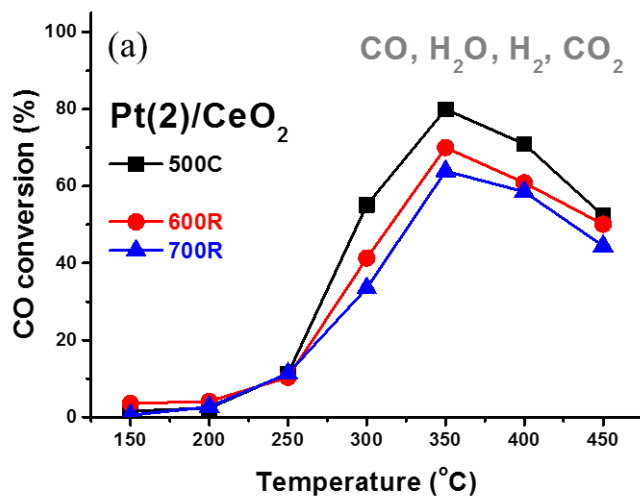


**Figure 4-8.** (a) WGS reactivity and (b) CH<sub>4</sub> yield of Pt(2)/CeO<sub>2</sub> 500C, 600R and 700R under the feed of 3 % CO, 24 % H<sub>2</sub>O, 3 % CO<sub>2</sub>, 20 % H<sub>2</sub> and He balance gas.

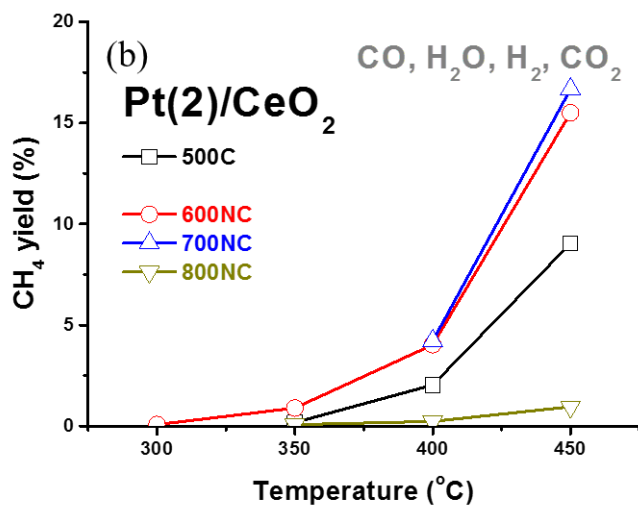
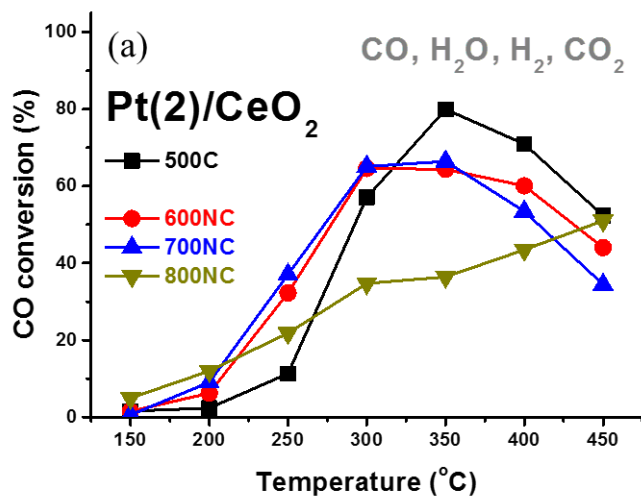


**Figure 4-9.** (a) WGS reactivity and (b)  $\text{CH}_4$  yield of  $\text{Pt(2)/CeO}_2$  500C, 600NC, 700NC and 800NC under the feed of 3 % CO, 24 %  $\text{H}_2\text{O}$ , 3 %  $\text{CO}_2$ , 20 %  $\text{H}_2$  and He balance gas.

#### **4.3.3. Why only Pt(2)/CeO<sub>2</sub> 800NC has the WGS activity, not Pt(2)/CeO<sub>2</sub> 800R?**

Although Pt NPs are covered by CeO<sub>2</sub> over-layers both in Pt(2)/CeO<sub>2</sub> 800R and 800NC, only Pt(2)/CeO<sub>2</sub> 800NC is active in WGS while Pt(2)/CeO<sub>2</sub> 800R is inactive in WGS (Table 4-3). The incomplete covering of Pt NPs could be thought of as the origin of the difference in catalytic activity since the larger amount of CO chemisorbed at -78 °C on Pt(2)/CeO<sub>2</sub> 800NC (0.005 mmol/g) than on Pt(2)/CeO<sub>2</sub> 800R (0.001 mmol/g). However, exposed Pt would not be the active site of 'Pt in CeO<sub>2</sub>' catalyst because the active sites of 'Pt on CeO<sub>2</sub>' and 'Pt in CeO<sub>2</sub>' catalysts are completely different, as discussed in Figure 4-4. In addition, BET surface area of Pt(2)/CeO<sub>2</sub> 800R and 800NC are 17 and 33 m<sup>2</sup>/g, respectively (Table 4-1). Since the values are similar, the difference in BET surface area could not explain the large difference in catalytic activities. One possibility to account for the difference in catalytic activities is that the intrinsic catalytic properties of the CeO<sub>2</sub> surface in two samples are completely different.

Oxygen vacancies on CeO<sub>2</sub> surface have been frequently referred to play an important role in catalyzing WGS [27, 93]. Therefore, the concentration of oxygen vacancy on CeO<sub>2</sub> over-layers of R and NC treated Pt/CeO<sub>2</sub> catalysts needs to be compared to answer why only Pt(2)/CeO<sub>2</sub> 800NC can catalyze WGS. In Chapter 2, it has already been discussed that CO chemisorbs on oxygen vacancies on CeO<sub>2</sub> surface [14]. Therefore, the amount of oxygen vacancies could be estimated from the amount of CO chemisorbed on the surface of CeO<sub>2</sub>.

In Figure 4-10 (a), pulsed CO chemisorption was performed at -78 and 50 °C. CO molecules predominantly adsorb on Pt sites at -78 °C [46]. On the other hand, CO would adsorb both on Pt sites and CeO<sub>2</sub> surface at 50 °C [46]. Hence, the amount of CO adsorbed on CeO<sub>2</sub> surface could be evaluated by subtracting the amount of CO adsorbed at -78 °C from that at 50 °C. Figure 4-10 (a) demonstrates that the amount of CO adsorbed on CeO<sub>2</sub> surface is much larger on NC treated samples than on R treated samples; 37 μmol/g (1.12 μmol/m<sup>2</sup>) and 12 μmol/g (0.70 μmol/m<sup>2</sup>) of CO adsorbed on CeO<sub>2</sub> in Pt(2)/CeO<sub>2</sub> 800NC and 800R, respectively. Since oxygen vacancies promote CO chemisorption, such results indicate that the oxygen vacancy concentration on CeO<sub>2</sub> over-layer is much higher on Pt(2)/CeO<sub>2</sub> 800NC. O 1s XP spectra in Figure 4-10 (b) also indicate the high concentration of oxygen vacancy on Pt(2)/CeO<sub>2</sub> 800NC. In Pt(2)/CeO<sub>2</sub> 800NC, the XP peak from oxygen vacancies is clearly visible in the region between 529 and 531 eV [94, 95]. Such peak was not clearly observed in Pt(2)/CeO<sub>2</sub> 500C nor in Pt(2)/CeO<sub>2</sub> 800R. Only XP peaks from lattice oxygen (528-530 eV) and surface oxygen or OH groups (531-534 eV) are visible in these samples [94, 95].

It can be concluded that only CeO<sub>2</sub> over-layers formed by 800NC treatment could catalyze WGSR because it has the high oxygen vacancy concentration. It is interesting that the metal-support interaction could transform inactive support surface into the active one. In analogy to the present model, Hardacre et al. reported that the Pt(111) surface fully covered by CeO<sub>2</sub> film displayed the high activity in CO oxidation [96]. They suggested that Pt surface promoted the formation of oxygen

vacancies on CeO<sub>2</sub> film, and imparted the catalytic activity to CeO<sub>2</sub> film that was originally inactive for CO oxidation [96]. They also suggested that CeO<sub>2</sub> film should be very thin so that the effective electronic communication between Pt and CeO<sub>2</sub> is maintained [96]. Similarly, Yeung et al. also reported that the WGS activity of Pt@CeO<sub>2</sub> decreased when the CeO<sub>2</sub> layer became too thick [81]. According to pore distribution curves in Figure 4-1, the structure destruction was less severe on Pt(2)/CeO<sub>2</sub> 800NC than on Pt(2)/CeO<sub>2</sub> 800R. Therefore, the thinner CeO<sub>2</sub> over-layers would have been formed on Pt NP in the former catalyst, which could have caused the distinct catalytic activities of two catalysts.

Figure 4-11 displays bright-field TEM images of Pt(2)/CeO<sub>2</sub> 800R and 800NC catalysts. High-Resolution TEM images enable the determination of the thickness of CeO<sub>2</sub> over-layers on Pt NP. Most of Pt NPs in Pt(2)/CeO<sub>2</sub> 800R are present away from the surface (Figure 4-11 (a)). In addition, when the periphery of CeO<sub>2</sub> particle was closely observed, CeO<sub>2</sub> over-layers thicker than 1 nm encapsulating Pt NP are clearly visible (Figure 4-11 (b)). However, in Pt(2)/CeO<sub>2</sub> 800NC, many of Pt NPs are located near the surface (Figure 4-11 (c)). In addition, when the periphery of CeO<sub>2</sub> particle was closely observed, CeO<sub>2</sub> over-layers covering Pt NP were thinner than 0.5 nm (Figure 4-11 (d)). TEM images in Figure 4-11 indicate that the CeO<sub>2</sub> over-layer is thicker on Pt(2)/CeO<sub>2</sub> 800R than on Pt(2)/CeO<sub>2</sub> 800NC.

The molar ratio between Pt and Ce (Pt/Ce) of 'Pt on CeO<sub>2</sub>' (Pt(2)/CeO<sub>2</sub> 500C) and 'Pt in CeO<sub>2</sub>' (800R and 800NC) samples were obtained from XP spectra. Setting Pt/Ce of Pt(2)/CeO<sub>2</sub> 500C as 1, Pt/Ce of Pt(2)/CeO<sub>2</sub> 800R and 800NC was 0.75 and 0.85, respectively (Figure 4-12 (a)). Although Pt/Ce is the complex function of various variables (e.g. Pt surface density, CeO<sub>2</sub> surface area etc.), such result may indicate the presence of thicker CeO<sub>2</sub> over-layers on Pt(2)/CeO<sub>2</sub> 800R [97]. Figure 4-12 (b) displays depth profiling XP spectra of Pt(2)/CeO<sub>2</sub> 500C, 800R and 800NC. Samples were ion sputtered using an Ar gun before taking each XP spectrum. Pt/Ce most rapidly decreased with the increasing number of Ar sputtering in Pt(2)/CeO<sub>2</sub> 500C. This is not surprising since Ar could easily remove Pt species on 'Pt on CeO<sub>2</sub>'. Pt/Ce decreased more slowly on 'Pt in CeO<sub>2</sub>' samples (Figure 4-11 (b)). This is because CeO<sub>2</sub> over-layers on Pt NP delayed the removal of Pt by Ar sputtering. In addition, Pt/Ce decreased more slowly in 800R treated sample than in 800NC treated sample. This is another evidence that the thicker CeO<sub>2</sub> over-layers are formed on the former sample. It can be summarized that although Pt NP were covered with CeO<sub>2</sub> over-layers both after 800R or 800NC treatments, the thinner CeO<sub>2</sub> over-layers are formed after 800NC treatment. Thinner CeO<sub>2</sub> over-layers interact with Pt NPs to possess the high concentration of oxygen vacancies, which could catalyze WGS on 'Pt in CeO<sub>2</sub>' catalyst.

The WGS activity of CeO<sub>2</sub> over-layers was investigated with in-situ DRIFT analysis. After CO adsorption and N<sub>2</sub> purging, DRIFT peaks from monodentate formate in the regions of 1250-1350 cm<sup>-1</sup> and 1500-1650 cm<sup>-1</sup> mainly survived on CeO<sub>2</sub> 500C, Pt(2)/CeO<sub>2</sub> 800R and 800NC samples (Figure 4-13) [93]. Previously, Collins et al. reported that monodentate formates are active intermediates in WGS [93]. However, Pt(2)/CeO<sub>2</sub> 800R displayed only low intensity peaks over the entire range of wavenumber. This can be explained by the lack of oxygen vacancies, the CO adsorption site, on CeO<sub>2</sub> over-layers of Pt(2)/CeO<sub>2</sub> 800R as discussed in Figure 4-10. H<sub>2</sub>O was added at 100 °C after N<sub>2</sub> purging. In Figure 4-14, time-on-stream variations in peak maxima of monodentate formate ( $\nu_s(\text{OCO})$  at 1300 cm<sup>-1</sup>) was followed under the feed containing 3 % H<sub>2</sub>O. Figure 4-14 clearly demonstrates that monodentate formates on 'Pt in CeO<sub>2</sub>' is consumed by reacting with H<sub>2</sub>O while those on CeO<sub>2</sub> 500C did not. This strongly indicates that inert CeO<sub>2</sub> surface was activated in WGS by the interaction with Pt. In the case of Pt(2)/CeO<sub>2</sub> 500C, monodentate formates did not react with H<sub>2</sub>O (Figure 4-14); instead the peak intensities in the region of 1350-1500 cm<sup>-1</sup> (CO adsorbed on Pt-CeO<sub>2</sub> interface) greatly diminished in intensity (data not shown). Therefore, completely different reaction mechanisms operate on 'Pt on CeO<sub>2</sub>' and 'Pt in CeO<sub>2</sub>', in agreement with the conclusion of sub-section 4.3.2.1. The present work would be the good example of how the intrinsic metal-support interactions could affect the chemical properties and catalytic performances of catalysts.

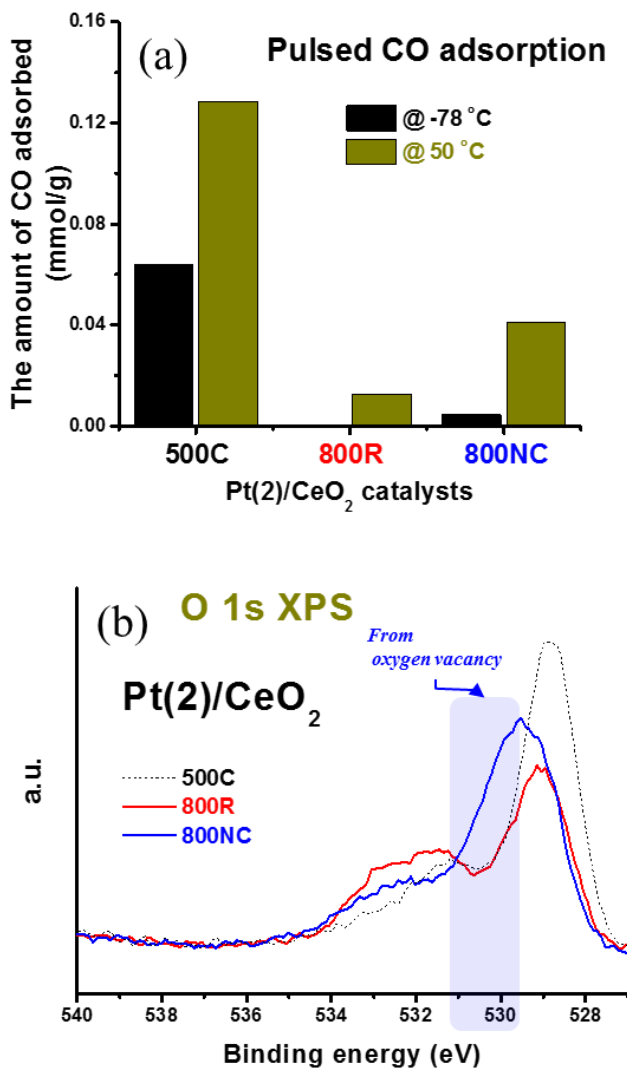


**Figure 4-10.** Pulsed CO chemisorption was performed at -78 and 50 °C. The amount of CO chemisorbed in Pt/CeO<sub>2</sub> catalysts (either ‘R’ or ‘NC’ treated) are compared in (a). (b) O 1s XPS spectra of Pt(2)/CeO<sub>2</sub> 500C, 800R and 800NC catalysts.

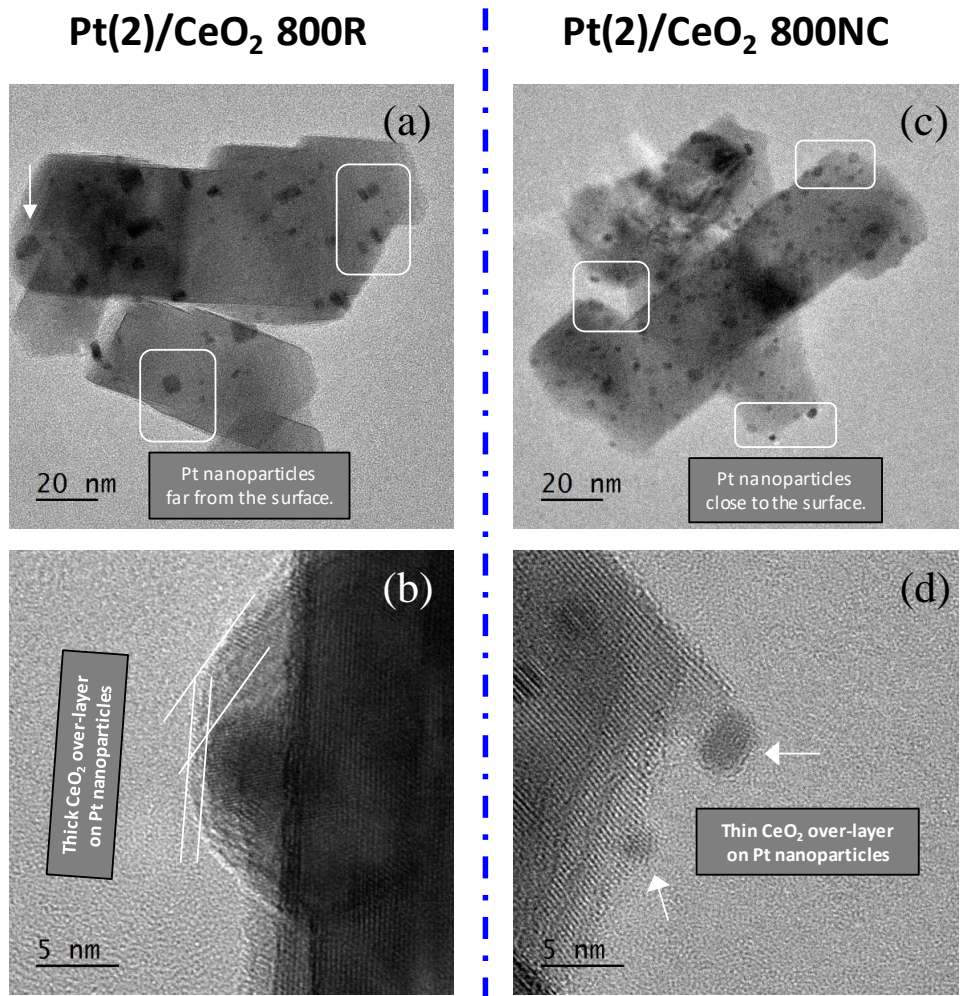


**Figure 4-11.** Bright-field TEM images of Pt(2)/CeO<sub>2</sub> 800R ((a) and (b)) and Pt(2)/CeO<sub>2</sub> 800NC ((c) and (d)) catalysts.

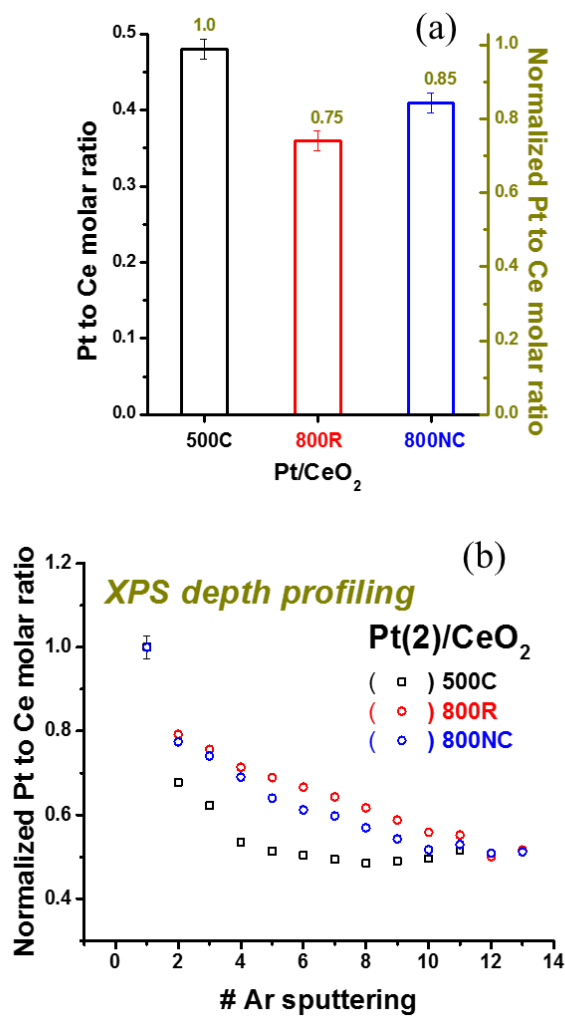


**Figure 4-12.** Pt to Ce molar ratio of Pd(2)/CeO<sub>2</sub> 500C, 800R and 800NC catalysts, calculated from XP spectra, are compared in (a). Error bars are included in the figure. Depth-profiling XP spectra of Pt/CeO<sub>2</sub> catalysts are compared in (b).

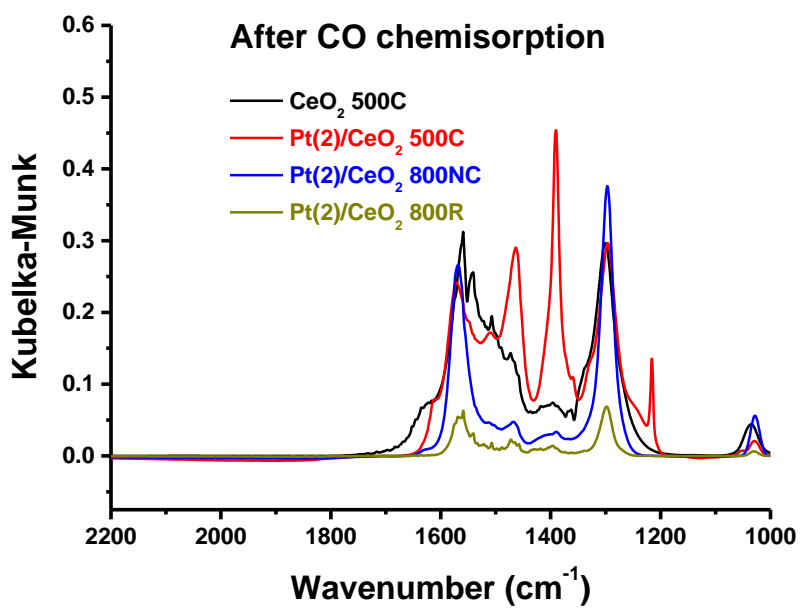


**Figure 4-13.** Comparison of in-situ CO-DRIFT spectra of CeO<sub>2</sub> 500C, Pt(2)/CeO<sub>2</sub> 500C, 800NC and 800R after CO adsorption followed by N<sub>2</sub> purging for 60 min at 100 °C.

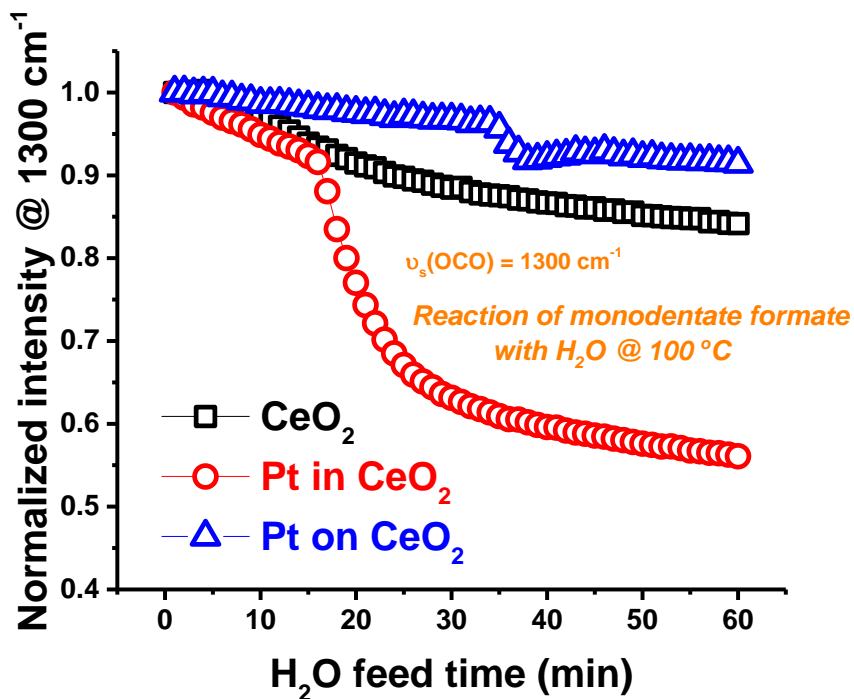


**Figure 4-14.** The variation in the peak intensity of DRIFT spectra from monodentate formate ( $\nu_s(\text{OCO}) = 1300 \text{ cm}^{-1}$ ) upon  $\text{H}_2\text{O}$  addition was monitored. Prior to  $\text{H}_2\text{O}$  addition, catalysts were exposed to  $\text{CO}$  flow for 60 min and purged under  $\text{N}_2$  flow for 60 min. These in-situ DRIFT experiments were carried out at  $100 \text{ }^\circ\text{C}$ .

## Chapter 5. Summary and Conclusions

In this thesis, the metal-support interaction between PGMs and metal-oxides (e.g. Pt/CeO<sub>2</sub>, Pt/TiO<sub>2</sub>) was investigated under both oxidizing and reducing conditions, and based on the understandings three distinct strategies were devised to modify the metal-support interaction to improve catalytic performances of CO oxidation and WGS reaction.

According to Raman spectra, Pt is anchored on CeO<sub>2</sub> surface by forming Pt-O-Ce bonds under the oxidizing atmosphere. Pt-O-Ce bonds bring about the high dispersion of Pt. Under the reducing atmosphere, Pt-O-Ce bonds can be reduced, and static CO chemisorption showed that Pt is located on the oxygen vacancies generated on CeO<sub>2</sub> surface. Pt-O-Ce bonds not only provided the high Pt dispersion, but they also improved the thermal stability of CeO<sub>2</sub>. Pt/CeO<sub>2</sub> sustained its structure from 1000 °C oxidation treatment, while CeO<sub>2</sub> structure collapsed. The thermal stability of Pt/CeO<sub>2</sub> increased as the Pt loading increased. In addition, when surface oxygen of Pt/CeO<sub>2</sub> was selectively removed, there was a decrease in the thermal stability of CeO<sub>2</sub>. These evidences emphasize the importance of Pt-O-Ce bond in improving the thermal stability of Pt/CeO<sub>2</sub> sample against high-temperature treatments.

While Pt-O-Ce bond maintained the sample structure from the high temperature treatment, Pt-O-Ce bond also became harder to be reduced after the high temperature treatment. XPS results showed that Pt concentration on Pt/CeO<sub>2</sub> surface

was decreased after the oxidative treatment at elevated temperature. Therefore, it is suggested that Pt diffuses into CeO<sub>2</sub> structure at elevated temperature.

To improve the CO oxidation performance of Pt/CeO<sub>2</sub> catalyst, the Pt-CeO<sub>2</sub> interaction was weakened by loading Pt on CeO<sub>2</sub> surface with low defect concentration. Pt was loaded on high-temperature (800 °C) treated CeO<sub>2</sub> (Pt(2)/(800C)CeO<sub>2</sub>), where high-temperature treatment decreased the defect concentration on CeO<sub>2</sub> surface. The CO oxidation ability of Pt(2)/(800C)CeO<sub>2</sub> was superior to that of Pt(2)/CeO<sub>2</sub> catalyst; the temperature of 50% conversion of CO oxidation shifted 76 °C to the lower temperature. Particularly, Pt/(800C)CeO<sub>2</sub> accomplished ~100% CO conversion below 150 °C. Such enhanced activity is explained by the formation of PtO<sub>2</sub> species that interact weakly with CeO<sub>2</sub>. The small amount of Pt metal clusters (larger than 5 nm) was formed on Pt(2)/(800C)CeO<sub>2</sub> after the oxidative treatment at 800 °C, which was not observed on Pt/CeO<sub>2</sub>. This indicates that the resistance against Pt sintering decreased when the defect concentration of CeO<sub>2</sub> decreased. However, relatively high Pt dispersion was maintained on (800C)CeO<sub>2</sub> (47 %) even after the oxidative treatment at 800 °C. It can be concluded that by weakening the Pt-CeO<sub>2</sub> interaction, the CO oxidation ability of Pt/CeO<sub>2</sub> catalyst was greatly enhanced while retaining the excellent thermal resistance against Pt sintering.

To improve the CO oxidation performance of Pt/TiO<sub>2</sub> catalyst, the Pt-TiO<sub>2</sub> interaction was weakened by loading Pt on S-doped TiO<sub>2</sub> surface (Pt/S-TiO<sub>2</sub>). The temperature for 50% conversion of CO oxidation of Pt/S-TiO<sub>2</sub> was 50 °C lower than

that of Pt/TiO<sub>2</sub>. Especially, Pt(4)/S-TiO<sub>2</sub> accomplished ~100% CO conversion below 150 °C. S-dopants hindered metal-support interaction and induced the formation of large metallic Pt clusters with the high intrinsic CO oxidation ability.

The catalytic performance could be also improved by modifying the geometry of catalysts to facilitate the metal-support interaction. 'Pt in CeO<sub>2</sub>' samples were synthesized from 'Pt on CeO<sub>2</sub>' by the controlled reductive treatments to prepare HT-WGSR catalysts with good activity and suppressed CH<sub>4</sub> formation. The structure of Pt(2)/CeO<sub>2</sub> was modified by using two different methods; **1.** by the reductive treatment to reduce CeO<sub>2</sub> bulk (R treatment) and **2.** by the reductive treatment at 250 °C followed by the thermal treatment with N<sub>2</sub> (NC treatment). After 800R treatment, WGSR activity of Pt/CeO<sub>2</sub> was completely lost. However, HT-WGSR activity of Pt/CeO<sub>2</sub> 800NC ('Pt in CeO<sub>2</sub>') was comparable to that of 'Pt on CeO<sub>2</sub>', while CH<sub>4</sub> production rate was greatly suppressed. Detailed XPS, CO chemisorption and in-situ DRIFT studies indicate that such difference is attributed to the high concentration of oxygen vacancies on thin CeO<sub>2</sub> over-layers formed after 800NC treatment. The interaction between CeO<sub>2</sub> over-layers and underneath Pt NP granted the catalytic activity to originally inactive CeO<sub>2</sub> surface. Therefore, 'Pt in CeO<sub>2</sub>' prepared by 800NC treatment in the present work would be the good candidate HT-WGSR catalyst with high activity and suppressed CH<sub>4</sub> formation.

## Bibliography

- [1] D. Kunwar, S. Zhou, A. DeLaRiva, E.J. Peterson, H. Xiong, X.I. Pereira-Hernández, S.C. Purdy, R. ter Veen, H.H. Brongersma, J.T. Miller, *ACS Catal.*, 9 (2019) 3978-3990.
- [2] H. Wang, J.-X. Liu, L.F. Allard, S. Lee, J. Liu, H. Li, J. Wang, J. Wang, S.H. Oh, W. Li, *Nat. Commun.*, 10 (2019) 1-12.
- [3] N. Daelman, M. Capdevila-Cortada, N. López, *Nat. Mat.*, (2019).
- [4] A. Beniya, S. Higashi, *Nat. Catal.*, 2 (2019) 590-602.
- [5] H. Jeong, G. Lee, B.-S. Kim, J. Bae, J.W. Han, H. Lee, *J. Am. Chem. Soc.*, 140 (2018) 9558-9565.
- [6] C.-T. Kuo, Y. Lu, L. Kovarik, M.H. Engelhard, A.M. Karim, *ACS Catal.*, (2019).
- [7] X.I. Pereira-Hernández, A. DeLaRiva, V. Muravev, D. Kunwar, H. Xiong, B. Sudduth, M. Engelhard, L. Kovarik, E.J. Hensen, Y. Wang, *Nat. Commun.*, 10 (2019) 1358.
- [8] L. DeRita, S. Dai, K. Lopez-Zepeda, N. Pham, G.W. Graham, X. Pan, P. Christopher, *J. Am. Chem. Soc.*, 139 (2017) 14150-14165.
- [9] A. Bruix, J.A. Rodriguez, P.J. Ramírez, S.D. Senanayake, J. Evans, J.B. Park, D. Stacchiola, P. Liu, J. Hrbek, F. Illas, *J. Am. Chem. Soc.*, 134 (2012) 8968-8974.
- [10] M. Cargnello, P. Fornasiero, R. Gorte, *Catal. Lett.*, 142 (2012) 1043-1048.
- [11] T.W. van Deelen, C.H. Mejía, K.P. de Jong, *Nat. Catal.*, (2019) 1-16.
- [12] A. Russell, W.S. Epling, *Catal. Rev.: Sci. Eng.*, 53 (2011) 337-423.

- [13] Y. Ryou, J. Lee, H. Lee, J.W. Choung, S. Yoo, D.H. Kim, *Catal. Today*, 258 (2015) 518-524.
- [14] J. Lee, Y. Ryou, X. Chan, T.J. Kim, D.H. Kim, *J. Phys. Chem. C*, 120 (2016) 25870-25879.
- [15] J. Lee, Y. Ryou, J. Kim, X. Chan, T.J. Kim, D.H. Kim, *J. Phys. Chem. C*, 122 (2018) 4972-4983.
- [16] J. Lee, I. Song, D.H. Kim, *ChemCatChem*, 10 (2018) 1258-1262.
- [17] S. Hinokuma, H. Fujii, M. Okamoto, K. Ikeue, M. Machida, *Chem. Mater.*, 22 (2010) 6183-6190.
- [18] K. Ding, A. Gulec, A.M. Johnson, N.M. Schweitzer, G.D. Stucky, L.D. Marks, P.C. Stair, *Science*, 350 (2015) 189-192.
- [19] H. Lee, D.-H. Lee, Y.-H. Song, W.C. Choi, Y.-K. Park, D.H. Kim, *Chem. Eng. J.*, 259 (2015) 761-770.
- [20] W.R. Schwartz, D. Ciuparu, L.D. Pfefferle, *J. Phys. Chem. C*, 116 (2012) 8587-8593.
- [21] A. Toso, S. Colussi, J. Llorca, A. Trovarelli, *Appl. Catal. A: Gen.*, 574 (2019) 79-86.
- [22] Y. Ma, B. Chi, W. Liu, L. Cao, Y. Lin, X. Zhang, X. Ye, S. Wei, J. Lu, *ACS Catal.*, 9 (2019) 8404-8412.
- [23] M.G. Castaño, T. Reina, S. Ivanova, M. Centeno, J. Odriozola, *J. Catal.*, 314 (2014) 1-9.
- [24] S. Aranifard, S.C. Ammal, A. Heyden, *J. Catal.*, 309 (2014) 314-324.

- [25] Y. Zhai, D. Pierre, R. Si, W. Deng, P. Ferrin, A.U. Nilekar, G. Peng, J.A. Herron, D.C. Bell, H. Saltsburg, *Science*, 329 (2010) 1633-1636.
- [26] C. Kalamaras, D. Dionysiou, A. Efstathiou, *ACS Catal.*, 2 (2012) 2729-2742.
- [27] C. Kalamaras, D. Dionysiou, A. Efstathiou, *ACS Catal.*, 2 (2012) 2729-2742.
- [28] C.T. Campbell, C.H. Peden, *Science*, 309 (2005) 713-714.
- [29] A. Laachir, V. Perrichon, A. Badri, J. Lamotte, E. Catherine, J.C. Lavalley, J. El Fallah, L. Hilaire, F. Le Normand, E. Quéméré, *J. Chem. Soc., Faraday Trans.*, 87 (1991) 1601-1609.
- [30] A. Satsuma, K. Osaki, M. Yanagihara, J. Ohyama, K. Shimizu, *Appl. Catal., B*, 132 (2013) 511-518.
- [31] Y. Nagai, T. Hirabayashi, K. Dohmae, N. Takagi, T. Minami, H. Shinjoh, S.i. Matsumoto, *J. Catal.*, 242 (2006) 103-109.
- [32] J.A. Farmer, C.T. Campbell, *Science*, 329 (2010) 933-936.
- [33] A. Trovarelli, *Catal. Rev.*, 38 (1996) 439-520.
- [34] S.E. Golunski, H.A. Hatcher, R.R. Rajaram, T.J. Truex, *Appl. Catal., B*, 5 (1995) 367-376.
- [35] P. Bera, A. Gayen, M. Hegde, N. Lalla, L. Spadaro, F. Frusteri, F. Arena, *J. Phys. Chem. B*, 107 (2003) 6122-6130.
- [36] C. Ratnasamy, J.P. Wagner, *Catal. Rev. Sci. Eng.*, 51 (2009) 325-440.
- [37] S. Tauster, S. Fung, R. Garten, *J. Am. Chem. Soc.*, 100 (1978) 170-175.
- [38] S.A. Stevenson, J.A. Dumesic, R.T.K. Baker, *Metal-support interactions in catalysis, sintering, and redispersion*, Van Nostrand Reinhold 1987.

- [39] J. Chastain, R.C. King, J. Moulder, Handbook of X-ray Photoelectron Spectroscopy: a Reference Book of Standard Spectra for Identification and Interpretation of XPS Data, Physical Electronics Eden Prairie, MN1995.
- [40] M. Sanchez, J. Gazquez, J. Catal. , 104 (1987) 120-135.
- [41] H. Yao, Y.Y. Yao, J. Catal. , 86 (1984) 254-265.
- [42] S. Alayoglu, K. An, G.r.m. Melae, S. Chen, F. Bernardi, L.W. Wang, A.E. Lindeman, N. Musselwhite, J. Guo, Z. Liu, J. Phys. Chem. C, 117 (2013) 26608-26616.
- [43] J. Frost, Nature, 334 (1988) 577-580.
- [44] N. Acerbi, S. Tsang, G. Jones, S. Golunski, P. Collier, Angew. Chem., Int. Ed., 52 (2013) 7737-7741.
- [45] A. Papavasiliou, A. Tsetsekou, V. Matsouka, M. Konsolakis, I. Yentekakis, N. Boukos, J. Phys. Chem. B, 90 (2009) 162-174.
- [46] T. Tanabe, Y. Nagai, T. Hirabayashi, N. Takagi, K. Dohmae, N. Takahashi, S.i. Matsumoto, H. Shinjoh, J.N. Kondo, J.C. Schouten, Appl. Catal. A: Gen., 370 (2009) 108-113.
- [47] M. Daniel, S. Loidant, J. Raman Spectrosc. , 43 (2012) 1312-1319.
- [48] M.S. Brogan, T.J. Dines, J.A. Cairns, J. Chem. Soc., Faraday Trans., 90 (1994) 1461-1466.
- [49] I. Kosacki, T. Suzuki, H.U. Anderson, P. Colomban, Solid State Ionics, 149 (2002) 99-105.
- [50] W. Lin, A. Herzing, C. Kiely, I. Wachs, J. Phys. Chem. C, 112 (2008) 5942-5951.

- [51] C. Zhang, A. Michaelides, D.A. King, S.J. Jenkins, *Phys. Rev. B*, 79 (2009) 075433.
- [52] J. Jones, H. Xiong, A.T. DeLaRiva, E.J. Peterson, H. Pham, S.R. Challa, G. Qi, S. Oh, M.H. Wiebenga, X.I.P. Hernández, Y. Wang, A.K. Datye, *Science*, 353 (2016) 150-154.
- [53] J.H. Kwak, J. Hu, D. Mei, C.-W. Yi, D.H. Kim, C.H. Peden, L.F. Allard, J. Szanyi, *Science*, 325 (2009) 1670-1673.
- [54] S. Yuvaraj, L. Fan-Yuan, C. Tsong-Huei, Y. Chuin-Tih, *J. Phys. Chem. B*, 107 (2003) 1044-1047.
- [55] B. Qiao, A. Wang, X. Yang, L.F. Allard, Z. Jiang, Y. Cui, J. Liu, J. Li, T. Zhang, *Nat. Chem.*, 3 (2011) 634-641.
- [56] M. Mao, H. Lv, Y. Li, Y. Yang, M. Zeng, N. Li, X. Zhao, *ACS Catal.*, 6 (2015) 418-427.
- [57] J.A. Farmer, J.H. Baricuatro, C.T. Campbell, *J. Phys. Chem. C*, 114 (2010) 17166-17172.
- [58] A. Vijay, G. Mills, H. Metiu, *J. Chem. Phys.*, 118 (2003) 6536-6551.
- [59] T.V. Johnson, *SAE Paper*, 5 (2012) 216-234.
- [60] R.M. Heck, R.J. Farrauto, S.T. Gulati, *Catalytic air pollution control: commercial technology*, John Wiley & Sons 2009.
- [61] Q. Fu, H. Saltsburg, M. Flytzani-Stephanopoulos, *Science*, 301 (2003) 935-938.
- [62] S. Gatla, D. Aubert, G. Agostini, O. Mathon, S. Pascarelli, T. Lunkenbein, M.G. Willinger, H. Kaper, *ACS Catal.*, 6 (2016) 6151-6155.

- [63] W. Tang, Z. Hu, M. Wang, G.D. Stucky, H. Metiu, E.W. McFarland, *J. Catal.*, 273 (2010) 125-137.
- [64] P. Periyat, S.C. Pillai, D.E. McCormack, J. Colreavy, S.J. Hinder, *The Journal of Physical Chemistry C*, 112 (2008) 7644-7652.
- [65] T. Umebayashi, T. Yamaki, S. Tanaka, K. Asai, *Chem. Lett.*, 32 (2003) 330-331.
- [66] T. Ohno, M. Akiyoshi, T. Umebayashi, K. Asai, T. Mitsui, M. Matsumura, *Appl. Catal. A: Gen.*, 265 (2004) 115-121.
- [67] T. Umebayashi, T. Yamaki, H. Itoh, K. Asai, *Appl. Phys. Lett.*, 81 (2002) 454-456.
- [68] J. Chen, R. Yang, *J. Catal.*, 139 (1993) 277-288.
- [69] M. Hidalgo, M. Maicu, J. Navío, G. Colón, *Appl. Catal. B: Environ.*, 81 (2008) 49-55.
- [70] I. Song, S. Youn, D.H. Kim, *Top. Catal.*, 59 (2016) 1008-1012.
- [71] A. Borodziński, M. Bonarowska, *Langmuir*, 13 (1997) 5613-5620.
- [72] P.J. Berlowitz, C.H. Peden, D.W. Goodman, *J. Phys. Chem.*, 92 (1988) 5213-5221.
- [73] G. Zafiris, R. Gorte, *J. Catal.*, 140 (1993) 418-423.
- [74] A. Szabó, M.A. Henderson, J.T. Yates Jr, *J. Chem. Phys.*, 96 (1992) 6191-6202.
- [75] J.L. Gland, M.R. McClellan, F.R. McFeely, *J. Chem. Phys.*, 79 (1983) 6349-6356.
- [76] B. Atalik, D. Uner, *J. Catal.*, 241 (2006) 268-275.
- [77] I. Song, S. Youn, H. Lee, D.H. Kim, *Korean J. Chem. Eng.*, 33 (2016) 2547-

2554.

- [78] H. Yoshida, S. Nonoyama, Y. Yazawa, T. Hattori, *Phys. Scr.*, 2005 (2005) 813.
- [79] D. Pierre, W. Deng, M. Flytzani-Stephanopoulos, *Top. Catal.*, 46 (2007) 363-373.
- [80] G. Jacobs, U.M. Graham, E. Chenu, P.M. Patterson, A. Dozier, B.H. Davis, *J. Catal.*, 229 (2005) 499-512.
- [81] C.M. Yeung, K.M.K. Yu, Q.J. Fu, D. Thompsett, M.I. Petch, S.C. Tsang, *J. Am. Chem. Soc.*, 127 (2005) 18010-18011.
- [82] E. Saw, U. Oemar, X. Tan, Y. Du, A. Borgna, K. Hidajat, S. Kawi, *J. Catal.*, 314 (2014) 32-46.
- [83] M. Ang, U. Oemar, E. Saw, L. Mo, Y. Kathiraser, B. Chia, S. Kawi, *ACS Catal.*, 4 (2014) 3237-3248.
- [84] C.M. Yeung, F. Meunier, R. Burch, D. Thompsett, S.C. Tsang, *J. Phys. Chem. B*, 110 (2006) 8540-8543.
- [85] C.M.Y. Yeung, S.C. Tsang, *J. Phys. Chem. C*, 113 (2009) 6074-6087.
- [86] G. Jacobs, L. Williams, U. Graham, D. Sparks, B.H. Davis, *J. Phys. Chem. B*, 107 (2003) 10398-10404.
- [87] Y. Xi, N.A. Ottinger, Z.G. Liu, *Appl. Catal. B: Environ.*, 160 (2014) 1-9.
- [88] J. Rodriguez, S. Ma, P. Liu, J. Hrbek, J. Evans, M. Perez, *Science*, 318 (2007) 1757-1760.
- [89] L. Mendelovici, M. Steinberg, *J. Catal.*, 96 (1985) 285-287.
- [90] T. Takeguchi, S. Manabe, R. Kikuchi, K. Eguchi, T. Kanazawa, S. Matsumoto,

- W. Ueda, *Appl. Catal. A: Gen.*, 293 (2005) 91-96.
- [91] T. Jin, Y. Zhou, G. Mains, J. White, *J. Phys. Chem.*, 91 (1987) 5931-5937.
- [92] C. Binet, A. Jadi, J.-C. Lavalley, M. Boutonnet-Kizling, *J. Chem. Soc., Faraday Trans.*, 88 (1992) 2079-2084.
- [93] J. Vecchietti, A. Bonivardi, W. Xu, D. Stacchiola, J.J. Delgado, M. Calatayud, S.n.E. Collins, *ACS Catal.*, 4 (2014) 2088-2096.
- [94] M. Konsolakis, M. Sgourakis, S.A. Carabineiro, *Appl. Surf. Sci.*, 341 (2015) 48-54.
- [95] V. Santos, S. Carabineiro, J. Bakker, O. Soares, X. Chen, M. Pereira, J. Órfão, J. Figueiredo, J. Gascon, F. Kapteijn, *J. Catal.*, 309 (2014) 58-65.
- [96] C. Hardacre, R.M. Ormerod, R.M. Lambert, *J. Phys. Chem.* , 98 (1994) 10901-10905.
- [97] S.C. Fung, *J. Catal.*, 58 (1979) 454-469.

## 국 문 초 록

전이 금속 산화물 지지체와 귀금속 간의 금속-지지체 상호작용 (metal-support interaction)을 조절함으로써 촉매의 화학적 특성을 조절하고 촉매 성능을 크게 개선할 수 있다. 이러한 맥락에서, 이 논문에서는 우선 metal-support interaction이 산화 및 환원 분위기에서 어떻게 작동하는지 연구하였다. 또한, metal-support interaction을 세가지 다른 효과적인 방법으로 조절하여, 촉매 성능(일산화탄소 산화 반응(CO oxidation)과 수성 가스 전이 반응(Water-Gas-Shift reaction; WGS))을 개선하는데 성공하였다.

본 논문에서는 우선, 환원 및 산화 분위기에서 플래티넘(Pt)과 세리아( $\text{CeO}_2$ )가 어떻게 상호작용하는지를 연구하였다. 라만 분광법(Raman spectroscopy)에 따르면, Pt은 산화 분위기에서 Pt-O-Ce 결합을 형성함으로써  $\text{CeO}_2$  표면에 강하게 결합한다. 흥미롭게도, 산화 온도가 500 °C에서 800 °C로 증가하면 Pt은  $\text{CeO}_2$ 와 더 강하게 상호작용하였다. 또한, 환원 분위기에서,  $\text{CeO}_2$ 에 화학-흡착한 일산화탄소(carbon monoxide; CO) 양은 Pt/ $\text{CeO}_2$ 에 화학-흡착한 CO 양과 동일하였다. 이는 Pt이 환원된  $\text{CeO}_2$  표면에 생성된 산소 결함(oxygen vacancy)에 위치함을 의미한다. Pt/ $\text{CeO}_2$ 의 표면적은 산화 분위기에서 1000 °C에 노출되어도 큰 변화 없이 유지되었

다. 그러나 Pt-O-Ce 결합이 선택적으로 제거되면, 고온 처리 후 Pt/CeO<sub>2</sub>의 표면적은 크게 감소하였다. 따라서, Pt-O-Ce 결합이 Pt/CeO<sub>2</sub>의 열-안정성을 향상시키는 데 중요한 역할을 한다고 결론 내릴 수 있었다.

Pt을 담지하기 전에 CeO<sub>2</sub> 표면의 결합 농도(defect concentration)를 감소시키면, Pt과 CeO<sub>2</sub> 사이의 상호작용이 약해지고, Pt/CeO<sub>2</sub> 촉매의 CO oxidation 활성은 증가한다. CeO<sub>2</sub> 표면의 defect concentration는 CeO<sub>2</sub>를 고온-열처리하면 감소한다. 따라서, 800 °C에서 CeO<sub>2</sub>를 열처리하고 Pt을 담지하여 촉매를 제조하였다 (Pt/(800C)CeO<sub>2</sub>.) Pt/(800C)CeO<sub>2</sub>는 800 °C에서 열처리 후, Pt가 담지 된 감마 알루미나 촉매(Pt/ $\gamma$ -Al<sub>2</sub>O<sub>3</sub>)보다 높은 Pt 분산도를 유지하여 Pt 소결에 대한 우수한 열 저항성을 보였다. 또한, Pt/(800C)CeO<sub>2</sub> 촉매는 Pt/CeO<sub>2</sub> 촉매보다 76 °C 더 낮은 온도에서 CO를 전부 산화 하였다. 이러한 촉매 활성 향상은 CeO<sub>2</sub>와 약하게 상호작용하는 산화 플래티넘(PtO<sub>2</sub>)의 형성에 기인한다.

Pt/CeO<sub>2</sub> 촉매와 유사하게, Pt과 티타니아(TiO<sub>2</sub>) 사이의 상호작용을 약화시키면, Pt가 담지 된 TiO<sub>2</sub>(Pt/TiO<sub>2</sub>) 촉매의 CO oxidation 활성을 증진할 수 있다. Pt를 황이 도핑 된 TiO<sub>2</sub>(S-TiO<sub>2</sub>)에 담지하면(Pt/S-TiO<sub>2</sub>), Pt는 TiO<sub>2</sub> 표면과 더 약하게 상호작용하고, 더 많은 금속 특성을 가지는 커다란 Pt 클러스터가 형성된다. Pt/S-TiO<sub>2</sub> 촉매는 Pt/TiO<sub>2</sub> 촉매보다 50 °C 더 낮은 온도에서 CO를 전부 산화 하였다.

마지막으로, 촉매의 기하학적 구조를 바꿔줌으로써 특정한 metal-support interaction을 유도하여 촉매 성능을 개선할 수 있다. 제어 된 환원 처리를 적용하여, Pt 나노 입자가 CeO<sub>2</sub> 과층에 갇힌 촉매(Pt in CeO<sub>2</sub>)를 제조하는 데 성공하였다. Pt가 기상에 노출된 Pt/CeO<sub>2</sub> 촉매(Pt on CeO<sub>2</sub>)는 우수한 고온 WGSR 활성을 나타내지만, Pt가 부산물로서 메탄(CH<sub>4</sub>)의 형성을 촉진한다는 문제가 있다. 반면에, ‘Pt in CeO<sub>2</sub>’ 촉매는 Pt가 노출되어 있지 않아서 CH<sub>4</sub>이 생성되지 않았고, 높은 고온 WGSR 활성도 나타내었다. 흥미롭게도, 얇은 CeO<sub>2</sub> 과층은 WGSR 활성이 있었지만, 두꺼운 CeO<sub>2</sub> 과층은 WGSR 활성이 없었다. Pt의 영향으로 얇은 CeO<sub>2</sub> 과층에는 oxygen vacancy 농도가 높았는데, oxygen vacancy가 WGSR 반응의 중간체인 한 자리 폼산염(monodentate formate)의 형성을 촉진하기 때문에 얇은 CeO<sub>2</sub> 과층에서만 우수한 WGSR 활성이 나타난 것으로 분석된다.

**주요어:** 귀금속, 전이 금속 산화물 지지체, 금속-지지체 상호작용, 일산화탄소 산화 반응, 수성 가스 전이 반응

**학번:** 2014-21513